Coating Techniques and Characterization of Protective Coatings for Electrode Materials in Lithium Ion Batteries

-With the Examples of TiO_2 on NCM by ALD and Plasma Polymerization of 1.4bis(trifluoromethyl)benzene on Lithium-

Dem Fachbereich Biologie und Chemie

der Justus-Liebig-Universität Gießen

vorgelegte Dissertation zur Erlangung

des akademischen Grades

Doktor der Naturwissenschaften

- Dr. rer. nat. -

Yannik Moryson

_____ November 2023 _____

Dekan / Dean	Prof. Dr. Thomas Wilke
1. Gutachter / 1st Reviewer	Prof. Dr. Jürgen Janek (Justus-Liebig-Universität Gießen)
2. Gutachter / 2nd Reviewer	Prof. Dr. Michael Dürr (Justus-Liebig-Universität Gießen)
Eingereicht / Submitted	November 2023
Disputation /Disputation	19.12.2023

Eidesstattliche Erklärung

Die vorliegende Arbeit wurde im Zeitraum vom 18.01.2019 bis. 13.11.2023 am Physikalisch-Chemischen Institut der Justus-Liebig-Universität Gießen unter Betreuung von Prof. Dr. Jürgen Janek angefertigt.

Ich erkläre: Ich habe die vorgelegte Dissertation selbstständig und ohne unerlaubte fremde Hilfe und nur mit den Hilfen angefertigt, die ich in der Dissertation angegeben habe. Alle Textstellen, die wörtlich oder sinngemäß aus veröffentlichten Schriften entnommen sind, und alle Angaben, die auf mündlichen Auskünften beruhen, sind als solche kenntlich gemacht. Ich stimme einer evtl. Überprüfung meiner Dissertation durch eine Antiplagiat-Software zu. Bei den von mir durchgeführten und in der Dissertation erwähnten Untersuchungen habe ich die Grundsätze guter wissenschaftlicher Praxis, wie sie in der „Satzung der Justus-Liebig-Universität Gießen zur Sicherung guter wissenschaftlicher Praxis“ niedergelegt sind, eingehalten.

Gießen, den 13.11.2023

_____

Yannik Moryson

Abstract

Today's lithium ion batteries (LIB) are approaching their theoretical limit of 250 Wh/kg. In order to meet the increasing demands for batteries due to the energy transition and the associated electrification of passenger transport, new concepts must be established. One promising possibility is the use of a lithium metal anode (LMA), which, in combination with solid electrolytes in solid-state batteries, has a capacity that is theoretically 10 times larger than the graphite electrodes currently used. The use of an LMA would thus be an important step towards e.g. long-range vehicles, but is associated with a lot of obstacles. The high reactivity of lithium causes unwanted side reactions with the used electrolytes. When liquid electrolytes are used, the high heat generated by dendrites in the event of short circuits and the associated fire hazard are major problems. Safety can be improved by using solid electrolytes, but the high reactivity remains a problem. Unwanted side reactions are not limited to the LMA, but also to the nickel-cobalt-manganese oxide (NCM) particles used at the cathode. Overall, these (electro) chemically induced degradations lead to poorer battery performance or capacity loss culminating in cell failure. In literature it is already reported that thin protective layers are applied to cathode or anode materials. It is now considered proven that protective coatings are unavoidable to ensure the long-term stability of LIBs. In literature, many processes and different materials are used for coatings, while the analysis of the protective layers in order to understand the protective effect often falls short.

In the context of this doctoral thesis, protective layers were therefore prepared for the cathode, by using ALD, and for the anode, by using plasma polymerization, suitable analytical methods were used for the investigation, and a guideline for reproduction of the analytics was prepared. In addition to the widely used methods such as X-ray photoelectron spectroscopy (XPS) and scanning electron microscopy (SEM), further useful complementary methods such as time-of-flight mass spectrometry (ToF-SIMS) and low-energy ion scattering spectroscopy (LEIS) or Raman spectroscopy were applied. The analysis results contribute to the comprehensive elucidation of the protective layers and interfaces. In symmetric Li cells, the electrochemical performance of the polymer protective layer was verified and the mechanical properties were determined by nanoindentation. Furthermore, the diffusion coefficients of oxygen ions in the native passivation layer of lithium and the polymer layer were determined by $^{18}O_2$ experiments.

The results in this dissertation, on the one hand, extend the analytical characterization of protective layers on battery materials by using new methods and, on the other hand, introduce with the plasma polymerization a forgotten method for the application of protective layers on LMAs. Without performing a proper analysis of the protective layers, it is difficult to draw conclusions about the causes of the protective effects and misinterpretations can easily occur. The work is an important step towards a systematic characterization of protective coatings in combination with their electrochemical performance to develop new coating concepts with the aim of making predictions about suitable materials.

Zusammenfassung

Die sich aktuell im Einsatz befindlichen Lithiumionenbatterien (LIB) nähern sich ihrem theoretischen Limit von 250 Wh/kg. Um die steigenden Anforderungen an Batterien durch die Energiewende und die damit verbundene Elektrifizierung des Personenverkehrs zu erfüllen, müssen neue Konzepte etabliert werden. Eine vielversprechende Möglichkeit bietet die Nutzung einer Lithiummetallanode (LMA), welche in Kombination mit Feststoffelektrolyten in Festkörperbatterien eine theoretisch 10-fach größere Kapazität als die aktuell verwendeten Graphitelektroden besitzen. Der Einsatz einer LMA wäre damit ein wichtiger Schritt in Richtung von z.B. *long-range* Fahrzeugen, ist aber mit vielen Hindernissen verbunden. Die hohe Reaktivität von Lithium sorgt für ungewollte Nebenreaktionen mit den eingesetzten Elektrolyten. Beim Einsatz von Flüssigelektrolyten ist dabei die große Hitzeentwicklung bei Kurzschlüssen durch Dendriten und die damit einhergehende Brandgefahr ein großes Problem. Die Sicherheit kann durch den Einsatz von Festelektrolyten verbessert werden, die hohe Reaktivität bleibt jedoch weiterhin ein Problem. Ungewollte Nebenreaktionen beschränken sich nicht nur auf die LMA, sondern auch auf die an der Kathode eingesetzten Nickel-Cobalt-Mangan-Oxid-Partikel (NCM). Insgesamt führen diese (elektro-)chemisch induzierten Degradationen zu einer schlechteren Performance der Batterie bzw. zu Kapazitätsverlust bis hin zum Zellversagen. In der Literatur wird darüber berichtet, dass bereits dünne Schutzschichten auf die Kathoden- bzw. Anodenmaterialien aufgebracht werden. Es gilt mittlerweile als sicher, dass Schutzschichten essenziell sind, um die Langzeitstabilität von LIB zu gewährleisten. Laut Literatur werden viele Verfahren und verschiedene Materialien zur Beschichtung eingesetzt, während die Analyse der Schutzschichten, um die schützende Wirkung zu verstehen, häufig zu kurz kommen.

Im Rahmen dieser Doktorarbeit wurden daher Schutzschichten für die Kathode, mittels ALD und für die Anode, mittels Plasmapolymerisation, hergestellt, geeignete analytische Methoden zur Untersuchung verwendet und ein Leitfaden zur Reproduktion der Analytik erstellt. Dabei konnten neben den in der Literatur vorherrschenden Methoden wie Röntgen-Photoelektronenspektroskopie (XPS) und Rasterelektronenmikroskopie (REM), weitere sinnvolle Ergänzungen wie Flugzeit-Sekundärionen-Massenspektrometrie (ToF-SIMS) und niederenergetische Ionenstreuungsspektroskopie (LEIS) oder Raman-Spektroskopie angewendet werden, um zur umfänglichen Aufklärung der Schutzschichten und Grenzflächen beizutragen. In symmetrischen Li-Zellen wurde die elektrochemische Performance der Polymerschutzschicht überprüft und die mechanischen Eigenschaften mittels Nanoindentierung ermittelt. Des Weiteren wurden die Diffusionskoeffizienten von Sauerstoff in der natürlichen Passivierungsschicht von Lithium und der Polymerschicht mittels $^{18}O_2$-Experimenten bestimmt.

Die Ergebnisse in dieser Dissertation erweitern durch die Vorstellung und Anwendung neuer Methoden zum einen die analytische Charakterisierung von Schutzschichten an Batteriematerialien und stellen zum anderen mit der Plasmapolymerisation eine vergessene Methode zur Aufbringung von Schutzschichten auf LMAs vor. Ohne die Durchführung einer gründlichen Analyse an den Schutzschichten sind kaum Rückschlüsse auf die Ursachen der Schutzwirkungen nachvollziehbar und es kann leicht zu Fehlinterpretationen kommen. Die Arbeit ist ein wichtiger Schritt in Richtung einer systematischen Charakterisierung von Schutzschichten in Kombination mit ihrer elektrochemischen Performance, um neue Schutzschichten zu entwickeln und Vorhersagen über geeignete Materialen zu treffen.

List of Abbreviations

ALE	atomic layer epitaxy
ALD	atomic layer deposition
ASEI	artificial solid electrolyte interface
CAM	cathode active material
CVD	chemical vapor deposition
ESCA	electron spectroscopy for chemical analysis
ISS	ion scattering spectroscopy
LEIS	low energy ion scattering
LCO	$LiCoO_2$
LIB	lithium ion battery
LNO	$LiNiO_2$
LMA	lithium metal anode
MLD	molecular layer deposition
NCM	lithium nickel cobalt manganese oxide
PDMS	C_2H_6OSi
PLD	pulsed laser deposition
PVD	physical vapor deposition
SE	solid electrolyte
SEI	solid electrolyte interface
SEM	scanning electron microscopy
SSB	solid-state battery
TEM	transmission electron microscopy
TMSP	$C_9H_{27}PSi_3$
TNNP	$C_{18}H_{12}N_3O_{10}P$
ToF-SIMS	time-of-flight secondary ion mass spectrometry
XPS	X-ray photoelectron spectroscopy

Table of contents

1. Introduction

The most used energy storage devices in our daily life are batteries. Especially, secondary lithium ion batteries are the standard in smartphones, laptops and other portable devices. Already in the 1970s intercalation electrodes were discovered and lithium cells were built by Whittingham but never commercialized due to safety concerns.[1] In the 1980s Goddenough looked at suitable cathode materials such as lithium cobalt oxide and prototype cells were built.[2] Both were awarded with the Nobel prize in 2019 for their work about lithium ion batteries. Finally, Sony and Asahi Kasei commercialized the lithium ion battery (LIB) in 1991. Since then a lot of work has been done and lithium ion batteries were optimized and almost reached their theoretical limits for the energy density of 250 Wh/kg or 700 Wh/L.[3,4] To fulfill the increasing demand of higher energy densities for batteries due to electrification of cars and substitution of fossil fuels new concepts have to be developed. One possibility is the use of a lithium metal anode (LMA), since lithium provides the highest theoretical specific capacity (3860 mAh/g) and lowest electrochemical potential (−3.04 V vs. standard hydrogen electrode).[3]

Reasons why no working LMA could be realized until now are the high reactivity of lithium metal and dendrite formation during cycling. In combination with the used liquid electrolytes an LMA provides a huge safety risk in electric devices because short circuits induced by dendrites can lead to ignition of the electrolyte.[5] To overcome this risk and also further improve the energy density the liquid electrolyte can be replaced by a solid electrolyte. Nevertheless, the high reactivity of lithium will still lead to reactions and formation of interphases between the LMA and the solid electrolyte (SE). Therefore, applying protection layers on top of the LMAs is of great interest to suppress side reactions and enable stable cycling in lithium ion and solid state batteries.[6]

Not only the LMA suffers from side reactions and degradation during battery cycling, also the cathode materials undergo structural changes and (electro-)chemical reactions. In state-of-the-art LIBs transition metal oxides with the formula $LiMO_2$ (M = transition metal) are commonly used as cathode materials. Especially mixtures of Co, Mn, and Ni as so called NCM cathode active materials are present. During battery cycling and delithiation of the NCM, the NCM particles shrink and will grow again during lithiation. This so-called breathing induces mechanical stress and can lead to cracks inside of the particles and contact loss with the electrolyte, which results in capacity fading.[7,8] Additionally, oxidation of the SE and the formation of an solid electrolyte interface (SEI) lowers the capacity retention. To suppress the degradation of the CAMs protective coatings are widely applied in literature.[9]

As protective coatings for both anode and cathode are of great importance and interest to enable stable cycling for next generation batteries, comprehensive analyses are necessary. In literature this is often not the case and only the improvement of the electrochemical performance is highlighted without a systematic analyses of the coating material and interfaces. [10–13] While the improvement of the electrochemical performance is at last the aim of protective coatings, the thoroughly analysis e.g. of possible contaminations is necessary to figure out the reasons for success or failing of coatings. For lithium, the lack of understanding of the pristine metal and passivation layer also complicate further the analysis. Otto et al.[14,15] characterized the native passivation layer of lithium and its influence in

ASSBs to help better to understand the underlying processes. Therefore, a combination of a well-known substrate, well-engineered coating techniques and a comprehensive analysis is necessary to develop protective coatings for next generation batteries.

This doctoral thesis focuses on the fabrication and characterization of protective layers for CAMs and LMAs. The thesis should help the reader to understand what techniques are suitable for CAM/LMA coating analyses and what pitfalls have to be avoided. Additionally, LEIS was introduced as a very powerful technique to investigate CAM coating surfaces. As well as the plasma polymerization as a combination of a cleaning and coating technique in one step for LMAs.

In the first publication of this thesis, entitled: *"Analyzing Nanometer-Thin Cathode Particle Coatings for Lithium-Ion Batteries – The Example of TiO_2 on NCM622"* a comprehensive analysis of the coating layer TiO_2 is given and the advantages and disadvantages of different analytical methods are discussed, see chapter 3.1. Besides the established methods Raman spectroscopy, ToF-SIMS imaging and LEIS were used to examine the coating layer and especially its surface with LEIS. Even the established methods such as XPS, REM/SEM or TEM exhibit pitfalls during the analyses, which are discussed and guidelines are given to avoid these in future analyses. Overall this publication should help the reader to see which information can be accessible with their available techniques and which is the best way to set up the analyses to gain the desired information.

In the second publication of this thesis, entitled: "*In-Depth Characterization of Lithium-Metal Surfaces with XPS and ToF-SIMS: Toward Better Understanding of the Passivation Layer*" the composition of the native passivation layer of different lithium samples with XPS, ToF-SIMS and EDX was elucidated, see chapter 3.2. The combination of the quantification by XPS and depth resolution of ToF-SIMS depth profiling enabled a 3D rendering of the passivation layer and layer thickness determination. Common pitfalls when analyzing lithium are highlighted, such as the lithium plating, which was misinterpreted as electron beam cleaning in previous studies. Overall the second publication gives a comprehensive analysis of different lithium metal samples and is an important prerequisite for further modification of LMAs to improve their electrochemical performance.

In the third publication of this thesis, entitled" Protective *Coating for the Lithium Metal Anode Prepared by Plasma Polymerization* "a protection layer for LMAs by plasma polymerization with the precursor 1.4-bis(trifluoromethyl)benzene was fabricated and analyzed and the electrochemical performance of symmetric cells was improved, see chapter 3.3. Plasma polymerization gives the opportunity to remove the native passivation layer of lithium and deposit a new passivation layer in one setup. The layer was characterized by ToF-SIMS, XPS and the mechanical properties were examined by nanoindentation. The analyses showed a polymer formation with a Parylene HT® like structure. Cycling experiments with cells of coated lithium electrodes showed stable cycling for over 300 h at low overpotentials at current densities between 0.1 and 1 mA/cm^2 Additionally, $^{18}O_2$ diffusion experiments were conducted to examine the protection against oxygen of the plasma layer. Even though the diffusion coefficient of oxygen in the plasma layer is much greater than in the native passivation layer of oxygen, the combination of thickness and diffusion coefficient is sufficient to protect the LMA against oxygen for at least 30 minutes.

Overall, the results of this thesis highlight the importance of a reliable characterization and combination of an electrochemical performance of protective coatings for CAMs and LMAs

to better understand the underlying processes and develop specific new coatings for next generation batteries. In literature most often only the electrochemical performance is highlighted, while the layer characterization is neglected. With the given guidelines in this thesis it is possible to link a comprehensive analytical analysis with the electrochemical performance to compare different coatings and draw conclusions about material properties to further improve protective coatings.

2. Fundamentals

In this chapter an overview over the most important properties about electrode materials, coating techniques and surface analysis methods to understand this doctoral thesis are given. At first the cathode materials and degradation processes are summarized. Then different coating approaches and analyses techniques are described. After that the lithium metal anode and its passivation layer are discussed and possible ways to enable a working lithium metal anode in a battery are shown.

2.1 NCM

In this chapter the properties of nickel cobalt manganese oxide-based cathode materials and suitable coating materials for them, to suppress degradation processes during battery cycling, are discussed

2.1.1 Material

As a cathode active material (CAM) in state-of-the-art lithium ion batteries (LIBs) and all-solid-state batteries (SSBs) layered structural compounds with the formula $LiMO_2$ (M = transition-metal) are mainly used. Theoretically a capacity of more than 270 mAh/g and voltages over 3.6 V versus lithium metal could be achieved.[16] While pure $LiNiO_2$ (LNO) can reach the highest capacity at lowest costs, it is also the one with the highest capacity fading, mainly due to phase transformation into rock salt-like structure. [9,17] The LNO can be stabilized by the addition of Co and Mn, whose layered structure remains unperturbed during lithium insertion.[18] The combination of Ni, Co and Mn leads to $LiNi_xCo_yMn_zO_2$ lithium nickel-cobalt-manganese oxide (NCM). The most common NCMs are NCM111 (x = 0.33), NCM622 (x = 0.60) and NCM811 (x = 0.80). NCM material is commercially available as polycrystalline spherical secondary particles with the size of about 10 µm, which consist of primary particles with the size of several hundred nanometers. Even though the cycling performance of NCM is improved in comparison to LNO or $LiCoO_2$ (LCO) it is not possible to reach the preferred performance in terms of stability and capacity without surface modification of the NCM due to degradation processes, which will be discussed in the next sections.[19]

2.1.2 Degradation Processes

The degradation processes on the cathode side do not only consist of structural changes of the NCM during lithium insertion and extraction but also of (electro-)chemical reactions.[20] Koerver et al.[8] investigated the huge irreversible capacity loss after the 1st cycle for NCM811 and β-Li_3PS_4 for SSBs. and with a 50:50 mixture of EC/EMC for LIBs. While

the Coulomb efficiency for the liquid cell was at 85.9 % the SSB only got 70.5 %, indicating that the degradation is more significant for SSBs. XPS measurements of pristine β-Li_3PS_4 and β-Li_3PS_4 after contact with NCM811 showed no significant difference, which rules out a non-stable SEI as a reason for the capacity fading. With SEM images of uncycled, charged and cycled NCM811/ β-Li_3PS_4 composite material they could show that the NCM particles loose contact with the solid electrolyte (SE) during the charging process due to shrinking. Therefore, these particles are no longer fully electrochemically accessible, which results in capacity fading. Kondrakov et al.[21] also looked at the volume changes for different NCM materials during cycling. Although the high Ni-NCMs have a higher specific capacity in comparison to low Ni-NCMs, the reversible volumetric change of the unit cell of NCM811 is more than four times greater than the one of NCM111. The highest contraction was found at E > 4.0 V vs Li and resulted in microcracking. Koerver et al.[7] compared the volume changes of different electrode materials during delithiation. In Figure 1 the volume change during delithiation and the partial molar volume of lithium for two-phase electrode materials can be seen. Except of LCO all materials shrink during delithiation and show a positive partial molar volume, respectively.

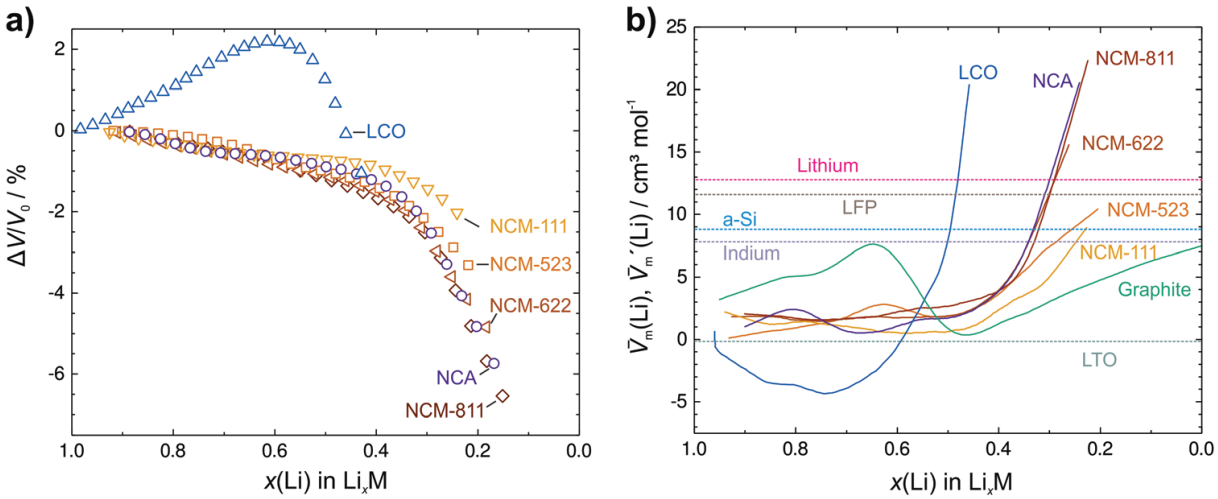

Figure 1: a) Change of the unit cell volume for different CAM materials vs. the state of lithiation. b) Partial molar volume of lithium $\overline{V}_m$(Li) for homogeneous storage phases and apparent partial molar volume of lithium $\overline{V}_m'$ (Li) for electrode materials with two-phases.[7] Reprinted with permission. © The Royal society of Chemistry.

These results underline that in SSBs the volume change of (both) electrodes can build up huge pressure in operating cells, which will lead to cracks, deformation and ultimately to cell failure.

At the interface of the cathode material and the electrolyte chemical reactions occur and the formation of an SEI takes place. Additionally, electrochemical instability of the solid electrolyte at high electrode potentials can add to these side reactions and lead to the formation of new passivation layers, which increase the interfacial resistance and result in capacity loss.[20] Walther et al. used XPS and ToF-SIMS imaging to visualize the

degradation products of NCM622 and Li_6PS_5Cl argyrodite. The results could confirm that NCM materials and thiophosphate based solid electrolytes form oxidized S and P species, such as Li_3PO_4 or Li_2SO_4. These decomposition products could be visualized as a compact shell around the NCM particles and therefore increase the cell resistance. Additionally, the decomposition process is much larger for cycled cells in comparison to uncycled cells. This shows that even if the interface between the NCM and the solid electrolyte might be stable without cycling, it can change drastically during cycling.[20,22] Since the capacity can also be boosted due to reduction of the NCM particle size, additional interfaces with possible degradation processes are formed.[23] To overcome these challenges and still be able to use the ideal particle size and solid electrolytes, it is mandatory to modify the surface of the NCM particles with e.g. coatings, which will be discussed in the next section.

2.1.3 Coating Approaches

Next generation LIBs/SSBs can only be realized with surface modifications of the CAM surface such as coatings or doping. In the literature are a lot of different coating approaches present.[24–31] Still the underlying mechanisms and interpretations are not clear. First, the addition of a coating layer adds two additional interfaces, one between the NCM and the coating and one between the coating and the SE. Considering the coating thickness in the few nm range these interfaces are even smaller and harder to analyze than the original one between NCM and SE. But especially the interfaces are the most important areas to be investigated in order to understand the protective effect of the coating. In SSBs the ideal coating should behave like a SE, which is stable against oxidation, this means it should have a high ionic conductivity and should be electronically isolating.[9] If the coating is realized as a core shell approach the question arises how the NCM particles can still be electrochemically active if completely isolated by the coating. Since these kinds of cells are working it is believed that the coating cracks or is thinned out and electron pathways become accessible.[9] Additionally, capacity fading can be observed, which supports the theory of cracks and partial destruction of the coating.[9] In Figure 2a these processes are visualized. If the coating is hard, i.e., Young's modulus is about 200 GPa, it will crack during cathode composite mixing, while softer materials, with Young's Modulus of about 20 GPa, will deform and electronic percolation between the NCM particles becomes possible.[9]

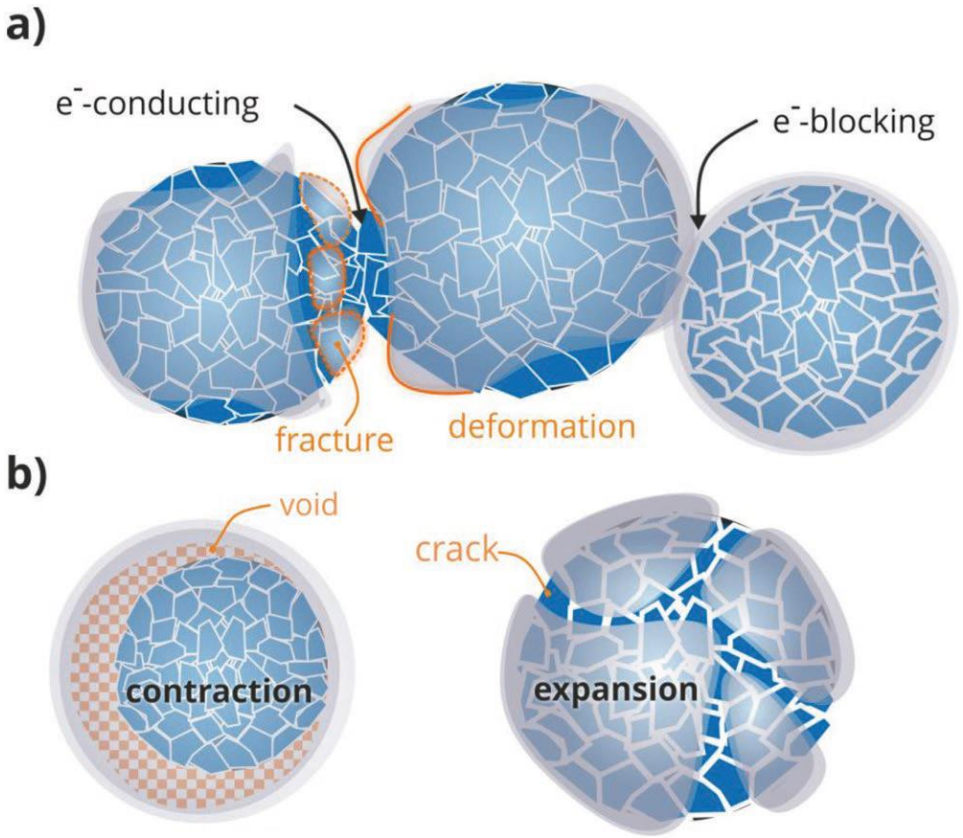

Figure 2: Schematic illustration of CAM particles and coatings. a) Possible formation of electronic pathways between CAM particles due to cracking or deformation of the coating during processing of composite cathodes b) Influence of the volume change of the CAM particles on the coating. If the coating cannot accommodate the expansion/contraction of the CAM particles it will either crack or lead to delamination and the formation of voids.[9] Reprinted with permission. © Wiley-VCH Verlag GmbH & Co. KGaA.

As already mentioned the ideal coating should behave like a SE and prevent the oxidation of the pristine SE by shielding against the highly reactive lithium, limit the interdiffusion between SE and CAM by providing an additional diffusion barrier and suppress cracking of the CAM with increased mechanical integrity. Additionally, the charge transfer resistance of the CAM for Li^+ can be lowered by adding high *k* materials at the surface and reduce the space charge regions.[32,33] In Figure 3 these properties are summarized.

Respecting the mentioned properties suitable coating materials are:

Binary oxides such as ZrO_2, Al_2O_3, TiO_2.[10,26,27,31,34] These binary oxides are high-*k* materials but show no sufficient Li^+ ion conductivity. In liquid cells the electrolyte can penetrate into the coating and enable Li^+ ion pathways but in SSBs the coating material has to be lithiated either by reaction with lithium compounds such as Li_2CO_3 or electrochemically during cycling.[9]

Ternary oxides already include lithium in comparison to the binary oxides, and therefore, show sufficient Li^+ ion conductivity. Coating materials such as (amorphous) $LiNbO_3$ are established as standard coating for SSBs due to its ionic conductivity of 10^{-5} S/cm and electronic conductivity below 10^{-11} S/cm.[9,29,35,36]

(Organo)phosphates such as tris(4-nitrophenyl) phosphate (TNPP) or tris(trimethylsilyl)phosphate (TMSP) are used in LIBs with liquid electrolyte due to before mentioned Li^+ ionic conductivity issues.[37] For SSBs fast ionic conductor NASICON-like phases are a possible approach, such as $Li_{1.5}Al_{0.5}Zr_{1.5}(PO_4)_3$.[38]

There are several methods to deposit these coating materials onto the CAMs such as wet chemical approaches e.g. sol-gel processes or spray coating, chemical vapor deposition (CVD), pulsed laser deposition (PLD) and atomic layer deposition (ALD).[22,39,40] With the sol-gel process binary and ternary oxides could be successfully deposited on the CAM particles.[34,36,39,41–43] The achieved layer thicknesses were around 6 – 10 nm and could be controlled by changing the weight percent of the precursor. Since the precursors must be dissolved in alcohol, hydrolyzed with water and afterwards calcinated the process is relatively costly and also the liquids are vulnerable to contaminations. Additionally, the layer thickness is not really well controllable.

Physical or chemical vapor deposition can also be used to coat the CAMs.[44,45] Both of these methods are well established for thin film preparation and corrosion protection on planar substrates. For more challenging substrates with a distinct and pronounced topography or complex geometry these techniques are not ideal due to the oriented nature of the process, which leads to thicker layers on surfaces faced to the source in comparison to surfaces turned away from the source.

Since conformity and layer thickness control are very important for this kind of coatings ALD is an interesting method to apply coatings and will be discussed in more detail in a separate chapter.

More information about coatings on CAMs can be found in the reviews of Culver et al.[9] and Liu et al.[16]

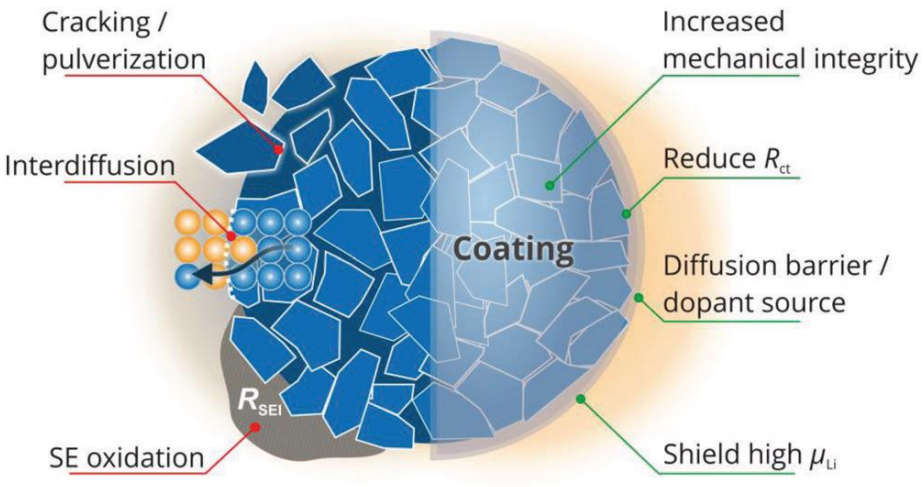

Figure 3: Schematic illustration of the main degradation phenomena at the interface between the CAM particles and the solid electrolyte. The beneficial properties of the coating

layer are also shown.[9] Reprinted with permission. © Wiley-VCH Verlag GmbH & Co. KGaA.

2.1.4 Analytical Challenges of CAM Coatings

The analysis of CAM coatings is quite challenging. In literature, XPS, SEM and TEM are the most common used techniques. An ideal analysis requires methods with a high spatial resolution and a low detection limit. For XPS the measurement area is in the 100 µm range and can be reduced to about 5 µm which comes with a huge loss in intensity and large extension of measurement time.[20] Additionally, spectra of low concentrated elements are even harder to measure and evaluated. TEM for example can provide a sufficient spatial resolution but cannot provide real chemical information and gives only information about single particles and not the complete CAM. To fully understand the properties of the protective coating, the surface and interfacial reactions, only a combination of different methods with different strengths and weaknesses can provide the needed information. Therefore, additional methods have to be applied for CAM coating characterization. ToF-SIMS imaging of CAM coatings and degradation processes gained more popularity in the last years.[20,30,46] Walther et al. were among the first who looked at CAM degradation and coatings with ToF-SIMS.[20,35] With ToF-SIMS imaging it is possible to visualize the degradation products around the particles for a large area of about 200 µm. It is also possible to use it semi-quantitatively and compare the amount of degradation products on different samples in spectrometry mode. Other methods like Raman spectroscopy or low energy ion scattering (LEIS) are very rarely used on CAM coatings but can provide very useful information since LEIS is the most surface sensitive method and Raman spectroscopy can give structural information without much experimental effort.[47,48] In Figure 4 the detection limit vs. the lateral resolution of possible methods to analyze CAM coating are shown in a simplified way. This illustration underlines the need of combination of different methods for a comprehensive CAM coating analysis.

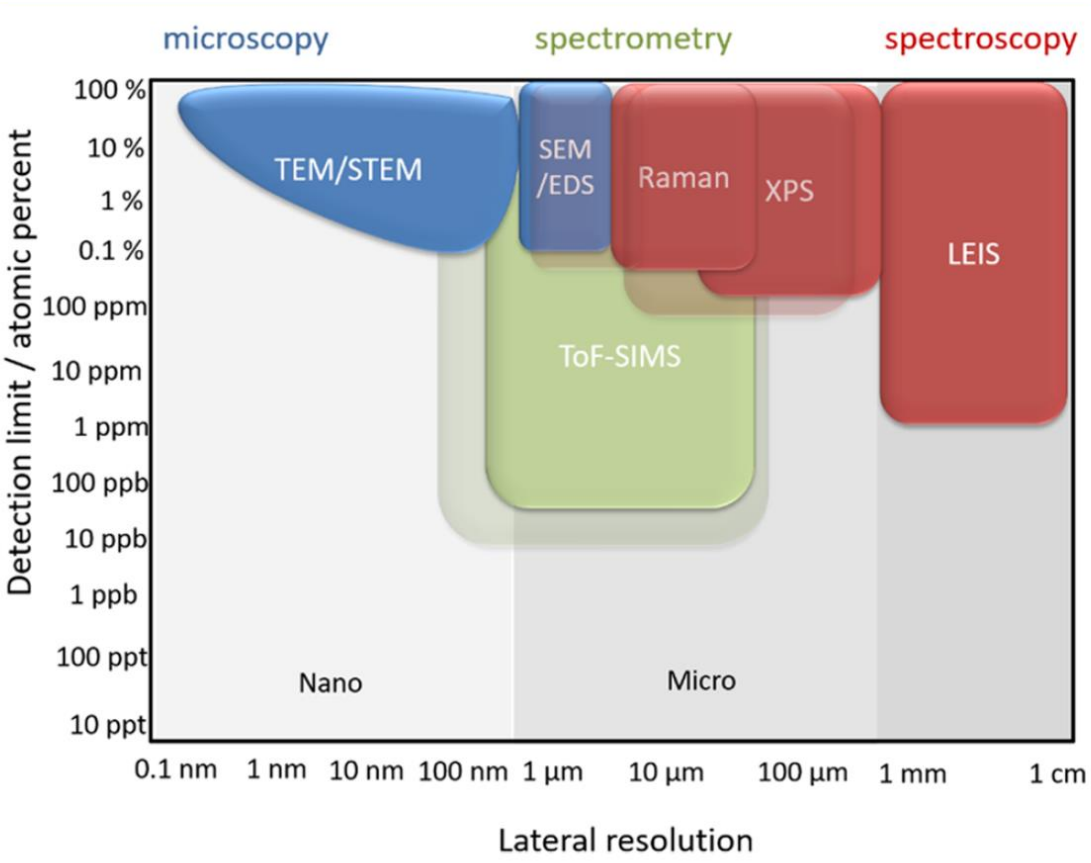

Figure 4: Detection limit vs lateral resolution of techniques suitable for (CAM) coating analysis. The areas for lateral resolution and detection limit depend on the examined samples and are not sharp. The colored areas represent measurements on common samples and the transparent areas indicate the limits when measuring ideal systems.[49] Reprinted with Permission. © American Chemical Society.

2.1.5 Conclusions

The development of new CAM materials for state-of-the-art LIBs/SSBs is strongly connected to surface modification since mechanical and (electro)chemical degradation cannot be avoided otherwise. For surface modification a lot of different materials are thinkable, which should show ideally a high Li^+ ion conductivity and a low electronic conductivity such as a SE. The coating materials can be applied by different methods such as wet chemically approaches or from the gas phase. One method that shows good controllability and conformity is ALD and will be discussed in detail later, see chapter 2.3.1. The lack of comprehensive coating analysis in literature still hamper the complete understanding of the protective properties of the coatings. Therefore, it is necessary to combine and apply new techniques, such as LEIS, Raman, ToF-SIMS with the established ones, XPS, SEM, TEM to fully understand the reactions and processes on the coating/CAM interfaces.

2.2 Lithium

In this chapter the basic properties and importance of metallic lithium for next generation batteries are explained. The reactivity and native passivation layer of lithium are discussed and artificial protection layers as well as difficulties during analyses are shown.

2.2.1 Lithium Metal Anode

The lithium metal anode is seen as the holy grail for next generation LIBs and also the precondition for high energy density SSBs.[4] Lithium has a theoretical Coulomb efficiency of 3860 mAh/g and a standard potential of −3.04 V versus the standard hydrogen electrode.[50,51] Despite these perfect properties of lithium the application comes with a lot of different challenges. The main challenges are the high reactivity of lithium with water and residual gases during cell preparation, the side reactions with the electrolytes and formation of dendrites during cycling, which can lead to short circuits and cell failure.[51]

The high reactivity of lithium is probably the most severe issue. Lithium is stored or handled in gloveboxes under Ar atmosphere or in dry air. The main contaminations, which can come in contact with lithium are residuals of the atmospheric gases, such as oxygen, nitrogen, carbon dioxide and water. In the second publication of this thesis and in a different work we looked at the native passivation layer of commercial lithium foils, the reactivity of lithium with the residual gases and the formation of passivation layers, which was published by Otto et al.[14,15] The results showed that commercially available lithium foils have a native passivation bilayer on top, which consists of Li_2CO_3/LiOH and Li_2O in contact with lithium metal. The layer thickness is in the range of few nanometers. If the passivation layer is not damaged, it can adequately protect the lithium from oxidation during storage under normal glovebox conditions. If the lithium foils are not properly sealed a growth of the passivation layer over 50 nm in 10 weeks is possible.[15] Additionally, damaged passivation layers lead to a reaction with nitrogen to fully conversion to Li_3N of the foils. In this study we also investigated the preparation of fresh lithium metal surfaces from a lithium rod. These experiments showed that the freshly prepared lithium metal surface was already re-passivated as ToF-SIMS and XPS measurements were conducted. The newly formed passivation layer consisted mostly of LiOH and Li_2O with very low amounts of Li_2CO_3. This shows on the hand that the residuals in the glovebox and transfer modules and analyzing machine chambers are sufficient to react with the lithium foil and on the other hand that the formation of LiOH with water is the initial reaction product, which then can convert to Li_2CO_3.[14]

These results emphasize the importance of proper handling of lithium foils for battery usage. In SSBs the thickness of the passivation layer has a direct influence on the interface resistance between the lithium anode and the SE.[15] In LIBs the homogeneity of the passivation layer is even more important as inhomogeneities lead to inhomogeneous electric fields and to dendrite formation.[52] In the next chapter the suitability of the native passivation layer as a protection layer for LIBs is discussed.

2.2.2 Native Passivation and SEIs/ASEIs

As already mentioned before the native passivation layer of lithium consists of a bilayer of lithium carbonate/lithium hydroxide and lithium oxide. This bilayer is sufficient to store lithium foils under normal glovebox conditions but it is not stable during battery cycling. One main problem of the native bilayer is its inhomogeneity and inhomogeneous organic impurities at the surface.[53] Both features lead to an unequal formation of a solid electrolyte interface (SEI) and unequal plating of lithium during battery cycling, which results ultimately in dendrite formation.[52,54,55] Especially in the first battery cycle the formation of the SEI leads to huge capacity losses, which cannot be recovered. During cycling the dendrites can either grow from the anode to the cathode and create a short circuit or react with the (liquid) electrolyte, which creates electrochemical “dead lithium” and also consumes electrolyte. Homogenization of the passivation layer can help to reduce dendrite formation but for long term cycling stability homogenous artificial solid electrolyte interfaces (ASEI) have to be designed.

These ASEIs shall prevent reactions between lithium and the electrolyte and minimize the formation of dead lithium and electrolyte consumption. The requirements for ASEIS are similar to the ones for protective coatings for CAMs. The layers should be electronic isolating and Li^+ ion conductive and withstand the volume changes. Additionally, it is believed that layers with a Young´s modulus of >10 GPa are mechanical capable of suppressing dendrite growth.[56] ASEIs can be divided into inorganic and organic layers or mixtures of both. Inorganic layers are often stable against lithium and the electrolytes and can reach the necessary Young´s modulus values, but they tend to break during cycling due to the volume changes. To deposit thin inorganic layers on lithium different approaches in literature are present. The ALD for example can be used to deposit LiF or Al_2O_3 on lithium.[57–59] Theoretically all coatings which can be applied on CAMs can be deposited on lithium and used for ASEIs, since the requirements are comparable. The main problem during deposition is the low melting point of lithium of 180°C. Therefore, established ALD processes have to be changed or reworked, to work at lower temperatures or with different precursors. The processes for Al_2O_3 can be realized at 150°C and are just under the melting point of lithium. Due to the high temperature, diffusion and reactions between the deposited ALD layer and the lithium may occur. For Al_2O_3 the formation of a $LiAlO_x$ phase can be observed. The lithiation of the ASEI may again not be a disadvantage, since ionic pathways have to be formed to enable battery cycling. The layer growth rate is much larger in the first ALD cycles since the reactions are not self-limited until a dense Al_2O_3 layer is formed.[57] Nevertheless, coating lithium with Al_2O_3 greatly enhances the wettability with liquid electrolytes and cycle life up to 2 times in symmetric cells and can prevent the huge capacity loss in the first cycles in Li│S batteries.[57,58]

LiF is considered a suitable component for ASEIs due to its Li^+ ion conductivity in the range of about 10^{-9}–10^{-13} S/cm among other features and can also be deposited by ALD.[59–61] Chen et al.[59] developed a low temperature ALD process to successfully deposit crystalline LiF with a shear modulus of 58 GPa on lithium. The Coulomb efficiency in Li-Cu cells was 99.5% for 170 cycles and enabled stable cycling 4 times longer than for uncoated LMAs. Yuan et al.[60] produced a porous LiF layer on Li by reaction with NH_4HF_2. The layer enabled dendrite free lithium plating and stable cycling for over 520 h at a current density of 1 mA/cm^2. They assumed that the lithium is first plated into the pores and will then spread

flat over the anode. Other wet chemical approaches with e.g. dip coating or spray coating of Al_2O_3 nanoparticles or phosphorene are also possible.[62–64]

Other than the hard, inorganic compounds also soft polymers with their (visco)elastic or rubber-like properties are possible approaches as ASEIs. Poly(dimethylsiloxane) (PDMS) was successfully applied on lithium via dip coating and spray coating.[65,66] With both techniques the cycle life of Li│Cu and symmetric Li│Li cells could be improved in comparison to cells without the PDMS coating, but the spray coating process seems more promising since HF treatment is not required. Li et al.[66] also showed that the PDMS layer can protect against corrosion in Li│S cells for more than 100 cycles. Already in the 1990s Takehara et al.[67,68] used plasma polymerization to deposit 1,1-diflourethene on cleaned lithium foils. The produced layers showed an ionic conductivity of $3 \cdot 10^{-8}$ S/cm, when immersed in 1 M Li perchlorate/propylene carbonate solution and a surface energy of 20 dyn/cm (0,02 J/m^2) and lead to a smoother deposition of lithium during cycling. A big advantage of the plasma setup is the possibility of combining a cleaning step and coating step in one process chamber since different plasma gases can be used. The plasma polymerization also enables a variety of different precursors as theoretically all monomers which can be vaporized are usable. The plasma polymerization process will be discussed in a separate chapter later, see chapter 2.3.2.

To combine the properties of both types, hybrid ASEI layers are a possibility. Kozen et al.[69] combined an electrochemically polymerized organic DOL layer with an ALD LiPON layer. The hybrid layer combination with a thickness of around 815 nm suppresses dendrite formation for over 100 cycles at a current density of 2 mA/cm^2 in symmetric Li cells. Chen et al.[70] used the molecular layer deposition (MLD), a variation of the ALD process to apply Alucone layers on lithium. The Alucone layers have a Young's modulus and hardness of one order of magnitude smaller compared to Al_2O_3 layers but have the same conformity and layer thickness control. In the Alucone structure PEO is cross-linked to aluminum and layers of 3 and 6 nm were deposited. In symmetric Li cells the Alucone coated LMAs showed stable cycling behavior for over 200 h at 1 mA/cm^2 with the 6 nm layer showing lower overpotential than the 3 nm layer. The 6 nm Alucone layer also showed improved performance in Li│S batteries with a sulfur loading of 5 mg/cm^2.

For a more detailed overview about different coatings look at the review from Yu et al.[56]

2.2.3 Analytical Challenges of Lithium Metal

For all battery materials of course the cleanliness of the preparation environment, transfer modules and analytical machines is important due to the high reactivity of lithium. A problem which can be easily overlooked is the sample change during the analysis due to inappropriate handling. On the one hand beam damage can change the sample and show false degradation products but also lithium metal plating may occur, when electron beams are present and the samples are grounded. In the second publication of this thesis, which is published by Otto et al.[14] we observed lithium metal plating during XPS measurements,

when using Cu tape and the electron neutralizer. In other studies, the phenomenon was described as electron cleaning of lithium foil, which is misleading.[71] It is more accurate to describe it as electrochemical plating of lithium, since the electron beam causes a potential difference between the surface of the sample and the grounded sample holder. Lithium ions will then migrate through the native passivation or protection layer to the surface to compensate the negative charge and form lithium metal with the electrons. As a result, lithium metal will be detected as if the passivation layer had been removed, which in fact is still underneath the freshly prepared lithium metal. In Figure 5 the process can be seen and is also relevant for e.g. ToF-SIMS with flood gun neutralization or SEM.

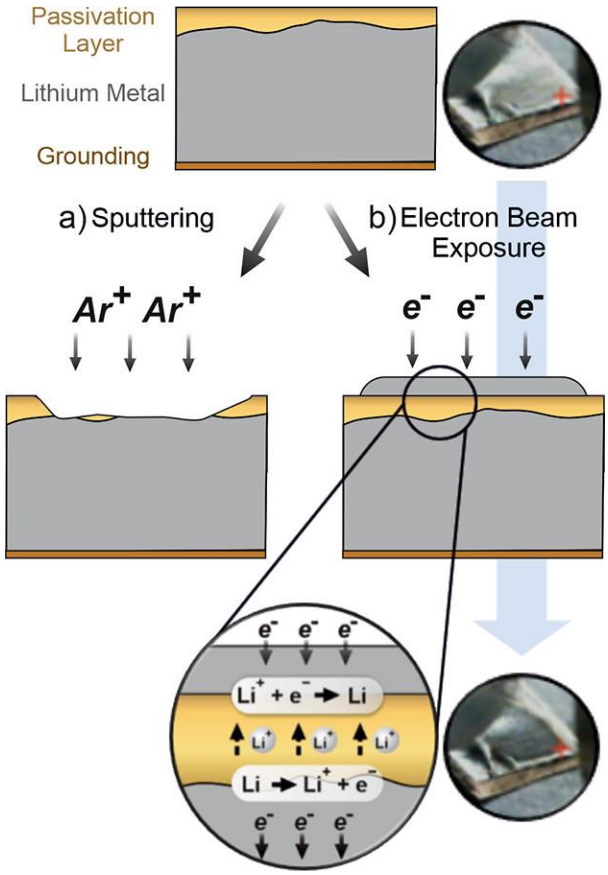

Figure 5: Schematic sketch of the difference between sputter cleaning a) and lithium plating induced by an electron beam on a grounded lithium sample b). The photos show the lithium foil before plating and after plating (5 min) in the XPS with electron neutralizer. Reprinted with Permission. © American Chemical Society.

To get an idea about the change of the sample during a measurement, lithium metal was plated inside the XPS and the surface was measured right away and after a waiting time of 2 hours. It is also recommended to measure e.g. the O 1s in all measurements at the start and again at the end of every measurement cycle to estimate the degradation. Both results showed a significant change of the surface composition. Especially the formation of Li_2O and LiOH was detectable by this method. The results are also important for

quantification of the different passivation layers components by XPS. Since all detail spectra are measured at different times while the composition is changing a reliable quantification is not possible. E.g., if the O 1s is measured first it will show less Li_2O or LiOH than the Li 1s spectrum, which is measured later. While with XPS the sample degradation during a measurement can be easily tracked it is not so trivial with other methods.

2.2.4 Conclusions

In literature a variety of different ASEIs has been presented. It is still important to look at different approaches to design new ASEIs with the ideal properties, such as a high Li^+ ionic conductivity (10^{-4}−10^{-3} S/cm), single ion transport, Young´s Modulus > 10 GPa but still enough flexibility to withstand volume changes without breaking, and shielding against side reactions. Additionally, the desired ASEI should be preferably applied by a large-scale method and should spare dangerous or hazardous precursors. A combination of all these different aspects is challenging but enables the future implementation of LMAs. Due to the high reactivity and electrochemical activity of lithium the handling during the coating process and analyses is critical to avoid contamination or false results.

2.3 ALD and Plasma Polymerization

In this chapter two techniques to apply protective coatings on CAMs or LMAs are explained in more detail. The ALD was chosen due to its good controllability and large-scale potential. The plasma polymerization combines the possibility of a cleaning step and deposition in one setup and also offers a huge number of possible precursors.

2.3.1 Atomic Layer Deposition

The atomic layer deposition is a self-limiting variation of a CVD process and uses alternate pulsing of precursor gases onto the substrate surfaces to achieve chemisorption or surface reaction, which result in layer growth. During the cycles of the precursor the reactor is purged with inert gases such as Ar or N_2. Before deposition the process parameters such as pulse length and temperature are adjusted to reach stable growth conditions, which results in constant growth rates.[72]

Originally, the ALD was developed as atomic layer epitaxy (ALE) and was used to deposit insulator films for electroluminescent flat panel displays. Since the 1990s the interest in ALD rose from the microelectronics side, which requires thin, conform coatings on small dimension devices. Since then the ALD was used in more and more areas such as, catalysis, nanotechnology or battery materials.[40,73–75] The only drawback of the ALD process is the comparable low growth rate in the range of a few Å/cycle but since the desired layer thicknesses in the mentioned fields tend to decrease over the years it is still an efficient method. The ALD exhibits also a great large scale potential which is important for the commercial production of protective coatings.[76] More information about the history of ALD and possible fields of use can be found here.[76,77]

2.3.2 Plasma Polymerization

The plasma polymerization is a technique to produce (ultra)-thin, pinhole-free polymer-like layers with a defined structure but variable composition in comparison to conventional polymers. The properties of the produced polymer-like layers arise from the functional groups of the used monomer, which stay mostly intact during the polymerization process.[78] Plasma polymerization reaches back to 1796 and was further explored in the 19th century with the arc synthesis of acetylene. Extensive research was done in the 1950s and 1960s and attempts were made to propose mechanisms (ion chain mechanism[79], radical mechanism[80]) for polymerization and parameters (Yasuda factor[81]) to compare different plasma conditions. The discussion about the underlying mechanism is still present in the last years.[82]

Plasma polymer layers are used as coatings for solids, membranes, semiconductors, metals or textiles. With the right choice of precursor monomer properties such as corrosion-inhibition, anti-fogging, chemical-, scratch- and abrasion resistance, adherence, lubrication, flame resistance, permeability, antistatic, barrier and optical characteristics are

possible.[78] In the 1990s it was also applied on lithium metal for LIBs but was not further pursued and can nowadays often be found in biomaterial research. [67,68,83–85]

As the name already suggests plasma polymerization works with plasmas, which is also called the fourth state of matter and is a gaseous mixture of free electrons, ions and neutral atoms/molecules. Laboratory plasmas are often produced by electromagnetic fields. A big advantage of plasma (polymerization) processes is the combination of a possible cleaning step and coating step in one setup by variation of the used gases. Inert gases such as Ar can be used for cleaning or sputtering of the sample, while reactive gases such as N_2 or O_2 may form nitrides and oxides. Plasma chambers are often either inductively or capacitively coupled and examples for possible setups can be found here.[86,87]

For this doctoral thesis an inductively coupled rf-plasma chamber was modified to enable air-tight sample transfer of the lithium samples from a glovebox to the plasma chamber. Due to the high reactivity of lithium this is especially important. The self-made transfer module can be seen in Figure 6. The sample can be driven into the z-axis manipulator, which is than closed by a hand valve. After attaching the transfer module to the plasma chamber the area between both of them can be flushed with Ar and pumped before the sample can be driven into the plasma reactor to the desired position.

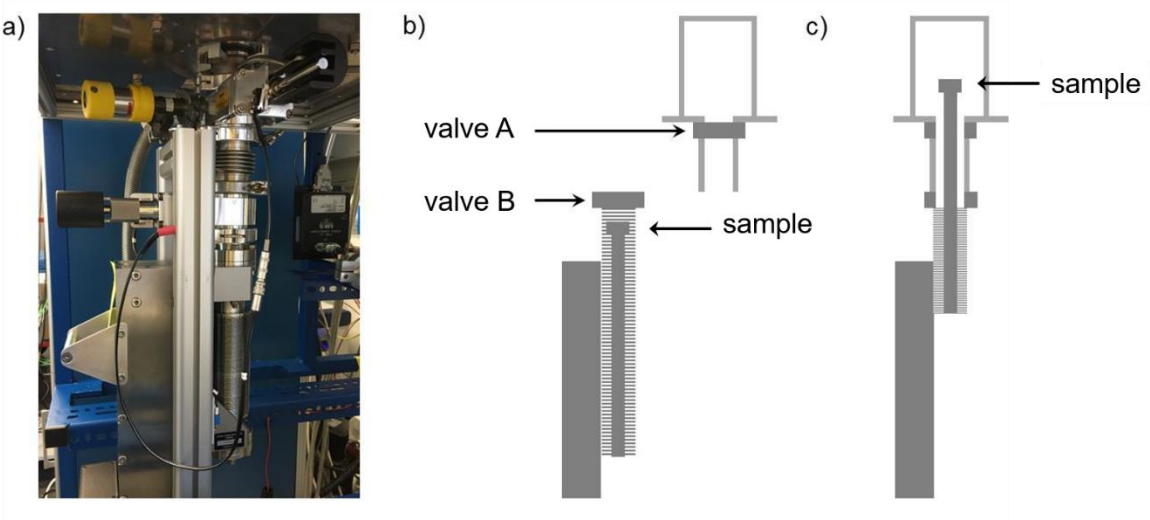

Figure 6: Photo a) and schematic sketch of the self-made transfer module b), c). The sample can be driven automatically from the storage position inside the transfer module to the process position in the plasma reactor. The transfer module and the plasma chamber can be closed with two separate vales, the pumping connection is between both valves to work as a lock.

As already mentioned the high reactivity of lithium can be problematic. That is why plasma cleaning has several advantages in comparison to a mechanically cleaning or a liquid approach. Before introducing lithium into the plasma chamber residuals of water and oxygen

must be removed by gas purging and pumping cycles to avoid side reactions. After that Ar is used as plasma gas to remove the native passivation layer of the lithium. Since Ar is inert and also used as an atmosphere gas in gloveboxes the conditions are ideal to suppress side reactions or a re-passivation of the lithium. If lithium is cleaned mechanically or in liquid solutions, impurities often lead to unwanted side reactions and the lithium gets much dirtier than without a treatment.

Another big advantage of the plasma polymerization is the large choice of possible precursors for the plasma layers. Plasma polymerization might be the only technique were everything, as long it exists in the gaseous state can be a possible precursor. For this work a gas washing bottle, filled with the precursor, was installed between the gas tubes, see Figure 7. Depending on the vapor pressure of the used precursor several approaches are thinkable.

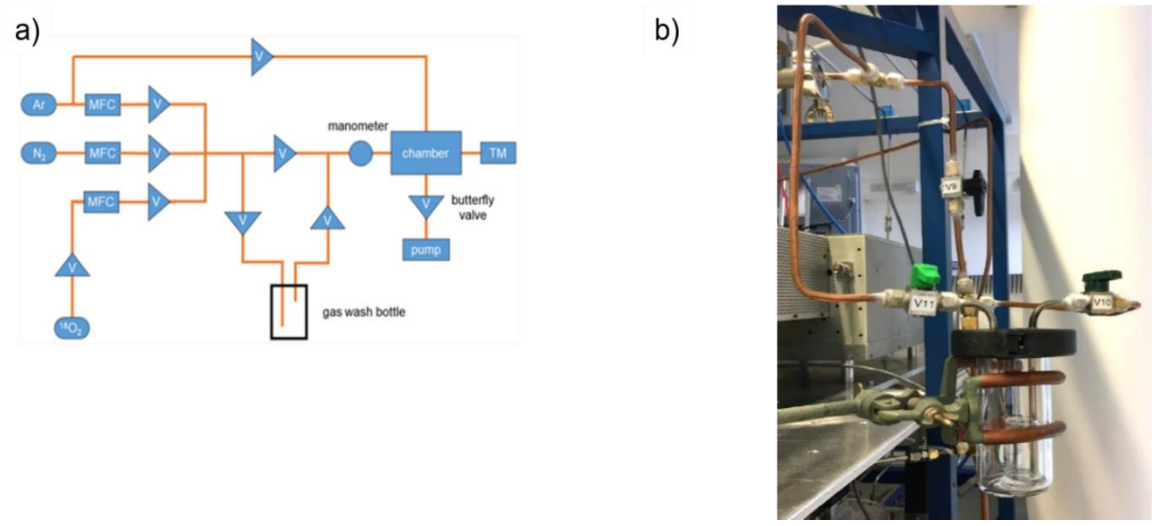

Figure 7: a) Schematic sketch of the gas tubes, mass controllers and valves of the plasma chamber. As working gases Ar, N_2 and $^{18}O_2$ are useable. All gases have to go through a mass controller and can be controlled remotely via PC/labview. b) picture of the gas washing bottle used for the polymer precursor. The washing botte is connected with two hand valves either to the plasma chamber or the other gases. The gas flow of the precursor gas can only be regulated manually via the chamber pressure (manometer).

If the precursor is a liquid and has a low vapor pressure no further adaptations have to be made. Of course, the same is true for gases. For this work we used the pure precursor gas for the plasma but it is also possible to mix it with Ar or even reactive gases like N_2 or O_2. If the vapor pressure of the desired precursor is not high enough, additional heating might be an option. This can either be done with a heat gun, which is also useful for removing water in the tubes and the chamber, or with a fixed heater.

It is also possible to use the plasma chamber and transfer module for other battery components, such as separators or CAMs and apply plasma polymerization/treatment on them.

2.4 XPS, ToF-SIMS and LEIS

In this chapter the analytical methods XPS, ToF-SIMS and LEIS are described in more detail since XPS and ToF-SIMS are the main techniques which were used in this doctoral thesis and LEIS is a rather unused technique but can bring much value for coating and battery analysis.

2.4.1 XPS

The electron spectroscopy for chemical analysis (ESCA) or also called X-ray photoelectron spectroscopy (XPS) is the most commonly used surface characterization technique. The sample surface is irradiated with photons in the X-ray energy range under vacuum. Typical X-ray sources are Al K_α (1486.6 eV) and Mg K_α (1253.6 eV). Due to the X-ray irradiation the surface or more precisely the atoms at the surface emit so called photoelectrons. The photoelectrons emitted in the surface region have enough energy and can leave the sample. They will then travel through the vacuum into the analyzer and are separated by their energy and counted. Electrons from deeper in the sample lose their energy due to inelastic energy loss processes and cannot be detected. As a rule of thumb the detection depths of XPS can be estimated to about 10 nm (3λ) but depends on the mean free path λ of the electrons in the investigated material. The measured kinetic energy (KE) of the electrons is described by Equation 1.[88]

$$KE = h\nu - BE - \Phi_s \qquad \textbf{Equation 1}$$

$h\nu$: Photon energy of X-ray source

BE: Binding energy of the electron emitted from the atom orbital

Φ_s: Work function of the spectrometer

Since the kinetic energy is measured and the photon energy and work function are known, the binding energy of the electrons can be calculated and is typically depicted in XPS measurements. Because every element has a different unique set of binding energies, it is possible with XPS to identify the elements in the probed region of the sample. Additionally, a quantification of the probed sample volume within an error range of about < ± 10 % is possible since the detected photo electrons of an element are proportional to its

concentration. Another feature of XPS measurements is the determination of oxidation states of the elements in the sample. As the binding energy of an electron is influenced by the chemical state of the element, because the electron density is changed, the measured kinetic energy varies for different oxidation states of the same element and can be identified. With XPS all elements except of H and He can be measured with a detection limit of about 0.1 at% and quantified. It is also possible to combine the XPS measurement with sputter steps with for example an Ar gun, a GCIB or C60 gun to apply depth profiling on the sample. This approach allows to get sub-surface information such as a qualitative and quantitative depth distribution of elements or changing oxidation states within the sample.

2.4.2 ToF-SIMS

ToF-SIMS is the combination of a time of flight analyzer with a secondary ion mass spectrometer to analyze ionized particles of a surface. Primary ions (e.g. Bi^+) are accelerated under vacuum on the sample surface and secondary particles are emitted due to the ongoing collision cascade from the uppermost layer. During the emission of the secondary particles, fragmentation and reactions as well as ionization processes will take place. Since the fragmentation and reactions can lead to species that are not naturally present in the sample ToF-SIMS is not able to detect chemical components without reference measurements. The charged secondary ions will be detected by a time-of-flight (ToF) analyzer. Therefore, all secondary ions are accelerated to a given potential and lead on a defined pathway to the detector. The flight time is measured and the *m*/*z* ratio can be calculated via Equation 2.[88]

$$t = L\left(\frac{m}{2zV}\right)^{\frac{1}{2}} \qquad \textbf{Equation 2}$$

t: Flight time

m/z: Mass-to-charge ratio of the secondary ions

L: Length of flight path

V: Acceleration potential

In comparison to XPS the signal intensity in ToF-SIMS analysis is not necessarily an indication of the concentration in the sample because the intensity depends on more parameters than the concentration and the ionization probability can change in different matrixes for the same fragment dramatically. The whole correlation is given in Equation 3.

$$I_s^{\mathrm{m}} = I_p \cdot y_{\mathrm{m}} \cdot \alpha^{\pm} \cdot \theta_m \cdot \eta \qquad \textbf{Equation 3}$$

I_s^m: Secondary ion current of species m

I_p: Primary ion current

y_m: Sputter yield

$\alpha^{\pm}$: Ionization probability for anions or cations

θ_m: Fractional concentration of m in the probed area

η: Transmission of used SIMS instrument

A quantification is only possible with reference measurements in defined systems. The detection limit of ToF-SIMS is in the ppm to ppb range and the depth resolution when depth profiling in combination with a sputter gun is in the 1 nm range. Therefore, a combination of ToF-SIMS and XPS measurements is very complementary since the combination of both results can help to fully understand the chemical environment and 3D morphology of thin layers.

2.4.3 LEIS

With Low energy ion scattering (LEIS) or ion scattering spectroscopy (ISS) information from the topmost atomic layer is obtained and is therefore the most surface sensitive technique. Primary noble gas ions such as He^+, Ne^+ and Ar^+ are accelerated on the surface with energies between 0.5−5 keV and the energies of the backscattered ions are measured e.g. with an electrostatic field or with a ToF analyzer. The interaction process is a two-body elastic collision problem. Since energy and momentum conversion have to be fulfilled the masses of the surface atoms can be calculated. For a 90° scattering process Equation 4 is valid. With LEIS only the individual atoms can be detected but no chemical or compositional information can be obtained.

$$\frac{E_1}{E_0} = \frac{M_2 - M_1}{M_2 + M_1} \qquad \textbf{Equation 4}$$

E_1: Energy of backscattered primary ion

E_0: Initial Energy of primary ion

M_1: Primary ion mass

M_2: Surface atom mass

The surface sensitivity of LEIS is also its biggest problem, since the sample surface has to be very clean and the system under UHV to avoid contamination. In comparison to ToF-

SIMS LEIS has no matrix effect which enables quantification of the surface atoms. With LEIS theoretically all elements heavier than H can be detected and the detection limit increases from Li of >1% over F of 1% over K of 0.05% and everything heavier than U of 0.001%.

Since the surfaces of protective coatings for CAMs or LMAs are in contact with the liquid or solid electrolytes and determine the properties, a greater understanding of the exact element distribution could bring great value to better understand the protective effect of coatings.

3. Results

At the start of this doctoral thesis in 2019 the fabrication of passivation layers for CAMs or LMAs were already present in the literature. However, the analyses of CAM protection layers was not comprehensive, since a large number of different materials were applied on CAMs but most often only the electrochemical performances were examined without deeper knowledge of the morphology and composition of the passivation layer. Mainly TEM, XRD or XPS were used to identify the coatings. For LMAs coating approaches such as ALD or plasma polymerization were used already in the 1990s to apply protective coatings for a possible usage of an LMA. Since the reactivity and formation of a native passivation layer of lithium metal was not very clear for battery research, this topic was first examined in the second publication to look afterward at possible ASEIs under controlled conditions with known substrates in the third publication. Additionally, the evaluation of Li 1s XPS data in literature was often inconclusive due to different analysis challenges which were discovered during the different works of this thesis. Therefore, the objectives of this work were to find reliable analytical methods to better understand coatings on CAMs and LMAs and give guidelines to avoid misinterpretation. Since the usage of LMAs is still of great interest but not implemented yet also the fabrication of a new ASEI was part of this thesis.

In the first publication of this doctoral thesis, guidelines for a comprehensive analysis of CAM coatings by the example of the known coating TiO_2 on NCM622 are presented. Besides the established methods also Raman spectroscopy, ToF-SIMS and LEIS were used to gain fast and easily accessible results for Raman spectroscopy, imaging with ToF-SIMS and surface information with LEIS. It was also looked at the difficulties and limitations of the used methods. In the second publication a comprehensive analysis of the native passivation layer with XPS and ToF-SIMS of different lithium samples was carried out and guidelines, as well as typical pitfalls were highlighted. In the third publication the electro chemical performance of symmetric Li cells was examined after applying plasma polymer layers on LMAs. The layers were characterized by ToF-SIMS and XPS and the mechanical properties were examined by nanoindentation. Additionally, the removal of the native passivation layer by Ar plasma treatment was examined.

3.1 Publication 1: “Analyzing Nanometer-Thin Cathode Particle Coatings for Lithium-Ion Batteries – The Example of TiO_2 on NCM622”

In publication 1 of this doctoral thesis, NCM622 particles were coated with TiO_2 by ALD as a model system and the coating layer was characterized by SEM/EDX, TEM/STEM, XPS, Raman spectroscopy, XPS, ToF-SIMS and LEIS. Advantages and disadvantages of the different methods were discussed and guidelines for a comprehensive analysis were given.

Unlike previous publications on CAM coatings, different analytical approaches are presented and discussed. The results showed that ALD is a suitable technique to apply conformal coatings on CAMs. SEM/EDX are good methods to get a first look after the coating process and see if the deposition was successful. During analysis the electron beam can initiate electrochemical reactions, which change the sample. The layer thickness and crystallinity can be determined by TEM using a grinding approach but also gives a large number of uncoated primary particles, which complicates the analysis. With XPS the oxidation state of the coating and partially the covering, depending on the coating layer thickness, can be examined. ToF-SIMS, Raman spectroscopy and LEIS have proven to be useful additions to the analysis of protective layers on CAM particles, since ToF-SIMS enables the imaging of the coating around the particles, Raman-spectroscopy provides rather easily accessible results and LEIS provides information about the surface and covering of the coating.

All in all, the results of the first publication highlight the advantages and disadvantages of different analytical methods for the analysis of CAM coatings and provide a guideline for the analysis, which can help to understand the properties of CAM coatings in full detail and for development of coatings for next generation batteries.

The experiments of this work were designed and planned by the first author under the supervision of M. Rohnke and J. Janek. The first author performed the ToF-SIMS, XPS, REM and LEIS measurements. F. Walther helped with the ToF-SIMS experiments. J. Sann and F. Walther helped with the XPS data evaluation. B. Mogwitz performed the FIB-REM measurements. The STEM measurements were performed by S. Ahmed. S. Burkhardt and L. Chen performed and evaluated the Raman measurements under supervision of P.J. Klar. The LEIS measurements were performed together with S. Fearn at the Imperial College London. The manuscript was written by the first author and edited by all co-authors.

ACS APPLIED ENERGY MATERIALS

www.acsaem.org Article

Analyzing Nanometer-Thin Cathode Particle Coatings for Lithium-Ion Batteries—The Example of TiO_2 on NCM622

Yannik Moryson, Felix Walther, Joachim Sann, Boris Mogwitz, Shamail Ahmed, Simon Burkhardt, Limei Chen, Peter J. Klar, Kerstin Volz, Sarah Fearn, Marcus Rohnke,* and Jürgen Janek*

Cite This: *ACS Appl. Energy Mater.* 2021, 4, 7168−7181 Read Online

ACCESS | Metrics & More | Article Recommendations | Supporting Information

ABSTRACT: Cathode active materials (CAMs) in state-of-the-art lithium-ion batteries are mostly lithium-transition-metal oxides such as $Li(Ni_xCo_yMn_z)O_2$ ($x + y + z = 1$). To achieve optimum cycling stability and performance of the cathode, the extent of degradation processes and side reactions between CAMs and liquid or solid electrolytes has to be minimized. For this purpose, various coating strategies for CAMs have been developed in recent years. The underlying mechanism of the protective function of nanoscale coatings and their role for the enhanced cycling performance are mostly unclear, which is often based on incomplete characterization of the coating. Only a few analytical methods, such as X-ray diffraction, scanning electron microscopy/energy-dispersive X-ray analysis, or X-ray photoelectron spectroscopy, have frequently been used in recent years, which often cannot provide enough information for a reliable and consistent picture of the very thin coating. For this reason, we demonstrate a systematic study on the analytical characterization of coated CAM using additional analytical methods. NCM622 coated with TiO_2 by atomic layer deposition is used as a model system and analyzed with SEM/EDX, focused ion beam scanning electron microscopy, scanning transmission electron microscopy, Raman spectroscopy, X-ray photoelectron spectroscopy, low-energy ion scattering, and time-of-flight secondary ion mass spectrometry. The results highlight the advantages and disadvantages of each analytical method for the analysis of typical CAM coatings. The results demonstrate that a combination of the different methods is essential to understand CAM coatings and their properties in full detail.

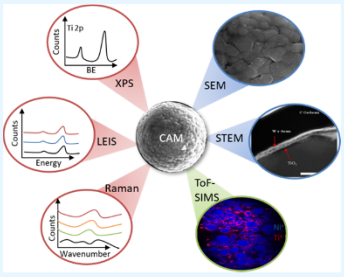

KEYWORDS: *lithium-ion battery, Ni-rich NCM, cathode active material, cathode coating, low-energy ion scattering, time-of-flight secondary ion mass spectrometry*

INTRODUCTION

Lithium-transition-metal oxides such as lithium cobalt oxide ($LiCoO_2$, LCO), lithium manganese oxide ($LiMnO_2$, LMO), lithium nickel manganese cobalt oxide ($Li(Ni_xCo_yMn_z)O_2$, NCM, $x + y + z = 1$), or nickel cobalt aluminum oxide ($(Li_{1+x}(Ni_{1-y-z}Co_yAl_z)_{1-x}O_2$, NCA) are mainly used as cathode active materials (CAMs) in state-of-the-art lithium-ion batteries (LIBs).[1,2] Further optimization of the cycling stability and performance of LIBs at the cathode side can be achieved by reducing degradation processes related to CAMs such as structural changes or interfacial reactions, which occur during battery cycling, for example, due to the electrochemical instability of the liquid and solid electrolytes.[3−7] The particular shape of the used CAM particles enables large contact areas between the CAMs and the electrolyte, which is necessary for a high capacity but also implies a high fraction of interfacial degradation. These interface reactions lead to the formation of side products, unwanted passivation layers, and ultimately capacity loss and a decrease in battery performance. For suppression of such degradation mechanisms, CAMs can be doped with other elements, covered with nanoparticles (locally restricted additives), or coated with thin protective layers by different deposition methods.[8−16]

To achieve a superior cycling performance in terms of long-term stability of CAMs, a protective surface treatment (surface doping and/or additional coating) seems promising,[17−19] but the underlying physicochemical function of the various coatings remains mostly unclear. One main reason is the difficult quantitative analysis of coatings. Accordingly, analytical methods for coating characterization must cope with the spherical shape of particulate CAMs with dimensions on the microscale, the nanometer-thin coatings and the resulting low volume and mass fraction of the coating material itself. In addition, the requirements on the sample preparation and sample transfer are high. Most Ni-rich NCM-based CAMs are sensitive to atmosphere and react with both H_2O and

Received: May 3, 2021
Accepted: June 23, 2021
Published: July 13, 2021

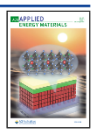

https://doi.org/10.1021/acsaem.1c01255
ACS Appl. Energy Mater. 2021, 4, 7168−7181

CO_2.[6,20] Not only the sample transfer into the analysis chambers is critical because the sample can degrade due to contaminations and atmospheric residues in the transfer vessel, but also, during the analysis itself, the sample surface can change due to evaporation of volatile substances, adsorption/redeposition of chamber contaminations or effects related to beam-damage, to name a few. Overall, these considerations lead to high requirements on the analytical methods used. From an analytical point of view, it is challenging to find the best compromise between spatial resolution, chemical information, and detection limit of the different methods (see Figure 1). As one method cannot deliver all necessary information, a combination of different analytical methods appears essential to obtain a complete picture of the coating properties.

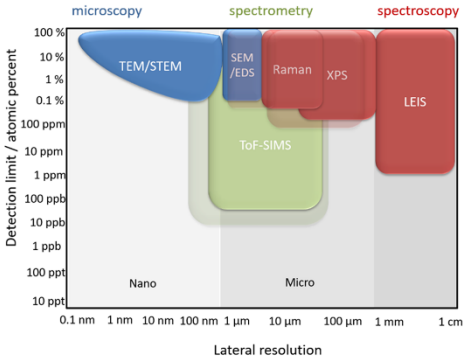

Figure 1. Detection limit vs lateral resolution of the used techniques in this work. The limits for lateral resolution and detection limit are not sharp and depend on the examined sample. The colored areas represent common measurement routines and transparent areas indicate the limits that can be obtained with ideal samples.

In the literature, coatings are mostly characterized by their influence on the cell cycling performance and precharacterized using scanning electron microscopy (SEM), transmission electron microscopy (TEM), energy-dispersive X-ray spectroscopy (EDX), X-ray diffraction (XRD), sometimes X-ray photoelectron spectroscopy (XPS), and rarely Raman spectroscopy.[21−30] The information gathered about the coating is mostly restricted to rough conclusions about the coating material distribution on the CAM surface and basic statements on its chemical composition. Other important information such as the degree of coverage of primary and secondary particles, possible interface reactions between the coating material and the CAM, changes in the composition due to variations in the coating thickness, or diffusion processes remain unknown in most cases. Knowledge of such properties could be quite valuable for understanding the functionality of coatings themselves, as well as the mechanism of improved battery performance, and is only accessible through a combination of different analytical methods.

Besides the routine-type methods mentioned above, additional surface-sensitive methods can provide highly useful information that cannot be obtained by the aforementioned methods. One of such powerful surface-sensitive methods is time-of-flight secondary ion mass spectrometry (ToF-SIMS). With its high chemical specificity, high lateral resolution (ca. 50−100 nm), and low detection limit (ppm-ppb), it is often complementary to XPS. Walther et al., for example, combined ToF-SIMS and XPS to investigate the interfacial degradation of a composite cathode of an In/InLiILi_6PS_5Cl|Li-$Ni_{0.6}Co_{0.2}Mn_{0.2}O_2$/$Li_6PS_5Cl$ all-solid-state battery cell (ASSB). The authors visualized the formation of the degradation layer (CEI) between the CAM and the solid electrolyte and obtained information on the reaction products.[31] The actually most surface-sensitive method is low-energy ion scattering (LEIS), where noble gas primary ions are accelerated onto a sample and the energy of the backscattered ions after collision with the surface atoms is measured.[32,33] Exclusively, the first atomic surface layer is probed. Téllez et al. used a combination of LEIS and ToF-SIMS to analyze the surface composition of solid electrolyte materials such as lithium lanthanum titanate perovskite (LLTO).[34] Using a pulsed primary ion beam to suppress secondary ion signals, they could also detect Li by LEIS, which is very challenging due to low-sensitivity factors of light elements. Hoskins et al. used LEIS and ToF-SIMS to investigate the ALD growth of very thin Al_2O_3 layers on NCM111.[35] These examples show that less common surface-sensitive analytical methods provide unique information that cannot be easily accessed by other methods. By combining these methods with more established ones, a more complete and comprehensive understanding of coatings is possible.

In Figure 1, the detection limits for different analytical methods are plotted vs the lateral resolution. Methods such as TEM with a high lateral resolution typically suffer from a poor detection limit and often cannot provide detailed information on the chemical environment. In contrast, methods such as ToF-SIMS can provide the latter information with good detection limits but suffer from a ≥100 times poorer lateral resolution compared to TEM. Even with this simplified comparison, it is obvious that the combination of different methods is required to comprehensively characterize nanometer-thin CAM coatings.

To highlight the advantages and disadvantages and also critically discuss the limits of each technique, we select a TiO_2 model CAM coating deposited by atomic layer deposition (ALD) on $Li(Ni_{0.6}Co_{0.2}Mn_{0.2})O_2$ (NCM622) secondary particles. TiO_2 was chosen since it is a well-known material for ALD processes and can be easily deposited with high conformity and reproducibility. In addition, it has already been used as a protective coating on NCM and has been shown to improve the cycling performance.[25] We apply a variety of more routine-type analytical methods such as SEM, STEM, TEM, and EDX to analyze the morphology of the coating; XPS and Raman spectroscopy to get chemical information; ToF-SIMS for visualization of the coating; and LEIS for information on the uppermost layer, its composition, and the coating coverage on NCM. In combination, the different methods provide comprehensive information on the coverage, the morphology, and the composition of the coating.

■ RESULTS AND DISCUSSION

Visualization of the TiO_2 Coating by SEM/EDX/FIB-SEM. The morphology of the NCM622 particles and possible changes due to the deposition of the TiO_2 were investigated by SEM analysis. A comparison between uncoated and coated particles is shown in Figure 2a−d. The morphology of the

https://doi.org/10.1021/acsaem.1c01255
ACS Appl. Energy Mater. 2021, 4, 7168−7181

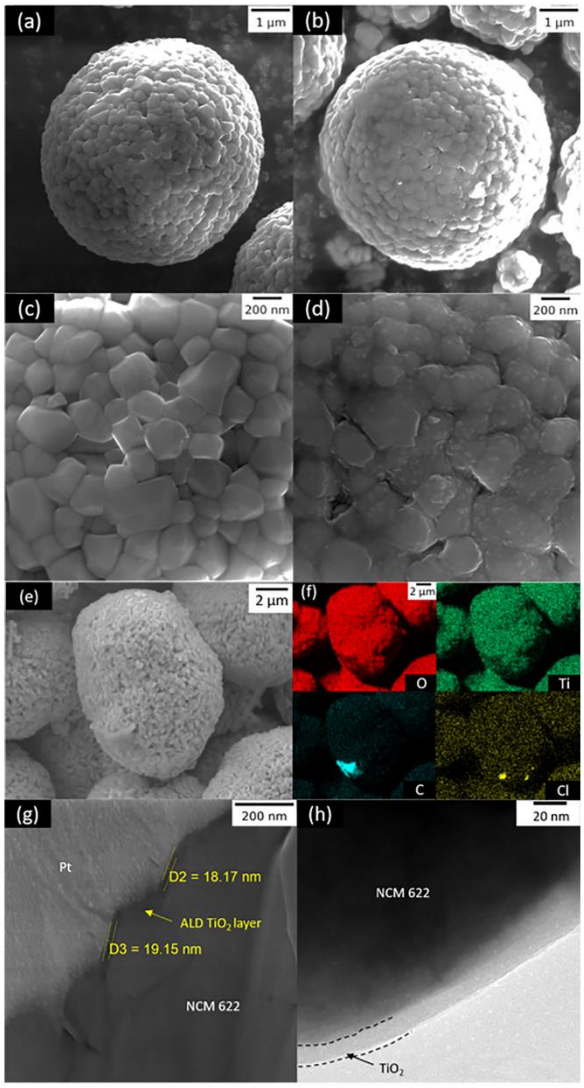

Figure 2. (a, c) SEM secondary electron (SE) images of uncoated NCM622 particles. (b, d) SEM SE images of TiO_2 (400 ALD cycles)-coated NCM622 particles. (e) SEM image of TiO_2 (400 ALD cycles)-coated NCM622 particles and (f) the corresponding EDX mappings of Ti, O, C, and Cl. (g) SEM SE image of a cross section of coated NCM622 particles. The coating thickness is about 18−19 nm. (h) TEM image of a coated NCM622 primary particle. The coating thickness is in the same range as in (g).

CAMs before and after coating looks very similar, with the surface appearing rougher and more structured after the coating process. The EDX mappings of the coated particles, also shown in Figure 2e, f indicate that Ti is homogeneously distributed on the surface of the particles, which proves successful deposition. Additionally, some Cl contamination was detected, probably originating from ALD precursor residues, namely, $TiCl_4$-related compounds. In the images of the FIB cross section in Figure 2g, a thin dark layer of about 20 nm thickness is visible between the CAM particle and the platinum protection layer. Given the STEM/EDX results below and the coating thickness being in the typical range for

https://doi.org/10.1021/acsaem.1c01255
ACS Appl. Energy Mater. 2021, 4, 7168−7181

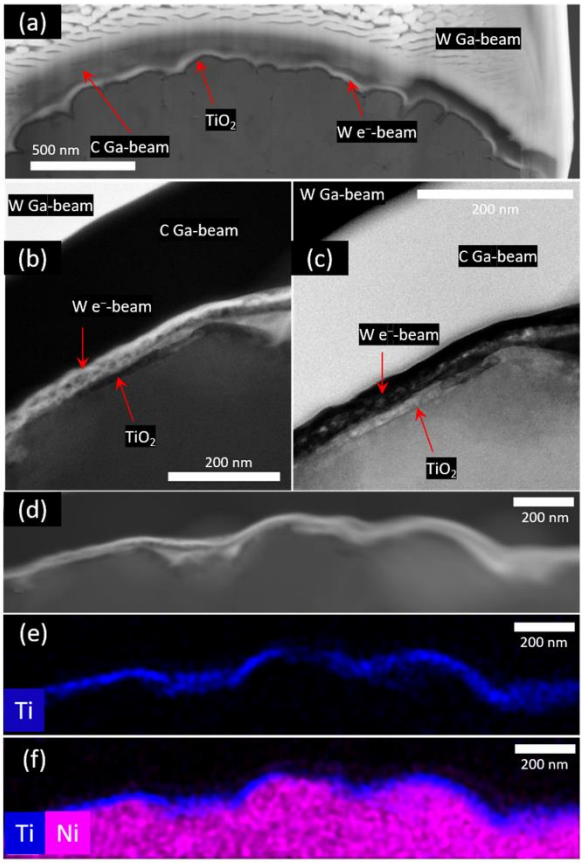

Figure 3. (a) SEM SE image of a secondary particle cross section acquired during sample preparation by FIB. "W e⁻-beam", "C Ga-beam", and "W Ga-beam" represent the tungsten (W) and carbon (C) protection layers deposited using electron (e^-) beam and Ga-ion beams, respectively. The TiO_2 layer has a thickness of approximately 22 nm. (b, c) STEM high-angular annular dark-field (HAADF) and bright-field (BF) images, respectively, showing TiO_2 coating. (d–f) EDX mappings of Ti and Ni and the STEM image of the coated particle.

the ALD process (growth rate 0.057 nm/cycle on a planar substrate), it is reasonable to identify the dark layer as the coating. For EDX analysis, the beam energy must be chosen in a way that the Kα X-ray line of Ti (4.5 eV) is excited. This results in a spatial resolution that is no longer sufficient to detect the coating layer with EDX, since the electron penetration depth becomes much larger than the layer thickness. For higher surface sensitivities, low excitation energies are mandatory. Unfortunately, the energy resolution of the used EDX detector was not high enough to distinguish the Ti Lα line at 0.45 eV from the Kα line of oxygen. This may be different for other coating materials, where the lines are distinguishable. Nevertheless, we find a homogeneous Ti distribution on the surface of the secondary particles (see Supporting Information S1). We like to note here that one should be cautious when using a backscattered electron detector (BSE) and observing a high brightness contrast. Accordingly, the brighter area in Figure S2 represents redeposited material due to the FIB preparation, but not the coating. This can easily lead to misleading interpretations of SEM micrographs.

SEM/EDX is a reasonable tool to control whether deposition took place at all. Except for Li (needs a special detector) and H, all other elements can be easily detected by standard EDX, which means the majority of coatings can be judged by SEM and EDX. One should keep in mind that electrochemical reactions and other degradation processes can be initiated by the electron beam while examining the CAMs, and therefore the material may change upon measuring.[36]

TEM/STEM techniques allow visualization of coatings with a high spatial resolution. While TEM facilitates higher magnification and spatial resolution compared to SEM, it may not be straightforward to identify a coating layer on CAM particles because of damage from sample preparation. Two

https://doi.org/10.1021/acsaem.1c01255
ACS Appl. Energy Mater. 2021, 4, 7168–7181

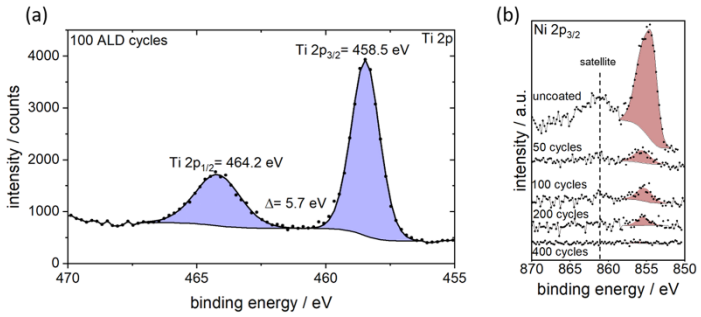

Figure 4. (a) XPS Ti 2p detail spectra of the coated NCM622 particles (100 ALD cycles). Note that the full width at half-maximum (FWHM) for the Ti $2p_{1/2}$ signal is broader than the Ti $2p_{3/2}$ due to the Coster−Kronig effect. (b) XPS detail spectra of Ni $2p_{3/2}$ as a function of the ALD cycle number (without differentiation of Ni^{3+} and Ni^{2+}).

different strategies for the sample preparation are discussed in the following.

The first method is to grind the coated secondary particles and disperse the solution containing the primary particles onto a TEM grid. This method of TEM sample preparation leads to the destruction of the secondary particle structure of the CAMs, which allows the examination of primary particles, as seen in Figure 2h. This also leads to a random distribution of at least two types of primary particles. Accordingly, several particles originate from the inside of the secondary particles, whereas significantly fewer primary particles were located on the surface of the secondary particles. Only the outer surface of the latter has been coated (see Figure S3). Since the fraction of surface-coated particles is small in comparison to all particles in a secondary particle, finding these particles is a tedious and time-consuming process. Moreover, only a small fraction of the surface of such surface particles is coated, which makes the analysis statistically even more challenging (see Figure S3). Additionally, the amorphous nature of the coating makes it difficult to identify the coated surfaces in a mixture of primary particles due to low contrast differences. Another drawback of this preparation method is that grinding of the secondary particles and the subsequent treatment to disperse them onto a TEM grid might affect the coating adversely. However, if coated primary particles can be found, then the layer thickness can be easily determined by TEM as seen in Figure 2h. Therefore, this preparation method is a relatively easy approach to determine basic coating properties such as the coating layer thickness.

The second method comprises a sample preparation using a FIB. This method has some advantages and also disadvantages. Here, finding the coated surfaces is not a problem. Moreover, changes of the coating layer during FIB preparation can be monitored between the various thinning steps, as shown in Figure 3a (if the coating layer is thicker than the lateral resolution limit of the SEM). A major advantage of FIB/SEM preparation over the grinding approach is that the coating remains undamaged, since the deposited protective metal layers protect the coating quite well. However, these protective layers also cause a major disadvantage in comparison to the grinding approach, since they can lead to projection artifacts in the subsequent TEM/STEM analysis. On the one hand, the projection effects can originate from the protection layers and, on the other hand, from the primary particles' surface at which the coating is present as shown in Figure 3b,c. This disadvantage can be compensated to a certain extent using STEM-EDX. Figure 3d−f shows the distribution of titanium on the surface of a secondary particle. It was found that the coating layer can sometimes be better visualized using SEM if it is sufficiently thick, especially during the thinning process by FIB, as shown in Figure S4. This is mainly because of higher surface sensitivity of the SE detector. Hence, we conclude that the combination of the highly surface-sensitive secondary electron signal from the SEM/FIB during sample preparation and the significantly higher resolution of EDX (and electron energy loss spectroscopy (EELS)) maps in STEM offers good visualization of the coating layers on the secondary particles. Also, EELS can provide information on the oxidation states of the elements in the coating,[37] complementing XPS analysis.

The FIB preparation route will be particularly important when analyzing electrochemically cycled or annealed coated CAMs. Unlike grinding,[38] FIB preparation preserves the spatial position of the sensitive and fragile surface films (formed after electrochemical cycling) due to protection layers, thus allowing an analysis of the morphology and composition of the interfacial region. Furthermore, the thinning process can be performed with great control, enabling subsequent high-resolution TEM/STEM analysis. All in all, it is recommended to also coat electrochemically cycled samples with, e.g., Au or Pt by electron deposition before conducting FIB preparation. In this way, the sample surface is protected during FIB preparation and the uppermost surface region can also be analyzed, which would otherwise be destroyed by the high-energy FIB. Another advantage is that the deposition of Pt leads to a smooth surface and thus reduces the curtaining effect.

As already mentioned, the low contrast between the coating and the CAM in BSE images can be problematic. If the masses of the coating material and CAM are too similar, the contrast within BSE images is poor. The differences in brightness in Figure 3b,c is just enough to differentiate between TiO_2 and the NCM. This might be different for other coating materials, but together with the EDX analysis shown in Figure 3e,f, clear identification is also possible for other materials.

Chemical Information by XPS. After visualization and determination of the layer thickness, the focus is now on the chemical composition. With XPS, the chemical composition and the bonding state of the coating components can be

https://doi.org/10.1021/acsaem.1c01255
ACS Appl. Energy Mater. 2021, 4, 7168−7181

determined and some information about the coverage may be obtained. XPS is a commonly used technique to analyze battery materials.[39−41] Depending on the electron mean free path in the examined compounds, XPS measurements provide chemical information within a depth in the range of roughly 10 nm. This can be problematic when analyzing very thin coatings, since the photoelectrons analyzed will originate from the coating and the substrate material (convoluted information). It is also possible to sputter in between XPS measurements to create depth profiles to analyze the interface between the coating and the CAM. However, sputtering can lead to a deterioration of the materials (e.g., due to differential sputtering) and thus to changes in the energetic signal position of the various elements. In addition, due to the spherical geometry of the particles, a complete removal of the coating is not possible because of shading effects.

However, several conclusions can be drawn from XPS surface measurements: Besides Ni, Co, Mn, O, and Li from the CAM substrate, and Ti and O from the coating, C and Cl were detected as impurities (see Figure S5). The atomic fraction of Cl decreases with increasing ALD cycles (from 12 to 2%), indicating a reaction between HCl, which is formed as a side product during the ALD process, and the NCM powder. This ultimately leads to the formation of transition-metal chlorides. After a certain number of ALD cycles, the entire surface of the NCM secondary particles (partially containing transition-metal chlorides) is covered with TiO_2 and HCl can no longer react with the NCM. Since XPS is a surface-sensitive technique, the reacted interface toward the NCM is successively covered by TiO_2 and thus signals related to transition-metal chlorides are decreasing with increasing TiO_2 layer thickness. The Ti 2p detail spectrum of coated CAM (100 ALD cycles) in Figure 4a reveals the formation of TiO_2 as the Ti $2p_{3/2}$ signal is located at a binding energy (BE) of 458.5 eV and the spin−orbit split between Ti $2p_{3/2}$ and Ti $2p_{1/2}$ is Δ = 5.7 eV.[42] The O 1s detail spectrum (not shown here) confirms the formation of TiO_2 and additionally indicates some surface contaminations (e.g., due to adsorbates). Furthermore, the atomic ratio of n(Ti)/n(O) is nearly 1:2 (oxide), which further strengthens the evidence for TiO_2. If the TiO_2 layers were dense and thicker than roughly 6−8 nm, no substrate signal should be visible based on the calculation of an electron inelastic mean free path of about 2.1 nm.[43] Therefore, Ni 2p detail spectra were measured and monitored as a function of ALD cycle numbers. The spectra shown in Figure 4b reveal that for ALD cycle numbers of less than 400, a weak Ni $2p_{3/2}$ signal is detected that increases with decreasing ALD cycle number and simultaneously shifts to lower binding energies. This could indicate a higher Ni^{3+} fraction for the coated particles but seems more likely due to potential gradients and thus energy calibration-related issues (see discussion below). With XPS alone, it is not clear whether the coating layer is too thin at lower ALD cycle numbers or whether a particulate coating is the reason that nickel signals can be observed. In this context, the results derived from TEM/STEM analysis are helpful, showing that 400 ALD cycles lead to a coating thickness of about 17−22 nm. This agrees reasonably well with a growth rate of 0.057 nm/cycle derived from a planar reference. Assuming a conformal growth process and a constant growth rate of 0.057 nm/cycle, the ALD process should theoretically lead to layer thicknesses of 2.85 nm (for 50 ALD cycles), 5.7 nm (for 100 ALD cycles), 11.4 nm (for 200 ALD cycles), and 22.8 nm (for 400 ALD cycles), respectively. Since substrate signals are weak for the sample coated with 200 ALD cycles and vanish for higher cycle numbers (see Figure 4b), a relatively conformal layer growth and a relatively dense coating layer can be assumed.

Sample preparation and measurement procedure for the NCM particles are straightforward, making XPS a fast and relatively simple analytical tool to examine CAM coatings. In contrast, it should be noted that the evaluation itself is often not straightforward and requires knowledge and expertise from the operator to avoid misinterpretation. Especially energy calibration is crucial for battery materials and can easily lead to misinterpretations if not done correctly. Coated CAMs, for example, mostly correspond to an alkali-metal-containing, electronically conductive material covered by an insulating layer. For this reason, differential charging effects and potential gradients must be taken into account, which can lead to relative shifts in the energetic signal position of the different components and will thus influence the energy calibration procedure.[44−46] The commonly applied calibration in relation to the signal of adventitious carbon can therefore easily be misleading. Accordingly, it is not sufficient to calibrate all spectra to the C−C signal contribution at 284.8 eV if it is not clear to which material component/layer this signal belongs to. The suitability of the energy calibration procedure should therefore be verified with other signals of the same compound to exclude the aforementioned detrimental effects.

Raman Spectroscopy. Among the presented methods for material characterization, Raman spectroscopy can be considered a particularly fast and nondestructive approach for the vibrational characterization and identification of materials. Raman spectroscopy can easily be applied to battery materials[47,48] in general, and also to coated CAM particles. However, it turns out that Raman spectroscopic analysis of materials relevant for high-performance LIBs and SSBs is only in few cases successful. Uncoated CAM particles with a size in the range of several micrometers often consist of multiple crystalline primary particles with grain boundaries and pores between them. The diameter of a laser spot on the sample in conventional Raman experiments is at best given by the diffraction limit of half the excitation wavelength. However, considering that it usually is in the order of 1−5 μm in diameter, Raman spectra measured on CAM particles will always reflect averaged vibrational properties of several primary particles, their surfaces, and grain boundaries. In addition, state-of-the-art CAMs are usually (transition)-metal-oxide solid solutions containing several different (transition) metals leading to rather broad Raman features, which may significantly depend on the actual composition of the alloy. The vibrational characteristics of different positive and negative electrode materials, experimental requirements, and the interpretation of the Raman spectra obtained can be found in a review by Julien and Mauger as well as references therein.[48] A recent trend in research on CAMs is to employ single-crystalline CAM particles in composite cathodes.[49,50] Employing single-crystalline primary particles will increase the potential of Raman spectroscopy for the characterization of CAMs significantly.

Going from uncoated CAM particles to coated ones, vibrations originating from the coating material arise at the expense of those originating from the surface of the CAM particles. The capability of Raman spectroscopy for coating characterization, in general, strongly depends on the composition and structure of both the CAM and the coating.

https://doi.org/10.1021/acsaem.1c01255
ACS Appl. Energy Mater. 2021, 4, 7168−7181

Both components determine the position of the individual modes and the corresponding scattering cross section. If Raman modes originating from the coating material can be distinguished from those originating from the CAM, the method provides a powerful tool for structurally characterizing the coating material with little sample preparation prior to the experiment unlike, e.g., in the case of TEM. However, characterization of amorphous coatings on CAMs by Raman spectroscopy may prove difficult as the corresponding spectra consist of very broad features impeding detection against a background, unless more sophisticated approaches for signal enhancements are followed.[29]

The intensities of individual Raman spectra obtained by mapping over the different powder surfaces have been averaged, and these average Raman spectra are depicted in Figure 5a. The Raman spectra of uncoated and coated

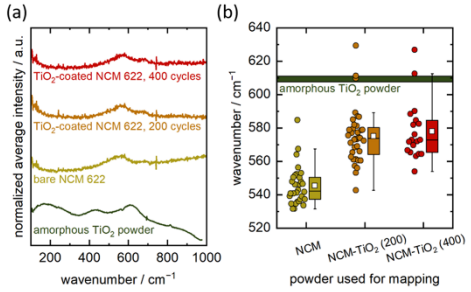

Figure 5. (a) Raman spectra obtained from mapping over four different powder samples. The intensity measured on individual spots was averaged and normalized for comparison. (b) Boxplot depicting the statistical distribution of the central wavenumber between different measurement spots on the powder surface. The white boxes represent the average central wavenumber, while the black horizontal lines within the colored boxes represent the median central wavenumber. The green bar represents the range in which the central wavenumber of the mode in Raman spectra of the amorphous TiO_2 powder was found.

NCM622 show comparably broad modes between 400 and 700 cm^{-1}. This is in line with Raman spectra of discharged NCM materials published in the literature.[51] A thorough analysis of the lattice dynamics in NCM materials, as well as systematic experimental studies still seem to be missing. Furthermore, challenges like, e.g., mode broadening due to compositional variations among individual primary particles or softening of k selection rules at smaller scales complicate the interpretation of Raman spectra of NCM materials. A qualitative comparison with Raman spectra of NCM622[28,52] and other NCM materials[51,53,54] published in the literature shows a good agreement. For comparison, measured Raman spectra of an amorphous TiO_2 powder are also shown in Figure 5a making use of the knowledge provided by the TEM studies that the TiO_2 coating on the coated NCM particles studied is amorphous. Amorphous TiO_2 reveals comparably broad modes at around 170, 430, and 610 cm^{-1} (see the Supporting Information in ref 55).

There are two qualitative differences between Raman spectra of uncoated and coated NCM622 powders. While the position of the most prominent peak is at approximately 540 cm^{-1} for the uncoated NCM, the Raman spectra of both coated NCM powders show a shift of this peak to higher wavenumbers. Furthermore, the spectra of the uncoated NCM sample exhibit a photoluminescence background in contrast to the spectra of the coated NCM samples. This finding suggests that the TiO_2 coating suppresses photoluminescence.

The Raman spectra of the coated and uncoated NCM do not show distinct features due to the coating in this case. Furthermore, conclusions regarding the characterization of the coating are difficult to deduce from a qualitative comparison of single spectra only. Note that the spectra shown in Figure 5a are average intensity values from multiple measurement spots on the powder surface. Also, the aforementioned shift of the most pronounced mode toward higher wavenumbers observed in Raman spectra of coated NCM622 particles is barely visible to the unaided eye. To analyze the experimental data in this respect more quantitatively, this mode was fitted with a Gaussian in all of the Raman spectra obtained from different positions on the powders after the background was subtracted. A boxplot depicting the statistical distribution of the central wavenumber of the dominant NCM mode as well as the wavenumber range, in which the mode at around 610 cm^{-1} was observed in Raman spectra of amorphous TiO_2, is shown in Figure 5b. The scattering of the mode position in Raman spectra of both, the uncoated and coated NCM, demonstrates the expected degree of inhomogeneity of the NCM solid solution. It also highlights the importance of reliable measurement statistics regarding the experimental data as the center position of the mode could easily vary by more than 20 cm^{-1} between different spots on the sample. However, average (white box) and median (solid line within box) mode position are different for spectra of coated and uncoated NCM particles. The corresponding shift is clearly visible in Figure 5b. Thus, an impact of the TiO_2 coating on the surface of the NCM622 particles is observable in the Raman spectra despite the lack of distinct signals of amorphous TiO_2 in the spectra. The lack of distinct TiO_2 features supports the conclusion that the TiO_2 coating is amorphous as crystalline TiO_2 phases yield distinct signals and possess large Raman cross sections.[56]

With the use of reference samples, Raman spectroscopy can not only provide chemical but also structural information regarding the TiO_2 coating. For other coating materials, this might not be the case as a very important requirement is that the examined coating has Raman-active vibrations.

Mass Spectrometric Imaging by ToF-SIMS. ToF-SIMS has been used yet only in a few publications dealing with battery materials and mostly not pushed to its limits. However, some nice results can be found in the literature. For instance, Li et al. imaged the surface and cross sections obtained by Cs^+ sputtering of NCM71515 particles to investigate the interphase between CAM and a nonaqueous electrolyte and the influence of the carbon black additive.[57] Bessette et al. combined FIB-SEM with ToF-SIMS to analyze the cross sections of NCM532 particles and show the Li distribution before and after cycling. Yamagishi et al. investigated and showed the Li distribution in NCA LPS ASSB using the same approach but with operando ToF-SIMS.[58,59]

For coating identification, surface spectra of coated and uncoated NCM particles could be measured and the signal intensities of the coating layer mass fragments can be compared. If the sample surface is covered with contaminations, sputter cleaning must be performed in advance, ideally with an argon cluster gun to enable a gentle cleaning process

https://doi.org/10.1021/acsaem.1c01255
ACS Appl. Energy Mater. 2021, 4, 7168−7181

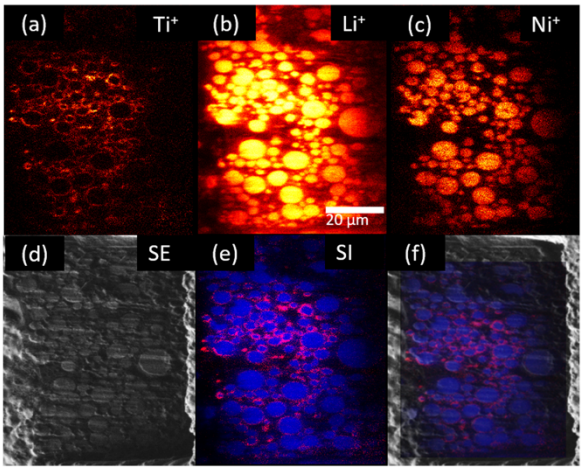

Figure 6. (a) SI image of the summation of $^{46}Ti^+$,$^{47}Ti^+$, and $^{48}Ti^+$ from the cleaned 45° FIB crater wall. (b, c) SI images of $^6Li^+$ and $^7Li^+$ and $^{58}Ni^+$, respectively. (d) Ion-induced SE image of the imaged FIB crater wall. (e) Overlay of the Ni^+ (blue) and Ti^+ signal (red). (f) Overlay of (d) and (e).

and to avoid ablation of the coating layer. The same applies for surface imaging. With both approaches, only the presence of a coating can be proven by corresponding fragments, but no information about the coverage of the entire secondary particle is accessible. The analyzed surface has to be ideally very smooth, otherwise topography effects play a huge role.

Because of its relatively high lateral resolution and sensitivity, ToF-SIMS is a suitable technique to visualize the coating and to gain some chemical information compared to spectroscopic methods.[60,61] In contrast to XPS, the chemical state of the coating cannot be determined by SIMS, but different ions/fragments can indicate components or changes of the chemical environment, for example, after battery cycling.[61] In comparison to other analytical methods, the challenge for ToF-SIMS analysis already starts at the sample preparation level (see Figure S6). Powders are not easy to handle, as the risk of single particles flying into the differentially pumped analyzer has to be avoided. Therefore, different preparation approaches were tested and the most suitable one is presented here. For the most promising approach, the coated CAM particles were embedded in a Technovit 4004 and analyzed with delayed extraction imaging mode. During depth profiling, different sputter rates were observed for the CAM particles and the embedding material (differential sputtering). Therefore, the mixing ratios of the two-component epoxy resin Technovit 4004 were varied to get as close as possible to the CAM particle sputter rates (see Supporting Information S7). Because of the electronically insulating properties of the Technovit matrix, the secondary ion intensity dropped to 0.9% of the intensity of nonembedded particles. As differential sputtering could not be completely avoided, we consider depth profiling of the CAM particles to be not ideal.

For the most suitable mixing ratio, a 45° FIB crater sidewall was prepared and subsequently analyzed in delayed extraction imaging mode. After core milling, the crater sidewall shows a strong curtaining effect, which was reduced by a fine milling approach using the Bi liquid metal ion gun (LMIG) in DC mode.[31] These fine milling steps were also necessary to remove a thin Technovit layer on top of the particles, which probably forms during FIB crater preparation due to melting and/or redeposition of Technovit. The cleaning procedure was performed in several steps, and the crater sidewall was imaged after every step to monitor the cleaning process. Too many cleaning steps damaged the coating and led to a wide distribution of the coating signal. The best results were achieved after a cleaning time of 8 min and are shown in Figure 6. The Ti^+ signal was used to represent the coating (summation of $^{46}Ti^+$, $^{47}Ti^+$, and $^{48}Ti^+$). In the secondary ion (SI) image, Ti^+ circles can be seen very well. Li^+ (summation of $^6Li^+$ and $^7Li^+$) and ^{58}Ni were used to visualize the CAM particles. In the secondary ion overlay image, the Ti^+ signal (red) is clearly visible around the NCM secondary particle edges (Li^+ blue). Overall, ToF-SIMS enables the visualization of the coating around multiple secondary particles together with chemical information, unlike TEM where the coating homogeneity can only be examined on single primary particles.

It must be noted here that the ionization probability for Ti^+ is not particularly high in comparison to, e.g., organophosphate coatings, which can be easily detected and visualized by ToF-SIMS but are not stable, for example, in TEM measurements.[60] The ionization probability in positive- and negative-ion modes as well as potential mass interferences strongly depend on the coating material used. Thus, the experimental settings required for optimum results must be systematically and individually optimized for different coating materials.

LEIS—What Is Really on the Surface? With the knowledge gained up to this point, and considering the uncertainties from the previous analytical methods, LEIS appears to be the perfect method to complement the set of analytical information for characterizing CAM coatings. While Raman spectra, XPS, TEM and SIMS results did not provide a clear evidence of whether the coating is dense and fully covering, LEIS can answer this question. The spectra shown in

https://doi.org/10.1021/acsaem.1c01255
ACS Appl. Energy Mater. 2021, 4, 7168−7181

Figure 7a highlight the surface sensitivity of LEIS. Both the spectra of pristine NCM and coated NCM (after 100 ALD cycles) showed virtually no coating and/or NCM signal, which can be attributed to carbon and hydrogen contaminations on the surface formed by hydrocarbon condensation during sample preparation in air. After a short sputter time, the coating signals become more and more visible and reveal the presence of Cl atoms at the surface, as already indicated by the SEM/EDX measurements. These Cl-based contaminations could have two origins. First, the Cl could originate from the precursor, namely, $TiCl_4$. It is possible that some of the precursor molecules are adsorbed inside the pores of the secondary particle and were not completely removed during the purging step. Second, HCl is formed during the reaction of $TiCl_4$ and H_2O. NCM is highly reactive to HCl and the transition-metal chlorides formed are not volatile and thus are not removed during purging. Unlike ToF-SIMS, LEIS does not show a matrix effect, which allows the comparison of the element-specific counts and quantitative information on the surface composition to be obtained by considering the substrate surface signals (see Figure 7b,c).[32]

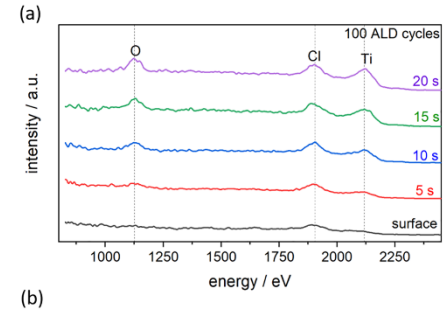

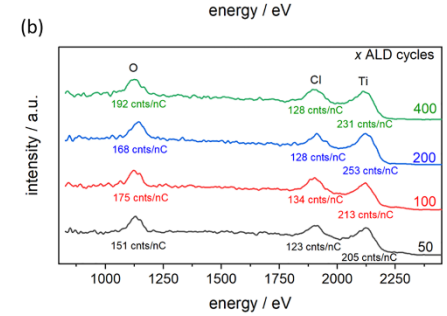

Cycles	O area	Cl area	Ti area	Total area	O /%	Cl / %	Ti / %
50	151	123	205	479	31.52	25.68	42.80
100	175	134	213	522	33.52	25.67	40.80
200	168	128	253	549	30.60	23.32	46.08
400	192	128	231	551	34.85	23.23	41.92

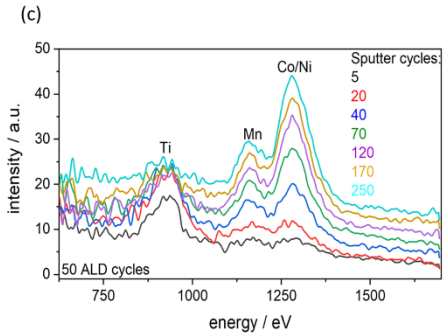

Figure 7. (a) LEIS surface spectra of TiO_2-coated NCM622 particles (100 ALD cycles) after several cleaning steps with the argon sputter gun. (b) Comparison of the cleaned surface signals of all coated NCM622 particles and atomic distribution at the surface for all coated NCM622 particles calculated from the spectra shown in the table. (c) LEIS depth profile of TiO_2-coated NCM622 particles (50 ALD cycles).

Ideally, the number of atomic layers deposited by ALD should not lead to a different surface composition. Assuming similar measurement conditions (e.g., focal plane) and a comparable surface morphology of the samples, all signal areas should be the same. However, surface roughness and/or contaminations can reduce the intensity of surface signals. Additionally, it should be noted that the z-height was adjusted manually for every sample, which can lead to slight differences between the samples and can influence the gain of back-scattered ions. This can explain the differences in intensity for the samples shown in Figure 7. Figure 7c shows LEIS spectra of coated NCM (50 ALD cycles) as a function of several sputter cycles. Initially, no surface signals from the substrate (Mn, Co, Ni) are visible at all, and the only metal detected is Ti. With increasing number of sputter cycles, the Ti surface signal shrinks and Mn, Co, and Ni surface signals develop (40 sputter cycles). Finally, after 250 sputter cycles, almost the entire coating layer is removed and only NCM signals are visible. This clearly shows that already 50 ALD cycles are sufficient to completely cover the entire NCM secondary particle surface with a TiO_2 layer.

From these results, it is clear that LEIS provides unique information about the outer surface at the atomic level that cannot be obtained by other analytical techniques. The extreme surface sensitivity allows us to judge precisely the coverage of the CAM with a coating material, even for very thin coating layers. However, a complete characterization of the coating (i.e., its composition and microstructure) can only be obtained by combining LEIS with other analytical techniques. LEIS measurements alone are only useful when the outermost atoms are to be examined and neither the coating thickness nor the chemical composition are of importance. Since lighter coating elements (m < 16 u) give less intense signals than heavier elements, coating materials with low fractions of light elements on the surface (less than 1%) might be difficult to identify.

The comprehensive analysis of a CAM coating demonstrated in this work is only the first step on the way to improved CAMs. Accordingly, the next step must be a combined study on the influence of coating thickness, composition, and microstructure on the electrochemical performance of CAMs to enable the development of advanced functional CAM coatings. Surely, LEIS can play an important role in this context.

https://doi.org/10.1021/acsaem.1c01255
ACS Appl. Energy Mater. 2021, 4, 7168−7181

CONCLUSIONS

In this work, several analytical methods such as SEM/EDX, STEM/TEM/EDX, FIB-SEM, XPS, Raman spectroscopy, SIMS, and LEIS have been applied to fully characterize the TiO_2 protective coating deposited by ALD on NCM622. We demonstrate that only the combination of several analytical methods offers a comprehensive picture. Therefore, imaging of the coating morphology (SEM, STEM, FIB-SEM) was supplemented by chemical composition/phase composition analysis (XPS, Raman spectroscopy) and imaging mass spectrometry (ToF-SIMS) as combined tool for visualization of morphology and chemical composition. Ultimately, the topmost (atomic) surface layer of the coated NCMs was analyzed by LEIS. Beside the coating elements, small amounts of unwanted precursor residuals and related side products were identified on the CAM surface, which have to be considered in the next step when evaluating the cycling performance. For better comparison, the various analytical methods used are listed in Table 1 together with a brief summary of the information they can provide, assuming state-of-the-art equipment. Considering additionally Figure 1, the analytical limits and specialties of the methods used can be seen. We would like to emphasize here that the success of the measurements with the various methods strongly depends on the examined material system. Accordingly, non-Raman-active coatings, coatings with poor ionization probabilities, coatings with strong charging effects, and/or coatings with high fractions of light elements or elements with similar masses compared to the CAM will pose severe problems depending on the analytical method used. Overall, our results and the experience gained through this work can be summarized in the following statements:

Table 1. Overview of the Used Methods and the Standard Information They Can Provide

method	structure	coating thickness	chemical information	specialty
SEM/EDX	√	√(FIB)	×	good for a first look
STEM/EDX	√	√(TEM lamella)	√[a]×	STEM-EDX to visualize coating
TEM	√×	√	×	only primary particles are visible, crystallinity of coating
XPS	×	√×	√	oxidation state + some thickness information
Raman	√	×	√	not much experimental effort needed for structural information
SIMS	√×	×	√×	imaging can show differences before and after cycling (degradation)
LEIS	×	√× (covering)	√	surface composition and covering of the coating accessible

[a]Chemical information can be obtained with STEM-EELS, which was not performed but is possible.

1. SEM/EDX is helpful to check whether a deposition was successful in general. It must be considered that the electron beam can initiate electrochemical reactions and degradation processes resulting in a continuously changing sample.
2. The grinding approach for TEM analysis is quite challenging due to the high number of uncoated primary particles, but the coating thickness can easily be determined if a coated primary particle is found. Additionally, the crystallinity of the coating can easily be checked in this way.
3. When using FIB preparation approach for STEM analysis, the CAM should always be covered with a protective layer (e.g., Pt) to protect the coating layer itself. The protection layer(s) can induce projection artifacts, which can be compensated by SEM analyses or using STEM/EDX to localize the coating elements in the STEM image.
4. The material contrast in BSE images might be poor depending on the mass differences between coating material and CAM. EDX analysis can help here to localize the coating. In the case of FIB cross sections, it should be noted that a strong contrast in the interfacial region can also result from material redeposition effects caused by the FIB milling process. To distinguish between the actual coating and the redeposited layer, checking the layer thickness can be helpful, since redeposited layers are typically much thicker than coatings.
5. For XPS measurements on coated CAMs, detrimental effects such as differential charging and potential gradients must be taken into account to avoid a misleading energy calibration. If the energy calibration is performed correctly, XPS can be used to determine the binding energies and thus the chemical state for the coating elements.
6. Raman spectroscopy can be used in combination with reference samples as a relatively fast method to check whether the coating process was successful. A basic requirement for this is that the coating material shows Raman-active vibrations.
7. For ToF-SIMS measurements, it is recommended to embed the CAM particles and create a FIB crater before the actual measurement to avoid differential sputtering and coating destruction during depth profiling. It is important to check whether the secondary ion signals from the coating can be better detected in positive- or negative-ion mode. Additionally, mass interferences must be considered in this context to find the more suitable measuring mode. Several cleaning steps of the crater sidewall should be performed to monitor the cleaning process in detail and to avoid removal of the coating. Overall, ToF-SIMS allows for visualization of the coating around several secondary particles at once together with chemical information.
8. LEIS is the only analytical method that can determine the outermost surface composition on an atomic scale and quantify the coverage of coatings. It must be considered that lighter elements are harder to detect than heavier elements (Li needs pulsing of the primary ion beam). LEIS has no matrix effect, which allows for quantification of the surface composition.
9. Finally, we want to point out that not all analytical methods are suitable for every coating material, e.g., due to poor ionization probabilities, non-Raman-active vibrations, to name a few. Accordingly, each coating may require its own analytical approach.

https://doi.org/10.1021/acsaem.1c01255
ACS Appl. Energy Mater. 2021, 4, 7168−7181

EXPERIMENTAL SECTION

TiO_2 Coating by ALD. For the optimization of the ALD process of TiO_2, the deposition process was first adjusted on Si(100) wafers (Siegert Wafer, Aachen, Germany) with a 275 nm SiO_2 layer thermally produced by the manufacturer, and on SiO_2 particles (LiChrospher Si 100) (MZ Analysetechnik, Mainz, Germany, 5 μm diameter). Finally, $LiNi_{0.6}Co_{0.2}Mn_{0.2}O_2$ particles (NCM622 (BASF, Germany)) were coated in an ALD system R-200 (PicoSun Oy, Masala, Finland). A powder sample holder from PicoSun and the PicoflowTM Diffusion Enhancer were used. $TiCl_4$ and H_2O were used as precursor A and precursor B, respectively. The sample temperature was 150 °C, and the pulsing times of precursor A and B were 0.1 and 3.0 s, respectively. A purge time of 30 s after every pulse was used, and the number of cycles was between 50 and 400.

Scanning Electron Microscopy/Energy-Dispersive X-ray Spectroscopy. Images of the morphology of the particles before and after deposition were acquired in a high-resolution SEM (Merlin Zeiss, Oberkochen, Germany). The NCM particles were fixed with conductive double-sided adhesive carbon tabs. Imaging was carried out with the in-lens and SE2 secondary electron detectors at an accelerating voltage of 4 kV. The homogeneity of the coating regarding the local element distribution was examined by EDX (Oxford Instruments, U.K.) with an X-Max 50 detector at an accelerating voltage of 7 kV.

Focused Ion Beam Scanning Electron Microscopy. Cross sections were prepared with a Xeia3 GMU (Tescan GmbH, Brno, Czech Republic) Xe plasma focused ion beam scanning electron microscope (FIB-SEM) at a xenon beam energy of 30 kV. The NCM particles were fixed with conductive double-sided adhesive carbon tabs. Before cross-sectioning, a suitable particle was selected in the secondary electron image. A thin layer of platinum was first deposited by electron beam deposition followed by a thicker layer of platinum of about 2.5 μm by ion beam deposition (Xe, 3 kV) to protect the surface. The cross section was cut and polished in one step (Xe, 30 kV). The sample transfer was carried out with the Leica EM VCT500 (Leica GmbH, Wetzlar, Germany) transfer system.

Transmission Electron Microscopy. To get information about the TiO_2 layer thickness, the coated NCM622 particles got dispersed in ethanol, fixed on carbon-coated copper tape, and were dried in air. Images were taken with a Philips CM30 transmission electron microscope (Philips, Amsterdam, Netherlands) operated with an acceleration voltage of 300 kV.

Scanning Transmission Electron Microscopy (STEM). STEM imaging and EDX (energy-dispersive X-ray) analysis were performed at Marburg University in a double aberration-corrected JEOL JEM-2200FS TEM (JOEL Ltd., Akishima, Japan) equipped with EDX system. The microscope was operated at 200 kV. Unlike the sample prepared for TEM analysis, the sample for STEM analysis was prepared using a JEOL JIB-4601F Multi beam SEM/FIB (focused ion beam). A secondary particle as shown in Supporting Information S4a was selected for the sample preparation. First, a tungsten layer of about 30 nm thickness was deposited using the electron beam. This is to protect the surface from coming into direct contact with the Ga-ion beam. Then, a carbon layer of around 200 nm thickness was deposited using the Ga-ion beam at 30 kV choosing an ion beam current of about 10 pA. Afterward, a tungsten layer of about 3 μm thickness was deposited using the Ga-ion beam at 30 kV with an ion beam current of about 1 nA. Such a preparation has proven to be useful for high-resolution STEM imaging for the analysis of primary particles located in the interior of secondary particles.[62,63]

X-ray Photoelectron Spectroscopy. XPS measurements were carried out with a PHI VersaProbe II instrument (Physical Electronics GmbH, Feldkirchen, Germany). The NCM powders were measured in Teflon cups and fixed with electrically isolating adhesive tape. The powders were transferred into an airtight transfer vessel under an argon atmosphere. Charge neutralization was carried out with the electron and ion gun. Monochromatic Al Kα radiation was used for analysis (1486.6 eV). The power of the X-ray source was 100 W, and the beam voltage was 20 kV (high-power mode). The examined area was 1 mm^2. For the survey spectra, a pass energy of 93.5 eV, and for the detail spectra, a pass energy of 23.5 eV were applied. The pressure during analysis was in the range of $\sim 5 \times 10^{-7}$ Pa. For data evaluation, the software CasaXPS (version 2.3.18, Casa Software Ltd.) was used. All data were calibrated in relation to the signal of adventitious carbon at 284.8 eV. A Shirley background and Gauss-Lorentz (GL (30)) line shapes were applied for data evaluation.

Raman Spectroscopy. Raman measurements were conducted on uncoated NCM622, TiO_2-coated NCM622 after 200 and 400 ALD cycles, and amorphous TiO_2 powder. The powders were transferred into an airtight sample holder under an argon atmosphere from the glovebox to the Raman spectrometer. Raman spectra have been measured in backscattering geometry through the uncoated fused silica window (Edmund Optics, Barrington, United States) of the sample holder. The uncoated window had a thickness of 3 mm and a surface flatness of 1 λ. The Raman setup consisted of a top-illuminating bright-field microscope (Leica GmbH, Wetzlar, Germany) with a 50× / 0.35 NA objective (Olympus) and a Renishaw InVia Raman spectrometer (Renishaw plc., Gloucestershire, Great Britain) equipped with a charge-coupled device camera providing a spatial resolution <2 cm^{-1}. The intensity of the argon-ion laser with a wavelength of 514 nm was <8 mW. A measurement routine for Raman mappings was used in a way that the lateral spacing between individual measurement spots on the surface of the particle agglomerates was 8 μm in both directions. The acquisition time for an individual Raman spectrum was 5 × 100 s at each measurement spot.

Time-of-Flight Secondary Ion Mass Spectrometry. Mass spectrometric crater wall imaging was performed using a TOF.SIMS 5 instrument (IONTOF GmbH, Münster, Germany) equipped with a 25 keV Bi cluster primary ion gun for analysis and a 30 keV Ga FIB gun. A 45° crater (100 μm × 80 μm, 20.20 nA, 700 μm aperture, 80 μs dwell time, 512 × 512 pixels, 1 cycle) was milled into particles embedded in Technovit 4004 (Kulzer GmbH, Hanau, Germany), and the 45° wall was analyzed after four cleaning steps (2 min with 20% DC (0.13 pA) current 512 × 512 pixels each) with the primary ion gun.

ToF-SIMS imaging was performed on an M6 Hybrid SIMS instrument (IONTOF GmbH, Münster, Germany) equipped with a 30 keV Bi cluster primary ion gun. All ToF-SIMS measurements were carried out in positive-ion mode because the comparison of surface spectra in negative and positive modes showed that the intensity of the relevant secondary ion signals in the positive mode was much higher and mass interferences could be avoided. For crater wall imaging, the liquid metal ion gun (LMIG) was operated in imaging mode with the 200 μm beam defining aperture in combination with the delayed extraction mode for the analyzer. The topography mode of the analyzer was activated to increase the total ion count. Imaging was carried out with 30 keV Bi_3^+ primary ions (I = 0.394 pA) at a cycle time of 45 μs and a chamber pressure of 5×10^{-6} mbar argon as well as low-energy electron flooding for charge compensation. The pixel resolution was 98 nm and the obtained mass resolution $m/\Delta m$ @ FWHM 2996 for Ti^+ (m/z = 47.95 amu). The data evaluation was carried out with the software SurfaceLab 7.1 (IONTOF GmbH, Münster, Germany).

Low-Energy Ion Scattering. LEIS was performed with a Qtac[100] instrument (IONTOF GmbH, Münster, Germany) equipped with an electron ionization source to produce a noble gas beam (e.g., He^+, Ne^+, and Ar^+) at the Imperial College in London. The primary ion beam is oriented 90° to the sample surface and its energy can be adjusted between 1 and 8 keV. The backscattered ions are analyzed in a double toroidal analyzer (DTA) with improved detection limits and mass resolution compared to conventional instruments.[64] The instrument is also equipped with a low-energy argon sputter gun for depth profiling or cleaning (0.2 keV, 200 nA) of the sample surface. Surface spectra and depth profiles were carried out using He^+ (4 keV) and Ne^+ (5−6 keV) as primary ions. The NCM powder was pressed by hand in a shallow metal mold for analysis. Data evaluation was carried out with the software SurfaceLab 7.1 (IONTOF GmbH, Münster, Germany).

https://doi.org/10.1021/acsaem.1c01255
ACS Appl. Energy Mater. 2021, 4, 7168−7181

■ ASSOCIATED CONTENT

Supporting Information

The Supporting Information is available free of charge at https://pubs.acs.org/doi/10.1021/acsaem.1c01255.

SE image and EDX mapping of coated NCM622; BSE image of coated NCM851005; sketch to understand the origin of different coating thicknesses after the ALD process; SE images showing the TEM sample preparation; XPS detail spectra (C 1s spectra of all samples, Cl 2p detail spectrum of coated NCM622 (50 ALD cycles)); schematic comparing different sample preparation approaches for ToF-SIMS analysis; and sputter depth as a function of the mixing ratio of Technovit 4004 (powder/liquid) (PDF)

■ AUTHOR INFORMATION

Corresponding Authors

Marcus Rohnke − *Institute of Physical Chemistry, Justus Liebig University Giessen, D-35392 Giessen, Germany; Center for Materials Research (LaMa), Justus Liebig University Giessen, D-35392 Giessen, Germany;* orcid.org/0000-0002-8867-950X; Email: Marcus.Rohnke@phys.chemie.uni-giessen.de

Jürgen Janek − *Institute of Physical Chemistry, Justus Liebig University Giessen, D-35392 Giessen, Germany; Center for Materials Research (LaMa), Justus Liebig University Giessen, D-35392 Giessen, Germany;* orcid.org/0000-0002-9221-4756; Email: Juergen.Janek@phys.chemie.uni-giessen.de

Authors

Yannik Moryson − *Institute of Physical Chemistry, Justus Liebig University Giessen, D-35392 Giessen, Germany; Center for Materials Research (LaMa), Justus Liebig University Giessen, D-35392 Giessen, Germany*

Felix Walther − *Institute of Physical Chemistry, Justus Liebig University Giessen, D-35392 Giessen, Germany; Center for Materials Research (LaMa), Justus Liebig University Giessen, D-35392 Giessen, Germany*

Joachim Sann − *Institute of Physical Chemistry, Justus Liebig University Giessen, D-35392 Giessen, Germany; Center for Materials Research (LaMa), Justus Liebig University Giessen, D-35392 Giessen, Germany*

Boris Mogwitz − *Institute of Physical Chemistry, Justus Liebig University Giessen, D-35392 Giessen, Germany; Center for Materials Research (LaMa), Justus Liebig University Giessen, D-35392 Giessen, Germany*

Shamail Ahmed − *Materials Science Centre and Faculty of Physics, Philipps University Marburg, D-35043 Marburg, Germany*

Simon Burkhardt − *Institute of Physical Chemistry, Justus Liebig University Giessen, D-35392 Giessen, Germany; Center for Materials Research (LaMa), Justus Liebig University Giessen, D-35392 Giessen, Germany*

Limei Chen − *Institute of Experimental Physics I, Justus Liebig University Giessen, D-35392 Giessen, Germany*

Peter J. Klar − *Institute of Experimental Physics I and Center for Materials Research (LaMa), Justus Liebig University Giessen, D-35392 Giessen, Germany;* orcid.org/0000-0002-4513-0330

Kerstin Volz − *Materials Science Centre and Faculty of Physics, Philipps University Marburg, D-35043 Marburg, Germany*

Sarah Fearn − *Department of Materials, Imperial College London, SW7 2AZ London, U.K.*

Complete contact information is available at: https://pubs.acs.org/10.1021/acsaem.1c01255

Notes

The authors declare no competing financial interest.

■ ACKNOWLEDGMENTS

Funding by Federal Ministry of Education and Research (BMBF, Germany) within the cluster of competence FESTBATT (project 03XP0176D) is acknowledged by J.J.; J.J. and M.R. thank the DFG for funding of the Hybrid SIMS under grant number INST 162/544-1 FUGG.

■ REFERENCES

(1) Neudeck, S.; Mazilkin, A.; Reitz, C.; Hartmann, P.; Janek, J.; Brezesinski, T. Effect of Low-Temperature Al_2O_3 ALD Coating on Ni-Rich Layered Oxide Composite Cathode on the Long-Term Cycling Performance of Lithium-Ion Batteries. *Sci. Rep.* **2019**, *9*, No. 5328.

(2) Wen, L.; Wang, X.; Liu, G. Q.; Luo, H. Z.; Liang, J.; Dou, S. X. Novel surface coating strategies for better battery materials. *Surf. Innov.* **2017**, *6*, 1−23.

(3) Koerver, R.; Aygün, I.; Leichtweiß, T.; Dietrich, C.; Zhang, W.; Binder, J. O.; Hartmann, P.; Zeier, W. G.; Janek, J. Capacity Fade in Solid-State Batteries: Interphase Formation and Chemomechanical Processes in Nickel-Rich Layered Oxide Cathodes and Lithium Thiophosphate Solid Electrolytes. *Chem. Mater.* **2017**, *29*, 5574−5582.

(4) Yada, C.; Lee, C. E.; Laughman, D.; Hannah, L.; Iba, H.; Hayden, B. E. A High-Throughput Approach Developing Lithium-Niobium-Tantalum Oxides as Electrolyte/Cathode Interlayers for High-Voltage All-Solid-State Lithium Batteries. *J. Electrochem. Soc.* **2015**, *162*, A722−A726.

(5) Yada, C.; Ohmori, A.; Ide, K.; Yamasaki, H.; Kato, T.; Saito, T.; Sagane, F.; Iriyama, Y. Dielectric modification of 5V-class cathodes for high-voltage all-solid-state lithium batteries. *Adv. Energy Mater.* **2014**, *4*, No. 1301416.

(6) Liu, W.; Oh, P.; Liu, X.; Lee, M. J.; Cho, W.; Chae, S.; Kim, Y.; Cho, J. Nickel-Rich Layered Lithium Transition-Metal Oxide for High-Energy Lithium-Ion Batteries. *Angew. Chem., Int. Ed.* **2015**, *54*, 4440−4457.

(7) Kondrakov, A. O.; Schmidt, A.; Xu, J.; Geßwein, H.; Mönig, R.; Hartmann, P.; Sommer, H.; Brezesinski, T.; Janek, J. Anisotropic Lattice Strain and Mechanical Degradation of High- and Low-Nickel NCM Cathode Materials for Li-Ion Batteries. *J. Phys. Chem. C* **2017**, *121*, 3286−3294.

(8) Kang, Y. J.; Kim, J. H.; Lee, S. W.; Sun, Y. K. The effect of $Al(OH)_3$ coating on the $Li[Li_{0.2}Ni_{0.2}Mn_{0.6}]O_2$ cathode material for lithium secondary battery. *Electrochim. Acta* **2005**, *50*, 4784−4791.

(9) MacHida, N.; Kashiwagi, J.; Naito, M.; Shigematsu, T. Electrochemical properties of all-solid-state batteries with ZrO_2-coated $LiNi_{1/3}Mn_{1/3}Co_{1/3}O_2$ as cathode materials. *Solid State Ionics* **2012**, *225*, 354−358.

(10) Ito, S.; Fujiki, S.; Yamada, T.; Aihara, Y.; Park, Y.; Kim, T. Y.; Baek, S. W.; Lee, J. M.; Doo, S.; Machida, N. A rocking chair type all-solid-state lithium ion battery adopting Li 2O-ZrO2 coated $LiNi_{0.8}Co_{0.15}Al_{0.05}O_2$ and a sulfide based electrolyte. *J. Power Sources* **2014**, *248*, 943−950.

(11) Huang, Y.; Huang, Y.; Hu, X. Enhanced electrochemical performance of $LiNi_{0.8}Co_{0.15}Al_{0.05}O_2$ by nanoscale surface modification with Co_3O_4. *Electrochim. Acta* **2017**, *231*, 294−299.

(12) Takada, K.; Ohta, N.; Zhang, L.; Xu, X.; Hang, B. T.; Ohnishi, T.; Osada, M.; Sasaki, T. Interfacial phenomena in solid-state lithium battery with sulfide solid electrolyte. *Solid State Ionics* **2012**, *225*, 594−597.

(13) Lai, Y. Q.; Xu, M.; Zhang, Z. A.; Gao, C. H.; Wang, P.; Yu, Z. Y. Optimized structure stability and electrochemical performance of $LiNi_{0.8}Co_{0.15}Al_{0.05}O_2$ by sputtering nanoscale ZnO film. *J. Power Sources* **2016**, *309*, 20−26.
(14) Han, X.; Gong, Y.; Fu, K.; He, X.; Hitz, G. T.; Dai, J.; Pearse, A.; Liu, B.; Wang, H.; Rubloff, G.; Mo, Y.; Thangadurai, V.; Wachsman, E. D.; Hu, L. Negating interfacial impedance in garnet-based solid-state Li metal batteries. *Nat. Mater.* **2017**, *16*, 572−579.
(15) Herzog, M. J.; Esken, D.; Janek, J. Improved Cycling Performance of High-Nickel NMC by Dry Powder Coating with Nanostructured Fumed Al_2O_3, TiO_2, and ZrO_2: A Comparison. *Batteries Supercaps* **2021**, 1−16.
(16) Herzog, M. J.; Gauquelin, N.; Esken, D.; Verbeeck, J.; Janek, J. Facile Dry Coating Method of High-Nickel Cathode Material by Nanostructured Fumed Alumina (Al2O3) Improving the Performance of Lithium-Ion Batteries. *Energy Technol.* **2021**, No. 2100028.
(17) Culver, S. P.; Koerver, R.; Zeier, W. G.; Janek, J. On the Functionality of Coatings for Cathode Active Materials in Thiophosphate-Based All-Solid-State Batteries. *Adv. Energy Mater.* **2019**, *9*, No. 1900626.
(18) Kim, A. Y.; Strauss, F.; Bartsch, T.; Teo, J. H.; Hatsukade, T.; Mazilkin, A.; Janek, J.; Hartmann, P.; Brezesinski, T. Stabilizing Effect of a Hybrid Surface Coating on a Ni-Rich NCM Cathode Material in All-Solid-State Batteries. *Chem. Mater.* **2019**, *31*, 9664−9672.
(19) Strauss, F.; Teo, J. H.; Maibach, J.; Kim, A. Y.; Mazilkin, A.; Janek, J.; Brezesinski, T. Li_2ZrO_3-Coated NCM622 for Application in Inorganic Solid-State Batteries: Role of Surface Carbonates in the Cycling Performance. *ACS Appl. Mater. Interfaces* **2020**, *12*, 57146−57154.
(20) Jung, R.; Morasch, R.; Karayaylali, P.; Phillips, K.; Maglia, F.; Stinner, C.; Shao-Horn, Y.; Gasteiger, H. A. Effect of Ambient Storage on the Degradation of Ni-Rich Positive Electrode Materials (NMC811) for Li-Ion Batteries. *J. Electrochem. Soc.* **2018**, *165*, A132−A141.
(21) Kong, J. Z.; Ren, C.; Tai, G. A.; Zhang, X.; Li, A. D.; Wu, D.; Li, H.; Zhou, F. Ultrathin ZnO coating for improved electrochemical performance of $LiNi_{0.5}Co_{0.2}Mn_{0.3}O_2$ cathode material. *J. Power Sources* **2014**, *266*, 433−439.
(22) Kong, J. Z.; Wang, S. S.; Tai, G. A.; Zhu, L.; Wang, L. G.; Zhai, H. F.; Wu, D.; Li, A. D.; Li, H. Enhanced electrochemical performance of $LiNi_{0.5}Co_{0.2}Mn_{0.3}O_2$ cathode material by ultrathin ZrO_2 coating. *J. Alloys Compd.* **2016**, *657*, 593−600.
(23) Shi, Y.; Zhang, M.; Qian, D.; Meng, Y. S. Ultrathin Al_2O_3 Coatings for Improved Cycling Performance and Thermal Stability of $LiNi_{0.5}Co_{0.2}Mn_{0.3}O_2$ Cathode Material. *Electrochim. Acta* **2016**, *203*, 154−161.
(24) Chen, Z.; Chao, D.; Lin, J.; Shen, Z. Recent progress in surface coating of layered $LiNi_xCo_yMn_zO_2$ for lithium-ion batteries. *Mater. Res. Bull.* **2017**, *96*, 491−502.
(25) Qin, C.; Cao, J.; Chen, J.; Dai, G.; Wu, T.; Chen, Y.; Tang, Y.; Li, A.; Chen, Y. Improvement of electrochemical performance of nickel rich $LiNi_{0.6}Co_{0.2}Mn_{0.2}O_2$ cathode active material by ultrathin TiO_2 coating. *Dalton Trans.* **2016**, *45*, 9669−9675.
(26) Chen, Z.; Qin, Y.; Amine, K.; Sun, Y. K. Role of surface coating on cathode materials for lithium-ion batteries. *J. Mater. Chem.* **2010**, *20*, 7606−7612.
(27) Razmjoo Khollari, M. A.; Paknahad, P.; Ghorbanzadeh, M. Improvement of the electrochemical performance of a nickel rich $LiNi_{0.5}Co_{0.2}Mn_{0.3}O_2$ cathode material by reduced graphene oxide/SiO2 nanoparticle double-layer coating. *New J. Chem.* **2019**, *43*, 2766−2775.
(28) Flores, E.; Novák, P.; Berg, E. J. In situ and Operando Raman spectroscopy of layered transition metal oxides for Li-ion battery cathodes. *Front. Energy Res.* **2018**, *6*, No. 82.
(29) Tornheim, A.; Maroni, V. A.; He, M.; Gosztola, D. J.; Zhang, Z. Enhanced Raman Scattering from NCM523 Cathodes Coated with Electrochemically Deposited Gold. *J. Electrochem. Soc.* **2017**, *164*, A3000−A3005.
(30) Wu, Y.; Li, M.; Wahyudi, W.; Sheng, G.; Miao, X.; Anthopoulos, T. D.; Huang, K. W.; Li, Y.; Lai, Z. Performance and Stability Improvement of Layered NCM Lithium-Ion Batteries at High Voltage by a Microporous Al_2O_3 Sol-Gel Coating. *ACS Omega* **2019**, *4*, 13972−13980.
(31) Walther, F.; Koerver, R.; Fuchs, T.; Ohno, S.; Sann, J.; Rohnke, M.; Zeier, W. G.; Janek, J. Visualization of the Interfacial Decomposition of Composite Cathodes in Argyrodite-Based All-Solid-State Batteries Using Time-of-Flight Secondary-Ion Mass Spectrometry. *Chem. Mater.* **2019**, 3745−3755.
(32) Brongersma, H. H.; Draxler, M.; de Ridder, M.; Bauer, P. Surface composition analysis by low-energy ion scattering. *Surf. Sci. Rep.* **2007**, *62*, 63−109.
(33) Samavat, F.; King, B. V.; John O'Connor, D. Low energy ion scattering. *Surf. Rev. Lett.* **2007**, *14*, 31−41.
(34) Téllez, H.; Aguadero, A.; Druce, J.; Burriel, M.; Fearn, S.; Ishihara, T.; McPhail, D. S.; Kilner, J. A. New perspectives in the surface analysis of energy materials by combined time-of-flight secondary ion mass spectrometry (ToF-SIMS) and high sensitivity low-energy ion scattering (HS-LEIS). *J. Anal. At. Spectrom.* **2014**, *29*, 1361−1370.
(35) Hoskins, A. L.; McNeary, W. W.; Millican, S. L.; Gossett, T. A.; Lai, A.; Gao, Y.; Liang, X.; Musgrave, C. B.; Weimer, A. W. Nonuniform Growth of Sub-2 Nanometer Atomic Layer Deposited Alumina Films on Lithium Nickel Manganese Cobalt Oxide Cathode Battery Materials. *ACS Appl. Nano Mater.* **2019**, 6989−6997.
(36) Lou, S.; Yu, Z.; Liu, Q.; Wang, H.; Chen, M.; Wang, J. Multi-scale Imaging of Solid-State Battery Interfaces: From Atomic Scale to Macroscopic Scale. *Chem* **2020**, *6*, 2199−2218.
(37) Piao, J. Y.; Sun, Y. G.; Duan, S. Y.; Cao, A. M.; Wang, X. L.; Xiao, R. J.; Yu, X. Q.; Gong, Y.; Gu, L.; Li, Y.; Liu, Z. J.; Peng, Z. Q.; Qiao, R. M.; Yang, W. L.; Yang, X. Q.; Goodenough, J. B.; Wan, L. J. Stabilizing Cathode Materials of Lithium-Ion Batteries by Controlling Interstitial Sites on the Surface. *Chem* **2018**, *4*, 1685−1695.
(38) Zhang, Y. Q.; Tian, Y.; Xiao, Y.; Miara, L. J.; Aihara, Y.; Tsujimura, T.; Shi, T.; Scott, M. C.; Ceder, G. Direct Visualization of the Interfacial Degradation of Cathode Coatings in Solid State Batteries: A Combined Experimental and Computational Study. *Adv. Energy Mater.* **2020**, No. 1903778.
(39) Koerver, R.; Walther, F.; Aygün, I.; Sann, J.; Dietrich, C.; Zeier, W. G.; Janek, J. Redox-active cathode interphases in solid-state batteries. *J. Mater. Chem. A* **2017**, *5*, 22750−22760.
(40) Wu, X.; Villevieille, C.; Novák, P.; El Kazzi, M. Monitoring the chemical and electronic properties of electrolyte-electrode interfaces in all-solid-state batteries using: Operando X-ray photoelectron spectroscopy. *Phys. Chem. Chem. Phys.* **2018**, *20*, 11123−11129.
(41) Kato, A.; Kowada, H.; Deguchi, M.; Hotehama, C.; Hayashi, A.; Tatsumisago, M. XPS and SEM analysis between Li/Li_3PS_4 interface with Au thin film for all-solid-state lithium batteries. *Solid State Ionics* **2018**, *322*, 1−4.
(42) Naumkin, A. V.; Kraut-Vass, A.; Gaarenstroom, S. W.; Powell, C. J. *NIST X-ray Photoelectron Spectroscopy Database 20*, version 4.1. https://srdata.nist.gov/xps/, 2012.
(43) Tanuma, S.; Powell, C. J.; Penn, D. R. Calculation of electron inelastic mean free paths (IMFPs) VII. Reliability of the TPP-2M IMFP predictive equation. *Surf. Interface Anal.* **2003**, *35*, 268−275.
(44) Oswald, S.; Thoss, F.; Zier, M.; Hoffmann, M.; Jaumann, T.; Herklotz, M.; Nikolowski, K.; Scheiba, F.; Kohl, M.; Giebeler, L.; Mikhailova, D.; Ehrenberg, H. Binding energy referencing for XPS in Alkali metal-based battery materials research (II): Application to complex composite electrodes. *Batteries* **2018**, *4*, No. 36.
(45) Greczynski, G.; Hultman, L. X-ray photoelectron spectroscopy: Towards reliable binding energy referencing. *Prog. Mater. Sci.* **2020**, *107*, No. 100591.
(46) Maibach, J.; Lindgren, F.; Eriksson, H.; Edström, K.; Hahlin, M. Electric Potential Gradient at the Buried Interface between Lithium-Ion Battery Electrodes and the SEI Observed Using Photoelectron Spectroscopy. *J. Phys. Chem. Lett.* **2016**, *7*, 1775−1780.

https://doi.org/10.1021/acsaem.1c01255
ACS Appl. Energy Mater. 2021, 4, 7168−7181

(47) Baddour-Hadjean, R.; Pereira-Ramos, J. P. Raman microspectrometry applied to the study of electrode materials for lithium batteries. *Chem. Rev.* **2010**, *110*, 1278−1319.
(48) Julien, C. M.; Mauger, A. In situ Raman analyses of electrode materials for Li-ion batter. *AIMS Mater. Sci.* **2018**, *5*, 650−698.
(49) Wang, C.; Yu, R.; Hwang, S.; Liang, J.; Li, X.; Zhao, C.; Sun, Y.; Wang, J.; Holmes, N.; Li, R.; Huang, H.; Zhao, S.; Zhang, L.; Lu, S.; Su, D.; Sun, X. Single crystal cathodes enabling high-performance all-solid-state lithium-ion batteries. *Energy Storage Mater.* **2020**, *30*, 98−103.
(50) Qian, G.; Zhang, Y.; Li, L.; Zhang, R.; Xu, J.; Cheng, Z.; Xie, S.; Wang, H.; Rao, Q.; He, Y.; Shen, Y.; Chen, L.; Tang, M.; Ma, Z. F. Single-crystal nickel-rich layered-oxide battery cathode materials: synthesis, electrochemistry, and intra-granular fracture. *Energy Storage Mater.* **2020**, *27*, 140−149.
(51) Ghanty, C.; Markovsky, B.; Erickson, E. M.; Talianker, M.; Haik, O.; Tal-Yossef, Y.; Mor, A.; Aurbach, D.; Lampert, J.; Volkov, A.; Shin, J. Y.; Garsuch, A.; Chesneau, F. F.; Erk, C. Li+-Ion Extraction/Insertion of Ni-Rich $Li_{1+x}(Ni_yCo_zMn_z)_wO_2$ ($0.005 < x < 0.03$; y: Z = 8:1, w ≈ 1) Electrodes: In Situ XRD and Raman Spectroscopy Study. *ChemElectroChem* **2015**, *2*, 1479−1486.
(52) Code, L. Investigation on Degradation Mechanism of under the High Temperature. Master's Thesis, Seulgi Shin Department of Energy Engineering Graduate School of UNIST, 2019.
(53) Gilbert, J. A.; Maroni, V. A.; Cui, Y.; Gosztola, D. J.; Miller, D. J.; Abraham, D. P. Composition and Impedance Heterogeneity in Oxide Electrode Cross-Sections Detected by Raman Spectroscopy. *Adv. Mater. Interfaces* **2018**, *5*, No. 1701447.
(54) Saavedra-Arias, J. J.; Karan, N. K.; Pradhan, D. K.; Kumar, A.; Nieto, S.; Thomas, R.; Katiyar, R. S. Synthesis and electrochemical properties of $Li(Ni_{0.8}Co_{0.1}Mn_{0.1})O_2$ cathode material: Ex situ structural analysis by Raman scattering and X-ray diffraction at various stages of charge-discharge process. *J. Power Sources* **2008**, *183*, 761−765.
(55) Schipporeit, S.; Mergel, D. Spectral decomposition of Raman spectra of mixed-phase TiO_2 thin films on Si and silicate substrates. *J. Raman Spectrosc.* **2018**, *49*, 1217−1229.
(56) Li, J. G.; Ishigaki, T.; Sun, X. Anatase, brookite, and rutile nanocrystals via redox reactions under mild hydrothermal conditions: Phase-selective synthesis and physicochemical properties. *J. Phys. Chem. C* **2007**, *111*, 4969−4976.
(57) Li, W.; Dolocan, A.; Oh, P.; Celio, H.; Park, S.; Cho, J.; Manthiram, A. Dynamic behaviour of interphases and its implication on high-energy-density cathode materials in lithium-ion batteries. *Nat. Commun.* **2017**, *8*, No. 14589.
(58) Bessette, S.; Paolella, A.; Kim, C.; Zhu, W.; Hovington, P.; Gauvin, R.; Zaghib, K. Nanoscale Lithium Quantification in LiXNiyCowMnZO2 as Cathode for Rechargeable Batteries. *Sci. Rep.* **2018**, *8*, No. 17575.
(59) Yamagishi, Y.; Morita, H.; Nomura, Y.; Igaki, E. Visualizing Lithium Distribution and Degradation of Composite Electrodes in Sul fi de-based All-Solid-State Batteries Using Operando Time-of-Flight Secondary Ion Mass Spectrometry. *ACS Appl. Mater. Interfaces* **2021**, 580−586.
(60) Neudeck, S.; Walther, F.; Bergfeldt, T.; Suchomski, C.; Rohnke, M.; Hartmann, P.; Janek, J.; Brezesinski, T. Molecular Surface Modification of NCM622 Cathode Material Using Organophosphates for Improved Li-Ion Battery Full-Cells. *ACS Appl. Mater. Interfaces* **2018**, *10*, 20487−20498.
(61) Walther, F.; Strauss, F.; Wu, X.; Mogwitz, B.; Hertle, J.; Sann, J.; Rohnke, M.; Brezesinski, T.; Janek, J. The Working Principle of a Li_2CO_3 /$LiNbO_3$ Coating on NCM for Thiophosphate-Based All-Solid-State Batteries. *Chem. Mater.* **2021**, 2110−2125.
(62) Ahmed, S.; Pokle, A.; Schweidler, S.; Beyer, A.; Bianchini, M.; Walther, F.; Mazilkin, A.; Hartmann, P.; Brezesinski, T.; Janek, J.; Volz, K. The Role of Intragranular Nanopores in Capacity Fade of Nickel-Rich Layered $Li(Ni_{1-x-y}Co_xMn_y)O_2$ Cathode Materials. *ACS Nano* **2019**, *13*, 10694−10704.
(63) Ahmed, S.; Bianchini, M.; Pokle, A.; Munde, M. S.; Hartmann, P.; Brezesinski, T.; Beyer, A.; Janek, J.; Volz, K. Visualization of Light Elements using 4D STEM: The Layered-to-Rock Salt Phase Transition in $LiNiO_2$ Cathode Material. *Adv. Energy Mater.* **2020**, No. 2001026.
(64) Brongersma, H. H.; Grehl, T.; van Hal, P. A.; Kuijpers, N. C. W.; Mathijssen, S. G. J.; Schofield, E. R.; Smith, R. A. P.; ter Veen, H. R. J. High-sensitivity and high-resolution low-energy ion scattering. *Vacuum* **2010**, *84*, 1005−1007.

https://doi.org/10.1021/acsaem.1c01255
ACS Appl. Energy Mater. 2021, 4, 7168−7181

3.2 Publication 2: “In-Depth Characterization of Lithium-Metal Surfaces with XPS and ToF-SIMS: Toward Better Understanding of the Passivation Layer”

In publication 2 of this doctoral thesis the native passivation layer of different lithium samples, which are used as anodes in LIBs, were examined by ToF-SIMS, XPS and EDX.

With the chemical information provided by XPS and the depth resolution of ToF-SIMS depth profiling a 3D model of the native passivation layer could be created. The native passivation layer on all samples consists of a bi-layer, with a lithium carbonate and lithium hydroxide phase present at the surface and lithium oxide underneath in contact with lithium metal. The thickness of the passivation layer could be determined by ToF-SIMS depth profiling and is for all samples in a few nanometer range but is heavily influenced by residual contaminations during storage and sample handling. The most important steps for a comprehensive analysis are highlighted and attention was drawn to common pit falls, such as the lithium plating during electron beam exposure, which lead to misinterpretation in previous publications. Furthermore, the results show that due to the degradation of the lithium samples in UHV and during argon sputtering only samples, which were analyzed under the same conditions are comparable.

Overall, the results of the second publication provide a comprehensive analysis of the native passivation layer of lithium samples with XPS and ToF-SIMS and elucidate the 3D composition of it. Since complete understanding of the lithium substrate before applying coatings is crucial, this work is a necessity for modifying LMAs with ASEIs to improve battery cycling.

The experiments for this work were designed and planned by the first author S.K. Otto under the supervision of A. Henss and J. Janek. The XPS experiments and data analyzation were performed by the second author (Y. Moryson). J. Sann supported the XPS data analyses. The first author performed the EDX and ToF-SIMS measurements and analyzed the data. K. Peppler and A. Henss assisted the scientific discussion of the EDX and ToF-SIMS data, respectively. The manuscript was written by the first author and edited by all co-authors.

CHEMISTRY OF MATERIALS

pubs.acs.org/cm Article

In-Depth Characterization of Lithium-Metal Surfaces with XPS and ToF-SIMS: Toward Better Understanding of the Passivation Layer

Svenja-K. Otto, Yannik Moryson, Thorben Krauskopf, Klaus Peppler, Joachim Sann, Jürgen Janek, and Anja Henss*

Cite This: *Chem. Mater.* 2021, 33, 859−867 Read Online

ACCESS | Metrics & More | Article Recommendations | Supporting Information

ABSTRACT: To significantly increase the energy density of lithium-based batteries, the use of lithium metal as an anode is an option despite all of the associated challenges. Due to its high reactivity, lithium is covered with a passivation layer that may affect cell performance and reproducibility of electrochemical characterization. In most studies, this is ignored and lithium metal is used without considering the passivation layer and carrying out a proper characterization of the surface. Against this background, we systematically characterized various lithium samples with X-ray photoelectron spectroscopy (XPS), time-of-flight secondary-ion mass spectrometry (ToF-SIMS), and complementary energy-dispersive X-ray spectroscopy (EDX), resulting in a complete three-dimensional chemical picture of the surface passivation layer. On all analyzed lithium samples, our measurements indicate a nanometer-thick inorganic passivation layer consisting of an outer lithium hydroxide and carbonate layer and an inner lithium oxide-rich region. The specific thickness and composition of the passivation layer depend on the treatment before use and the storage and transport conditions. Besides, we offer guidelines for experimental design and data interpretation to ensure reliable and comparable experimental conditions and results. Lithium plating through electron beam exposure on electrically contacted samples, the reactivity of freshly formed lithium metal even under ultrahigh-vacuum (UHV) conditions, and the decomposition of lithium compounds by argon sputtering are identified as serious pitfalls for reliable lithium surface characterization.

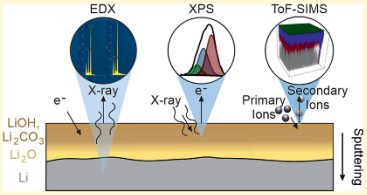

INTRODUCTION

The challenges of electrical energy storage and electrification of transportation are the driving force behind intensive effort in the development of improved lithium-ion batteries (LIB). Widely, lithium metal is considered as a promising next-generation anode material that could meet the demand for batteries with higher energy and power density than commonly used LIBs.[1] Therefore, lithium-metal anodes (LMAs) have attracted extensive research interest due to its kinetics and morphology.[2−4] Still, the application of lithium anodes faces serious challenges and problems, such as low coulombic efficiency, morphological instability, poor cycle life, and safety issues, that have not been solved yet.[5−7]

In this context, a number of previous reports as well as recent papers emphasize the importance of precise knowledge on the properties of the lithium surface and its passivation layer for battery applications.[8−10] These reports mostly agree that the passivation layer is crucial for the cell performance, as it influences the reactivity toward the electrolyte.[11−15] In 2003, Naudin et al. summarized the known information in a surface passivation model, assuming an outer layer of thickness 1−20 nm composed of Li_2CO_3 and LiOH, as well as an inner Li_2O layer of thickness 10−100 nm.[16] Mainly, X-ray photoelectron spectroscopy (XPS), infrared (IR) spectroscopy, and Raman spectroscopy were used as analytical methods.[16,17] More recent reports aim to understand the effects of the lithium passivation layer and any surface contamination in more detail. For example, Kamphaus et al. investigated the influence of Li_2O, LiOH, and Li_2CO_3 surface passivation layers on the interfacial reactivity of the LMA with XPS and ab initio molecular dynamics calculations.[18] Other authors studied the contamination of LMA as a possible cause of dendrite formation.[19−21] Becking et al. modified the surface film on lithium foils with a roll-press technique producing a foil with a thinner and flatter passivation layer, which showed superior cycling behavior.[22] Interesting results on the reactivity and passivation layer of lithium were also obtained in nonbattery applications, e.g., in magnetic fusion energy reactors as a blanket material or as a nuclear reactor coolant.[23−26] Additionally, patent specifications reveal that the surface of commercial lithium metal is commonly prepassivated to reduce corrosion during storage and to increase safety. The described methods include CO_2 gas treatments, wax or polymer coatings, as well as treatments with phosphorous or fluorinating

Received: September 1, 2020
Revised: January 4, 2021
Published: January 19, 2021

https://dx.doi.org/10.1021/acs.chemmater.0c03518
Chem. Mater. 2021, 33, 859−867

agents.[3] All of these reports complement the older model of a LiOH and Li_2CO_3 passivation layer on top of an oxide-rich layer in contact with lithium metal, and they highlight that the chemical nature, morphology, and thickness of the LMA passivation layer influence the reactivity of lithium and the later battery cell performance. Notably, these effects are often not considered in publications targeting battery cell performance, where the LMA surface is usually not analyzed. In case the pristine lithium metal surface is characterized, design and interpretation of the analyses are often poor.

To advance the knowledge on lithium-metal surfaces, to highlight serious pitfalls of analyzing lithium-metal samples and to attract more attention to the surface state of LMAs, we present here results from systematic XPS and time-of-flight secondary-ion mass spectrometry (ToF-SIMS) analyses of various lithium samples, which are commonly used for battery applications. We reveal detailed information on the chemical nature, composition, and spatial and depth distribution of the passivation compounds. Energy-dispersive X-ray spectroscopy (EDX) is considered as an additional nondestructive method to gain more information about thicker passivation layers and bulk regions. Along with the conclusions on the composition and three-dimensional (3D) distribution of compounds in the passivation layer, this multianalytical approach reveals information about factors influencing the passivation layer and demonstrates the potential and limitations of the different techniques. We propose how the analytical techniques should be combined to achieve maximum benefit from their complementary information content. Optimized experimental design, including sample preparation, measurement options, and reference analyses, as well as data interpretation as guidelines for lithium metal surface characterization are suggested. We believe that these factors are important for the understanding of the underlying surface and degradation reactions, which is essential for the characterization, handling, and successful application of LMAs.

■ EXPERIMENTAL SECTION

For highly reactive, air-sensitive samples such as lithium, reliable and reproducible characterization is specifically challenging and requires special precaution. Most importantly, samples have to be protected from undefined changes through reaction with the gas phase on the way to the analysis chamber. Therefore, sample transfer has to be performed without contact with air atmosphere, but unwanted reactions are not limited to the sample transfer and also occur inside the analysis instruments. Therefore, we prepared, transferred, and analyzed all samples which are directly compared under exactly the same conditions. All preparation and sample handling were done in a glovebox under argon atmosphere ($p(H_2O)/p < 0.1$ ppm, $p(O_2)/p < 0.1$ ppm). As reference samples, LiOH (98 wt %), Li_2O_2 (90 wt %), Li_2CO_3 (99.997 wt %), Li_2O (97 wt %), and LiH (95 wt %) powders (all Sigma-Aldrich) were characterized. Before analysis, the powders were either compacted in a handpress or pressed to pellets (3t, 1.5 min). Lithium foil 1 (>99.8 wt %, Albemarle Germany GmbH, former Rockwood Lithium GmbH), lithium foil 2 (>99.9 wt % Li, Honjo Metal), and slices cut from a lithium rod (99.8%, abcr GmbH) were investigated as lithium samples. They were analyzed as received (directly out of the transport packages received from the supplier) or stored in closed plastic boxes under a glovebox atmosphere before analysis.

XPS measurements were carried out with a PHI VersaProbe II instrument (ULVAC-PHI, Inc.). All samples were transferred to the instrument in an argon-filled transfer vessel. Monochromatic Al K_α radiation (1486.6 eV) was used; the power of the X-ray source was 50 or 100 W, and the beam voltage was 15 or 20 kV. The examined areas were 0.03 mm^2 or 1 mm^2. For depth profiling, Ar^+ ions with accelerating voltages between 1 and 4 kV were applied, using the following sputter steps: (1) surface, (2) 3 min 1 kV, (3) 8 min 2 kV, (4) 12 min 4 kV, (5) 30 min 4 kV. For the survey spectra, a pass energy of 93.9 eV, and for the detail spectra, a pass energy of 23.5 eV were used. Data evaluation was carried out with the software CasaXPS (version 2.3.18, Casa Software Ltd). All data were calibrated in relation to the signal of adventitious carbon at 284.8 eV or to the O 1s lithium oxide signal at 528.5 eV if no carbon was present. A Shirley background was used, and all spectra were fitted with a GL line shape, except the asymmetric Li metal signal, where an LF line shape was used. Lithium samples were electrically isolated with nonconductive double-sided tape (tesa) for the measurements if not stated differently.

ToF-SIMS measurements were conducted using a ToF.SIMS 5 instrument (IONTOF GmbH), which is equipped with a 25 kV Bi cluster primary-ion gun for analysis and a 20 kV gas cluster ion beam (GCIB), as well as a dual-source column with Ar^- and Cs^+ low-energy guns for depth profiling. All samples were transferred from the glovebox to the instrument with an argon-filled Leica EM VCT500 shuttle (Leica Microsystems). Depth profiles on lithium foils were measured in spectrometry mode (bunched) and fast imaging mode (unbunched). The spectrometry mode provides a high signal intensity and a high mass resolution (40 000 cts/s, full width at half maximum, FWHM $m/\Delta m$ = 5000 @ m/z = 17.00 (OH^-)), while the imaging mode allows better lateral resolution (<500 nm, 20/80% definition). Count rates and mass resolution are lower in imaging mode (20 000 cts/s, FWHM $m/\Delta m$ = 100 @ m/z = 17 (OH^-)). Depth profiles in spectrometry mode were acquired with Ar_{1500}^+ cluster ions (10 keV, 10 nA, 300 × 300 μm^2) as sputter species and Bi^+ (1.2 pA, 100 × 100 μm^2) as primary ions. Between two sputter frames, analysis was performed after 2 s of pause time, in random raster mode, measuring two frames with 128 × 128 pixels and 1 shot/pixel. For depth profiling of the very surface, less energetic Ar_{1500}^+ (5 keV, 0.5 nA, 300 × 300 μm^2) sputter ions and sputter steps of 5 s were used. The analysis parameters remained the same. For the depth profiles combined with analysis in imaging mode, Ar_{1500}^+ (10 keV, 10 nA, 500 × 500 μm^2) sputter ions and Bi^+ (0.2 pA, 200 × 200 μm^2) primary ions were used. After every sputter frame, analysis was performed with 2 s pause time, in sawtooth raster mode, measuring five frames with 1024 × 1024 pixels and 1 shot/pixel. The cycle time for all measurements was 100 μs. All measurements were carried out in positive- and negative-ion modes to compare the result. Data evaluation was carried out with the software SurfaceLab 7.0 (IONTOF GmbH). For the ToF-SIMS analyses, grounded samples without electron neutralization were measured if not stated differently.

EDX was done using a windowless XMAX EXTREME EDX detector (Oxford Instruments), which is attached to a Merlin high-resolution scanning electron microscope (SEM, Carl Zeiss AG). For sample transfer, an argon-filled Leica EM VCT500 shuttle (Leica Microsystems) was used. The electron acceleration voltage was varied between 1 and 5 kV, while the probing current was kept constant at 1 nA. EDX spectra were measured with a view field of 125 × 100 μm^2, using a resolution of 1024 pixels to scan three frames (pixel dwell time, 100 μs). For each sample and electron beam energy, three measurements at different areas were taken. The software AZtec 4.3 (Oxford Instruments) was used for automatic quantification of the elements Li, C, and O in all spectra. X-ray emission depths were calculated from simulations done with the software casino.[27] The samples were attached to the sample holder using nonconductive double-sided tape if not stated differently.

■ RESULTS AND DISCUSSION

EDX Analysis of Lithium Foil. To quickly obtain initial information on contaminations as well as on the element composition of the passivation layer, the lithium samples were examined nondestructively with EDX. The method was also applied to get qualitative information on the depth distribution of the different elements by varying the SEM electron acceleration voltage. A higher acceleration voltage causes deeper penetration, and X-rays are emitted out of deeper sample

https://dx.doi.org/10.1021/acs.chemmater.0c03518
Chem. Mater. 2021, 33, 859−867

regions. In Figure 1, the development of the elemental composition as a function of the acceleration voltage is shown

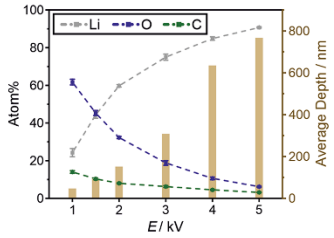

Figure 1. EDX static depth profile: determined atomic fractions of Li, O, and C as a function of the electron acceleration voltage for a sample of lithium foil 2 and calculated (casino) average generation depth of detected Li K_α emission in lithium for the applied voltages.

for lithium foil 2. Since the atomic fraction of Li increases while the O and C fractions decrease with increasing acceleration voltage, the oxygen and carbon content of the lithium foil is higher in the upper region. To get an idea about the probed depths, the average emission depth of the detected Li K_α X-rays was calculated for pure lithium metal (Figure 1) using the freeware casino.[27] As expected, the probed depth is much higher than with surface-sensitive techniques such as XPS and ToF-SIMS.

XPS Depth Profiling of Lithium Foil. With XPS, quantitative element- and compound-specific information is obtained within the detection limit of about 1 atom %. To enable the identification of different compounds with their specific binding energies, it is necessary to measure reference samples. Even though many authors have reported the binding energies for common lithium compounds, it is essential to determine the binding energies for the specific XPS instrument as the values vary due to charging.[28] Figure S1 shows the binding energies of the reference compounds LiOH, Li_2CO_3, Li_2O, and Li_2O_2, as well as of that of lithium metal for our XPS measurements. Depth profiling of the reference compounds was performed to remove the possibly contaminated surface and to evaluate the stability of the compounds against Ar^+ sputtering (S1, S3). Importantly, LiOH and Li_2CO_3 partly decomposed to Li_2O, which needs to be considered for the following interpretation.[29,30]

To complement the EDX results for the lithium samples, we performed XPS depth profiles that provide information about the probed lithium species and their qualitative depth distribution. The XPS spectra obtained for the depth profile of lithium foil 1 are shown in Figure 2a. All observed signals are in accordance with previous reports showing hydroxide and carbonate on an oxide-rich region, which is in contact with lithium metal.[31−33] This observation indicates a passivation bilayer on the lithium foil. A more detailed discussion is given in S2. We emphasize that the composition of the sample is changed to some extent by sputtering (see S3) and that this change must be considered when interpreting the measurement results. As a consequence, conclusions can only be drawn based on a semiquantitative comparison of different samples, as discussed for an example later in this paper. Besides, it is important to note for the interpretation of all lithium spectra that one can exclude a major fraction of lithium metal, if plasmon-loss features are not observed. This is not always taken into account in the literature and will then lead to incorrect conclusions.[34]

The XPS signals for the different species were fitted using area constraints, which were calculated from the relative sensitivity factors (RSF) of the elements and the stoichiometry of the compounds. Binding energy constraints were set with respect to the relative positions of the reference spectra. The profile of the calculated fractions of elements and compounds for lithium foil 1 with increasing depth is shown in Figure 2b,c. It is important to note that the shown sputter steps do not scale linearly with sputter time or even sputter depth, but were chosen to show the qualitative depth distribution of all compounds. Initially, low energy and short time were used to detect changes within the passivation layer, followed by higher energy and longer time to evaluate deeper regions of the sample.

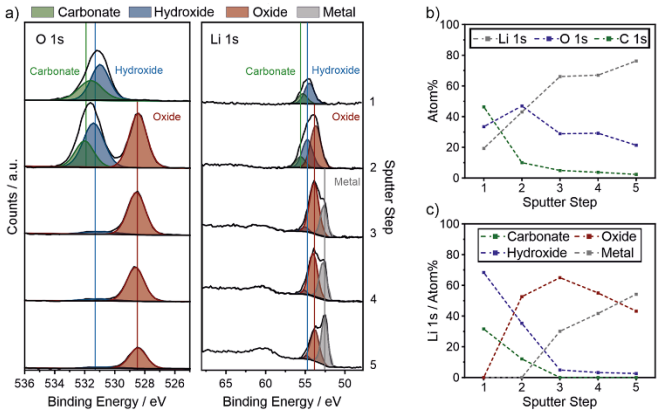

Figure 2. (a) O 1s and Li 1s detail spectra for the XPS depth profile of lithium foil 1 and evolution of atom fractions for (b) elements and (c) lithium compounds calculated from the depth profile. The following parameters were used as sputter steps: (1) surface, (2) 3 min 1 kV, (3) 8 min 2 kV, (4) 12 min 4 kV, (5) 30 min 4 kV.

https://dx.doi.org/10.1021/acs.chemmater.0c03518
Chem. Mater. 2021, 33, 859−867

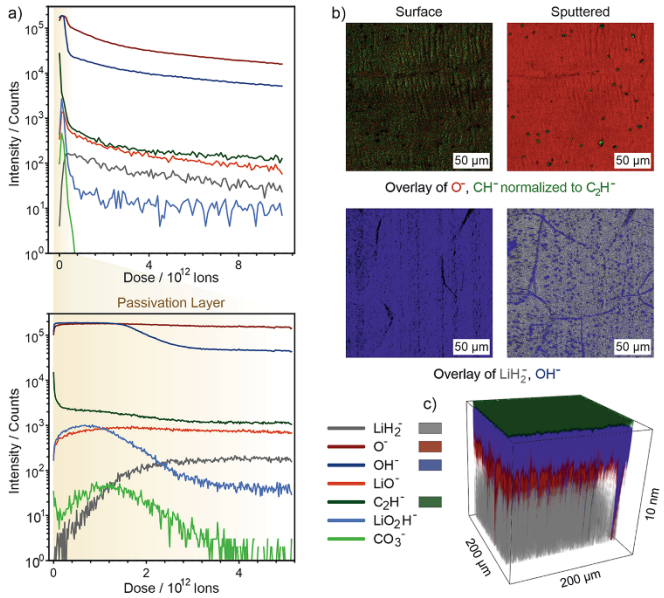

Figure 3. (a) ToF-SIMS depth profiles of as-received lithium foil 1 measured in spectrometry negative-ion mode. As sputter species, argon cluster ions with a size of 1500 atoms and energies of 10 or 5 kV were used to sputter deeper into the sample or to study the passivation layer in detail, respectively. (b) ToF-SIMS overlay images of lithium foil surfaces and the corresponding images after depth profiling, which show contaminations in addition to the passivation layer. (c) 3D reconstruction of a depth profile of lithium foil 1. The depth was calculated assuming a constant sputter rate of 0.50 nm/s.

ToF-SIMS Depth Profiling of Lithium Foil. Although the main elements, compounds, and qualitative depth distribution of the passivation layer on the lithium samples could be identified by XPS depth profiling, the lateral and depth resolutions of XPS analyses are rather low. In addition, the sensitivity toward lithium is low and hydrogen cannot be detected at all. Therefore, we applied ToF-SIMS to take advantage of its higher sensitivity, as well as of its superior lateral and depth resolution to get more information about the three-dimensional distribution of the different compounds. Due to matrix effects, the ToF-SIMS results are only semiquantitative and not inherently compound-specific. Therefore, we also investigated reference samples to identify specific secondary ions (SIs) for the different lithium compounds. The selection of the specific SIs is discussed in S4. Even by using reference spectra, the assignment of the chosen SIs for the interpretation of the depth profiles of lithium foil is not straightforward. An SI may be specific for the compound within the set of reference samples, but not in another chemical environment. Possible sources of error—besides the mentioned matrix effect—are decomposition processes, undefined contaminations, and mass interference. Therefore, all our interpretations are based on combining XPS results with signal developments in the ToF-SIMS depth profiles. In addition, we always considered groups of different SI signals rather than single SIs.

Figure 3a presents the ToF-SIMS depth profiles of a sample of lithium foil 1. The profiles match with the XPS results, showing that the passivation by oxide formation (typical SIs: O^-, LiO^-; Li without further note is ^7Li) reaches deeper than passivation by carbonate (typical SI: CO_3^-) or hydroxide formation (typical SIs: OH^-, LiO_2H^-). This supports the picture of a bilayered passivation structure. LiH was not identified as a component of the passivation film with XPS, but the ToF-SIMS depth profiles show an increased intensity of typical hydride SIs (LiH_2^-) after the first sputter cycles. As discussed above, this is no unequivocal proof for the presence of LiH, but we take it as an indication of its presence. Further evaluation of typical ToF-SIMS signals of lithium compounds will be necessary to answer if LiH is a compound of the passivation layer. This will be part of future work. Interestingly, all signal intensities in the ToF-SIMS depth profiles decrease at high sputter doses. As XPS depth profiling shows increasing amounts of lithium metal with a higher sputter dose, this observation indicates that there are no SIs that are typical for lithium metal (i.e., the ionization probabilities of all SIs are lower in lithium metal than in lithium compounds). This is also the case for lithium cluster ions such as Li_2^- and $^6LiLi^-$ or element ions like $^6Li^-$ and Li^-. Generally, the same information as in the negative-ion mode can be extracted from depth profiles measured for positive polarity (shown in S5). However, the negative-ion mode provides more chemical information as there are less specific and meaningful signals in the positive ToF-SIMS spectra.

From the depth profile shown in Figure 3a, the thickness of the passivation layer was calculated using a sputter rate of 0.50 nm/s (see S6 for discussion of the sputter rates determined from profilometry results). The inflection points of the OH^- and O^- signals were used as indicators for the end of the upper carbonate/hydroxide and oxide passivation layers, respectively. Based on these assumptions, the upper carbonate/hydroxide passivation film is only 2 nm thick. Including the oxide-rich region, the thickness of the complete passivation layer sums up to about 3 nm. In the literature, thicknesses between tens and

https://dx.doi.org/10.1021/acs.chemmater.0c03518
Chem. Mater. 2021, 33, 859−867

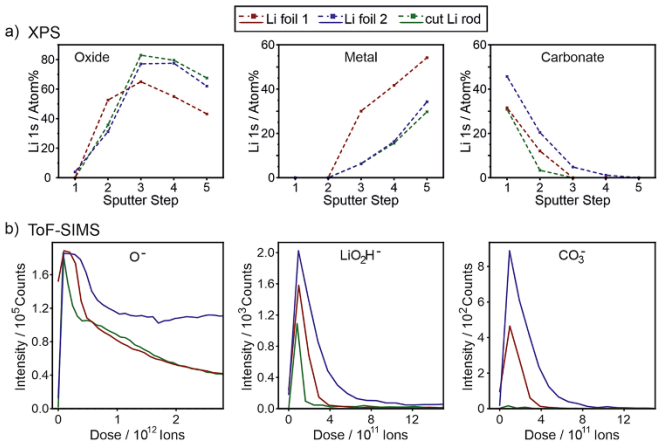

Figure 4. (a) Comparison of the calculated fractions of compounds for the XPS depth profiles of lithium foil 1, lithium foil 2, and sliced lithium rod. (b) ToF-SIMS depth profiles for the same lithium samples measured in spectrometry negative-ion mode. Evolution of the O^-, LiO_2H^-, and CO_3^- signals is presented to compare the thicknesses of the oxide, hydroxide, and carbonate passivation film, respectively.

hundreds of nanometers are reported.[15,16,35] This wide range is surely caused by the different pretreatment and history of the analyzed lithium foils, as well as by the used methods, the experimental design, and the assumptions made for depth calibration. In comparison to the literature, especially the thickness we determined for the oxide-rich region is quite low. Also, regarding the XPS measurements that show no oxide signal before sputtering, common estimations would result at least in a thickness of 6 nm for the upper hydroxide and carbonate passivation layer. This calculation is based on an inelastic mean free path for electrons (λ) of 2 nm[36] and 95% of the detected XPS signal coming from the depth up to 3λ. However, several factors like surface contamination, decreasing signal intensity from growing depth, low XPS sensitivity toward lithium, and the error range of the values taken for the interpretation of XPS and ToF-SIMS measurements influence the results. Therefore, we believe that our ToF-SIMS results give a good representation of the investigated samples and show the passivation film thickness with an error range of few nanometers.

ToF-SIMS Imaging of Lithium Foil. To access lateral information on the passivation layer, we measured depth profiles of the lithium foils in the imaging mode. Figure 3b,c shows the overlay images and a 3D reconstruction, respectively. The raw images are presented in S7. The images show that most areas of the lithium foils were homogeneously covered by a passivation layer with the sequence indicated by the XPS and ToF-SIMS spectrometry depth profiles. In some regions, additional contaminations were detected. The contaminations were enriched in spots or lines, with the latter being most likely grain boundaries. These observations add local contaminants to the simple layered passivation model. We note that the outer sample surface is homogeneously covered with adsorbed hydrocarbons, which have to be removed by sputtering before the contaminations can be detected.

Combined Analyses of Lithium Samples. To find the factors influencing the lithium surface passivation film and how the effects can be investigated best with the used characterization methods, two further samples were investigated. First, a second commercial lithium foil, which was stored longer in a closed plastic box under a glovebox atmosphere ($p(H_2O)/p$ < 0.1 ppm, $p(O_2)/p$ < 0.1 ppm) before analysis (lithium foil 2), was analyzed to find the potential differences between different commercial lithium surfaces and to investigate the influence of storage. Second, a piece of a freshly sliced lithium rod was prepared to analyze a lithium surface without any commercial prepassivation. All of these samples are representatives for lithium anodes, as storage under a glovebox atmosphere and preparation of fresh lithium surfaces are common procedures in battery research. The analyses of the three samples were performed under the exact same experimental conditions to account for sample changes through the analyses themselves. Figure 4a shows the evolution of the atom fractions calculated from XPS depth profiling for all three samples. Qualitatively, the same elements (only Li, C, and O) and compounds were present on all samples. Comparing the two lithium metal foils, the calculated lithium metal fraction was always lower for lithium foil 2. Furthermore, the calculated carbonate fraction was considerably higher for foil 2 and it took more sputter time to remove all carbonate. In addition, the calculated oxide fraction increased more slowly than for lithium foil 1. As lithium foil 2 was kept longer in the glovebox before measurement than lithium foil 1, this observation could either result from different commercial prepassivation of the lithium foils or from storage. To differentiate the two factors, a piece of lithium foil 1 was measured after 2 weeks of storage in a glovebox. As lower lithium metal and higher carbonate factions were observed, we assume that a longer storage time correlates with a thicker passivation layer, which is formed through reaction with residual gases in the glovebox. Consequently, a lower lithium metal fraction and a higher carbonate fraction may be good indicators for a thicker passivation layer, which develops in the glovebox.

The intention of analyzing a freshly sliced lithium sample was to characterize a very thin, initial passivation layer. However, the calculated lithium metal fractions were not higher for the sliced sample. Considering literature reports about freshly prepared lithium surfaces, this observation is not surprising. Lithium

https://dx.doi.org/10.1021/acs.chemmater.0c03518
Chem. Mater. 2021, 33, 859−867

metal is reported to react quickly with traces of contaminations in the glovebox, shuttle modules, and ultrahigh-vacuum (UHV) chambers.[12,18,37] Interestingly, the calculated carbonate fraction for the sliced sample was lower than that for lithium foil 2, while the fraction of lithium metal was similar. This observation indicates that the rapidly formed passivation layer on the freshly sliced sample had a different composition from the passivation layer on the commercial lithium foils. As lithium carbonate is reported to form relatively slowly and out of intermediates, a reduced amount on freshly sliced lithium is reasonable.[24,36]

Exemplary ToF-SIMS depth profiles for the three samples are shown in Figure 4b. All profiles are broadest for lithium foil 2, which indicates that the passivation layer of this sample was thickest. From the shown O^- profile, a passivation layer thickness of 5 nm is estimated. The results are in accordance with the XPS analyses, which also show a qualitatively similar, but thicker passivation layer for lithium foil 2. All ToF-SIMS profiles of the sliced sample are narrower than those of the lithium foils or completely vanished as in the case of CO_3^-. Even though a reduced carbonate contamination fits with the XPS results, a thinner oxide and hydroxide passivation layer is not in accordance. Probably, the differences are attributed to the transport and the atmospheres in the used instruments, since sample preparation and storage were the same. As discussed above, the sliced sample was affected because the freshly prepared surface was highly reactive. The commercially prepassivated lithium foils are not as prone for reaction, which allowed a correlation of the different analyses. In addition, it is important to note that there can always be a small variance in the ToF-SIMS profiles. This is especially true for the lithium samples with a thicker passivation layer as shown in S8 for two different profiles of lithium foil 2 in comparison to one of lithium foil 1. For a quantitative evaluation, these variances need to be considered, but the qualitative conclusions discussed above are not influenced. Investigation of these samples with EDX could not add any information as much more sample volume than the several nanometer thin upper passivation was probed even at low beam energies (Figure 1). EDX may be used for the characterization of thicker passivation layers as discussed in S9.

Lithium Plating through Electron Beam Exposure. XPS depth profiling through Ar^+-sputtering did not end at pure lithium metal for all investigated samples, but always led to a mixture of oxide and metal. Interestingly, electron beam cleaning is reported as a strategy to obtain pure lithium metal.[18] A closer look at the report shows that the term "electron beam cleaning" is misleading. Actually, we assume that the reported treatment rather induces an electrochemically driven mass flow of lithium toward the surface of the sample and does not lead to surface cleaning in the conventional sense. If a lithium sample with an electronically insulating passivation layer is electronically connected to the sample holder, electron beam irradiation causes a potential difference between the sample surface and the grounded sample holder. To compensate the negative charge on the surface, lithium ions migrate through the passivation layer to the surface and recombine with the excess electrons to form lithium metal. The electronically insulating passivation layer plays the same role as the separator electrolyte in a battery, and the effect is comparable to lithium plating. The difference between sputter cleaning and lithium plating is schematically shown in Figure 5. While the passivation layer is removed through sputter cleaning and a deeper region of the lithium sample is then analyzed, fresh lithium metal is plated on top of the passivation film through the electron beam exposure

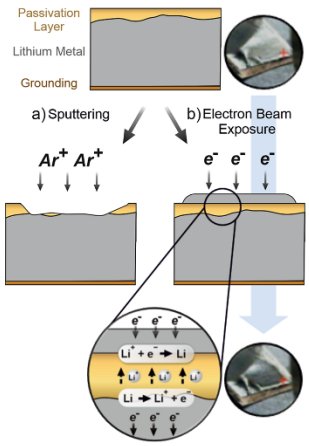

Figure 5. Scheme showing the difference between (a) sputter cleaning and (b) lithium plating through electron beam exposure of electrically contacted samples. XPS camera images show the sample change through lithium plating. The pictures were taken before and after 5 min of lithium plating.

and mimics a cleaned lithium foil. We induced lithium plating in the XPS instrument with the electron neutralizer on lithium foil prepared on copper tape and observed the plated lithium metal in the camera images as darker regions on the sample.

Obviously, the investigation of lithium samples in electrical contact with the grounded holder is not recommended if the electron neutralizer is used during the measurement, as lithium plating will unavoidably take place. The two potentially valid options in the case of XPS are, first, to prepare the lithium foil in electrical contact with the holder and to measure without neutralizer or, second, to isolate the sample from the holder and to use neutralization to create a floating potential. We chose the second option, because the first one bears the risk of undefined sample charging for insulating parts, as described in the literature.[12] Importantly, enforced lithium plating for grounded lithium samples with a passivation layer is a general problem for all measurement techniques with negatively charged probes. The effect is shown for ToF-SIMS measurements with flood gun in S10 and is discussed for EDX in S11. Still, the effect can of course be used for reactivity studies or other targeted studies, as already described in the literature.[38,39] For instance, Wood et al. used lithium plating enforced by the electron gun bias to investigate the SEI formation of a Li/LPS interface with XPS.[39]

Sample Changes under UHV Conditions. Even though lithium plating is unwanted during the investigation of the lithium passivation layer, it can be used to generate clean lithium metal in the XPS chamber. After a few minutes of lithium plating, fractions of about 80% lithium metal were determined, which is far more than after hours of sputter cleaning. Therefore, we used a surface prepared in situ by lithium plating to test the stability of lithium metal in the XPS instrument. Even under UHV conditions of 10^{-9} mbar, full coverage of a sample surface with a monolayer of adsorbate is reached within approximately 1000 s (assuming an adhesion coefficient of 1). Consequently, sample changes in the analysis instruments play an important role for the interpretation of the results and must be considered. The surface changes of lithium samples in the used XPS instrument

https://dx.doi.org/10.1021/acs.chemmater.0c03518
Chem. Mater. 2021, 33, 859−867

are presented in Figure 6. Within 2 h, the calculated fraction of metal in the Li 1s region drops from 81 to 57%. At the same time,

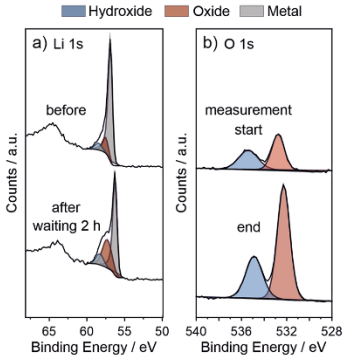

Figure 6. (a) Li 1s spectrum of plated lithium before and after 2 h of waiting time in the XPS instrument. (b) O 1s detail spectra taken at the start and end of one measurement cycle (XPS depth profile, sliced lithium rod). The intensity of the hydroxide and oxide peaks increases and the ratio shifts toward a higher lithium oxide fraction.

the calculated oxide fraction increases from 13 to 33% and the hydroxide fraction increases from 6 to 10%. Consequently, lithium metal reacted to oxide and hydroxide in the XPS chamber. Having in mind that measuring survey and detail spectra for the Li, C, and O 1s regions in the presented quality takes about 1 h, significant changes during measurement are expected, as also shown in Figure 6b. This demonstrates that a reliable comparison between analyses of different samples is only possible if the analyses are run under precisely the same experimental conditions regarding chamber atmosphere and measurement sequence. Even though unwanted reactions of the samples with the chamber atmosphere influence the quantitative results, qualitative relations and comparisons are valid in this case. This issue plays a non-negligible role for all (U)HV characterization techniques and was considered for all analyses discussed in this study.

■ CONCLUSIONS

In this study, we use EDX, XPS, and TOF-SIMS to characterize the passivation layer on various lithium samples. We show that the passivation film of lithium samples is mainly homogeneous with additional local organic and inorganic contaminants. Our measurements indicate a bilayered structure, which is composed of a layer of hydroxide and carbonate on top of an oxide-rich region, which is in contact with lithium metal. The layers are only a few nanometers thick in the case of the investigated lithium foils. Through analysis of lithium samples with different preparation and storage histories, we found that the thickness and composition of the surface passivation layer depend on preparation, storage, and transport of the samples. It is shown that storage in a glovebox cannot fully prevent sample changes through reaction and already 2 weeks of storage may cause a thicker layer and sample inhomogeneity. Besides, even transport from the glovebox to the analysis instruments under glovebox atmosphere can lead to rapid passivation of highly reactive samples like freshly sliced lithium, while commercially prepassivated lithium foils are less affected.

In addition to these results, we demonstrate the potentials and limits of EDX, XPS, and ToF-SIMS as analytical techniques for the characterization of the passivation layer on lithium samples. It is shown that a multianalytical approach is required for a comprehensive and reliable characterization of the passivation film. While XPS depth profiling provides important information about the quantitative composition and sequence of the passivation compounds, ToF-SIMS analyses add information about the passivation thickness, the sample homogeneity, and the lateral distribution of the compounds. The combined analysis gives a complete three-dimensional chemical picture of the lithium metal surfaces. Complementary, EDX measurements may provide information about thicker passivated layers and bulk contaminations.

Also, we show that the design of the measurements has a strong impact on the obtained results and can lead to unreliable data and serious misinterpretations. Importantly, we show that lithium plating occurs upon electron beam exposure of electrically contacted lithium samples, with the native passivation layer acting as a solid electrolyte. We demonstrated that surface reactions of lithium with the residual gas need to be considered even under UHV conditions, as significant changes occur within standard measurement periods. Together with the discussed decomposition of lithium compounds by argon sputtering, this observation shows that only measurements performed under exactly the same conditions are comparable. Concerning data evaluation, it is proposed that a reliable XPS fit model for compound quantification should include relative position constraints that are determined from reference samples and area constraints based on a valid physicochemical model. For the interpretation of ToF-SIMS data, it is most important to critically evaluate secondary ions that are considered as specific fragments of compounds with regard to matrix effects. Complementary XPS analyses are needed for a reliable interpretation. Overall, our work provides a guideline for robust characterization procedures that can be used to obtain reliable information on the surface composition and chemistry of lithium samples.

■ ASSOCIATED CONTENT

Supporting Information

The Supporting Information is available free of charge at https://pubs.acs.org/doi/10.1021/acs.chemmater.0c03518.

Characterization of reference samples with XPS, XPS depth profiles, decomposition by argon sputtering, characterization of reference samples with ToF-SIMS, ToF-SIMS depth profiling, determination of sputter rates with ToF-SIMS, ToF-SIMS imaging, variation in ToF-SIMS depth profiles, EDX analysis of lithium samples with thicker passivation layers, lithium plating through ToF-SIMS measurements, and lithium plating through EDX measurements (PDF)

■ AUTHOR INFORMATION

Corresponding Author

Anja Henss − *Institute of Physical Chemistry, Justus Liebig University Giessen, D-35392 Giessen, Germany; Center for Materials Research (LaMa), Justus Liebig University Giessen, D-35392 Giessen, Germany;* orcid.org/0000-0001-5009-6512; Email: anja.henss@phys.chemie.uni-giessen.de

https://dx.doi.org/10.1021/acs.chemmater.0c03518
Chem. Mater. 2021, 33, 859−867

Authors

Svenja-K. Otto − *Institute of Physical Chemistry, Justus Liebig University Giessen, D-35392 Giessen, Germany*

Yannik Moryson − *Institute of Physical Chemistry, Justus Liebig University Giessen, D-35392 Giessen, Germany*

Thorben Krauskopf − *Institute of Physical Chemistry, Justus Liebig University Giessen, D-35392 Giessen, Germany*

Klaus Peppler − *Institute of Physical Chemistry, Justus Liebig University Giessen, D-35392 Giessen, Germany*

Joachim Sann − *Institute of Physical Chemistry, Justus Liebig University Giessen, D-35392 Giessen, Germany*

Jürgen Janek − *Institute of Physical Chemistry, Justus Liebig University Giessen, D-35392 Giessen, Germany; Center for Materials Research (LaMa), Justus Liebig University Giessen, D-35392 Giessen, Germany;* orcid.org/0000-0002-9221-4756

Complete contact information is available at: https://pubs.acs.org/10.1021/acs.chemmater.0c03518

Notes

The authors declare no competing financial interest.

■ ACKNOWLEDGMENTS

The authors acknowledge the financial support by the BMBF (Bundesministerium für Bildung und Forschung) within the FestBatt−Cluster of Competence for Solid-state Batteries (03XP0176D), the MaLiBa (03XP0185D), and the ProLiFest (03XP0253B) projects. T.K. and S.-K.O. acknowledge the financial support (Kékulé scholarship) by the Funds of the Chemical Industry (FCI). The authors thank Felix Walther and Sven Kayser for the very helpful discussions about data interpretation.

■ REFERENCES

(1) Janek, J.; Zeier, W. G. A solid future for battery development. *Nat. Energy* **2016**, *1*, No. 1167.

(2) Zheng, J.; Kim, M. S.; Tu, Z.; Choudhury, S.; Tang, T.; Archer, L. A. Regulating electrodeposition morphology of lithium: towards commercially relevant secondary Li metal batteries. *Chem. Soc. Rev.* **2020**, *49*, 2701−2750.

(3) Schmuch, R.; Wagner, R.; Hörpel, G.; Placke, T.; Winter, M. Performance and cost of materials for lithium-based rechargeable automotive batteries. *Nat. Energy* **2018**, *3*, 267−278.

(4) Liand, X.; Pang, Q.; Kochetkov, I. R.; Sampere, M. S.; Huang, H.; Sun, X.; Nazar, L. F. A facile surface chemistry route to a stabilized lithium metal anode. *Nat. Energy* **2017**, *2*, 1−7.

(5) Ahn, J.; Park, J.; Kim, J. Y.; Yoon, S.; Lee, Y. M.; Hong, S.; Lee, Y.-G.; Phatak, C.; Cho, K. Y. Insights into Lithium surface: Stable Cycling by Controlled 10-μm-deep Surface Relief, Reinterpreting the Natural Surface Defect on Lithium Metal Anode. *ACS Appl. Energy Mater.* **2019**, *2*, 5656−5664.

(6) Cheng, X.-B.; Zhang, R.; Zhao, C.-Z.; Zhang, Q. Toward Safe Lithium Metal Anode in Rechargeable Batteries: A Review. *Chem. Rev.* **2017**, *117*, 10403−10473.

(7) Lin, D.; Liu, Y.; Cui, Y. Reviving the lithium metal anode for high-energy batteries. *Nat. Nanotechnol.* **2017**, *12*, 194−206.

(8) Zheng, H.; Wu, S.; Tian, R.; Xu, Z.; Zhu, H.; Duan, H.; Liu, H. Intrinsic Lithiophilicity of Li−Garnet Electrolytes Enabling High-Rate Lithium Cycling. *Adv. Funct. Mater.* **2020**, *30*, No. 1906189.

(9) Zhou, H.; Yu, S.; Liu, H.; Liu, P. Protective coatings for lithium metal anodes: Recent progress and future perspectives. *J. Power Sources* **2020**, *450*, No. 227632.

(10) Ryou, M.-H.; Lee, Y. M.; Lee, Y.; Winter, M.; Bieker, P. Mechanical Surface Modification of Lithium Metal: Towards Improved Li Metal Anode Performance by Directed Li Plating. *Adv. Funct. Mater.* **2015**, *25*, 834−841.

(11) David, D. J.; Froning, M. H.; Wittberg, T. N.; Moddeman, W. E. Surface reactions of lithium with the environment. *Appl. Surf. Sci.* **1981**, *7*, 185−195.

(12) Fujieda, T. Surface of lithium electrodes prepared in Ar + CO2 gas. *J. Power Sources* **1994**, *52*, 197−200.

(13) Schily, U.; Heitbaum, J. Surface analysis of freshly cut Li samples: Na-segregation and film forming reaction by O2, SO2, and liquid LiAlCl4 · 3(SO2). *Electrochim. Acta* **1992**, *37*, 731−738.

(14) Kanamura, K.; Tamura, H.; Shiraishi, S.; Takehara, Z.-i. Morphology and chemical compositions of surface films of lithium deposited on a Ni substrate in nonaqueous electrolytes. *J. Electroanal. Chem.* **1995**, *394*, 49−62.

(15) Kanamura, K. XPS Analysis of Lithium Surfaces Following Immersion in Various Solvents Containing LiBF4. *J. Electrochem. Soc.* **1995**, *142*, No. 340.

(16) Naudin, C.; Bruneel, J. L.; Chami, M.; Desbat, B.; Grondin, J.; Lassègues, J. C.; Servant, L. Characterization of the lithium surface by infrared and Raman spectroscopies. *J. Power Sources* **2003**, *124*, 518−525.

(17) Ismail, I.; Noda, A.; Nishimoto, A.; Watanabe, M. XPS study of lithium surface after contact with lithium-salt doped polymer electrolytes. *Electrochim. Acta* **2001**, *46*, 1595−1603.

(18) Kamphaus, E. P.; Angarita-Gomez, S.; Qin, X.; Shao, M.; Engelhard, M. H.; Mueller, K. T.; Murugesan, V.; Balbuena, P. B. Role of inorganic surface layer on solid electrolyte interphase evolution at Li-metal anodes. *ACS Appl. Mater. Interfaces* **2019**, *11*, 31467−31476.

(19) Harry, K. J.; Hallinan, D. T.; Parkinson, D. Y.; MacDowell, A. A.; Balsara, N. P. Detection of subsurface structures underneath dendrites formed on cycled lithium metal electrodes. *Nat. Mater.* **2014**, *13*, 69.

(20) Maslyn, J. A.; Frenck, L.; Loo, W. S.; Parkinson, D. Y.; Balsara, N. P. Extended Cycling through Rigid Block Copolymer Electrolytes Enabled by Reducing Impurities in Lithium Metal Electrodes. *ACS Appl. Energy Mater.* **2019**, *2*, 8197−8206.

(21) Meyerson, M. L.; Sheavly, J. K.; Dolocan, A.; Griffin, M. P.; Pandit, A. H.; Rodriguez, R.; Stephens, R. M.; Vanden Bout, D. A.; Heller, A.; Mullins, C. B. The effect of local lithium surface chemistry and topography on solid electrolyte interphase composition and dendrite nucleation. *J. Mater. Chem. A* **2019**, *7*, No. 513.

(22) Becking, J.; Gröbmeyer, A.; Kolek, M.; Rodehorst, U.; Schulze, S.; Winter, M.; Bieker, P.; Stan, M. C. Lithium-Metal Foil Surface Modification: An Effective Method to Improve the Cycling Performance of Lithium-Metal Batteries. *Adv. Mater. Interfaces* **2017**, *4*, No. 1700166.

(23) Harilal, S. S.; Allain, J. P.; Hassanein, A.; Hendricks, M. R.; Nieto-Perez, M. Reactivity of lithium exposed graphite surface. *Appl. Surf. Sci.* **2009**, *255*, 8539−8543.

(24) Hart, C. A.; Skinner, C. H.; Capece, A. M.; Koel, B. E. Sorption of atmospheric gases by bulk lithium metal. *J. Nucl. Mater.* **2016**, *468*, 71−77.

(25) Jeppson, D. W. *Lithium Literature Review: Lithium's Properties and Interactions*; Hanford Engineering Development Laboratory, 1978; pp 1−80.

(26) Rhein, R. A. *Lithium Combustion: A Review*; Ordance Systmens Department, Naval Weapons Center, 1990; pp 1−60.

(27) Drouin, D.; Couture, A. R.; Joly, D.; Tastet, X.; Aimez, V.; Gauvin, R. CASINO V2.42: a fast and easy-to-use modeling tool for scanning electron microscopy and microanalysis users. *Scanning* **2007**, *29*, 92−101.

(28) Wood, K. N.; Teeter, G. XPS on Li-Battery-Related Compounds: Analysis of Inorganic SEI Phases and a Methodology for Charge Correction. *ACS Appl. Energy Mater.* **2018**, *1*, 4493−4504.

(29) Edström, K.; Herstedt, M.; Abraham, D. P. A new look at the solid electrolyte interphase on graphite anodes in Li-ion batteries. *J. Power Sources* **2006**, *153*, 380−384.

(30) Dedryvère, R.; Laruelle, S.; Grugeon, S.; Poizot, P.; Gonbeau, D.; Tarascon, J.-M. Contribution of X-ray Photoelectron Spectroscopy to

the Study of the Electrochemical Reactivity of CoO toward Lithium. *Chem. Mater.* **2004**, *16*, 1056−1061.
(31) Kanamura, K.; Tamura, H.; Takehara, Z.-i. XPS analysis of a lithium surface immersed in propylene carbonate solution containing various salts. *J. Electroanal. Chem.* **1992**, 333, 127−142.
(32) Kanamura, K.; Tamura, H.; Shiraishi, S.; Takehara, Z.-i. XPS Analysis for Lithium Surface Immersed in Tetrahydrofuran Containing Various Salts. *Denki Kagaku oyobi Kogyo Butsuri Kagaku* **1993**, *61*, 1377−1382.
(33) Kanamura, K. X-Ray Photoelectron Spectroscopic Analysis and Scanning Electron Microscopic Observation of the Lithium Surface Immersed in Nonaqueous Solvents. *J. Electrochem. Soc.* **1994**, *141*, No. 2379.
(34) Tang, W.; Yin, X.; Chen, Z.; Fu, W.; Loh, K. P.; Zheng, G. W. Chemically polished lithium metal anode for high energy lithium metal batteries. *Energy Storage Mater.* **2018**, *14*, 289−296.
(35) Yen, S. P. S. Chemical and Morphological Characteristics of Lithium Electrode Surfaces. *J. Electrochem. Soc.* **1981**, *128*, No. 1434.
(36) Etxebarria, A.; Yun, D.-J.; Blum, M.; Ye, Y.; Sun, M.; Lee, K.-J.; Su, H.; Muñoz-Márquez, M. A.; Ross, P. N.; Crumlin, E. J. Revealing in situ Li metal anode surface evolution upon exposure to CO2 using Ambient Pressure X-ray Photoelectron Spectroscopy. *ACS Appl. Mater. Interfaces* **2020**, *12*, 26607−26613.
(37) Li, Y.; Li, Y.; Sun, Y.; Butz, B.; Yan, K.; Koh, A. L.; Zhao, J.; Pei, A.; Cui, Y. Revealing Nanoscale Passivation and Corrosion Mechanisms of Reactive Battery Materials in Gas Environments. *Nano Lett.* **2017**, *17*, 5171−5178.
(38) He, Y.; Ren, X.; Xu, Y.; Engelhard, M. H.; Li, X.; Xiao, J.; Liu, J.; Zhang, J.-G.; Xu, W.; Wang, C. Origin of lithium whisker formation and growth under stress. *Nat. Nanotechnol.* **2019**, *14*, 1042−1047.
(39) Wood, K. N.; Steirer, K. X.; Hafner, S. E.; Ban, C.; Santhanagopalan, S.; Lee, S.-H.; Teeter, G. Operando X-ray photoelectron spectroscopy of solid electrolyte interphase formation and evolution in Li2S-P2S5 solid-state electrolytes. *Nat. Commun.* **2018**, *9*, No. 2490.

https://dx.doi.org/10.1021/acs.chemmater.0c03518
Chem. Mater. 2021, 33, 859−867

3.3 Publication 3 “Protective Coating for the Lithium Metal Anode Prepared by Plasma Polymerization”

In publication 3 of this doctoral thesis a passivation layer by plasma polymerization was deposited on LMAs and combined with plasma cleaning. The plasma layers were characterized by ToF-SIMS, XPS and SEM, as well as the mechanical properties were examined by nanoindentation. Additionally, ^{18}O diffusion experiments were conducted to test the protective nature of the coating against oxygen and symmetric cell tests were performed.

First of all, the results showed that Ar plasma cleaning is a good method to remove the native passivation layer of lithium metal foils but also that a re-passivation with thinner passivation layers takes almost place immediately. With 1.4-bis(trifluoromethyl)benzene as precursors pore free and dense polymer layers with a thickness of about 1 µm could be deposited onto the lithium metal foil. The polymer layers showed similarities to commercially available Parylene HT® layers with additional crosslinking. The ToF-SIMS depth profiles showed that no Li is present on the surface and that the polymer layer consists of three sublayers. By nanoindentation the Young’s modulus and hardness of the polymer films could be determined on non-air sensitive samples and showed values of about 4.6 GPa and 0.16 GPa which are in the typical range for polymers.

To see the impact of the plasma layer on cell performance, symmetric Li cells with liquid electrolyte were cycled and the overpotentials and impedance were measured. At first wettability tests were performed with the liquid electrolyte and showed that the wettability of coated LMAs is better than the wettability of uncoated ones but also that the polymer layers soak up the electrolyte. This has a direct influence of the cycling behavior as the experiments showed that more electrolyte is needed to avoid cell dry out. The soaking up of the electrolyte gives also a lot of different pretreatment options for the used polymers layers e.g. the layers can be treated with Li containing solutions to enhance the lithium ion conductivity. The cell tests showed that the coated symmetric cells performed much better than the uncoated ones with low overpotentials at current densities between 0.1 and 1.0 mA/cm^2. Even though, the resistance of the polymer layer is at the beginning about twice as high as for a pristine cell, the resistance is continuously decreasing during the cycling process due to increasing lithium ion conductivity.

The ^{18}O diffusion experiments revealed that the diffusion coefficient in the plasma layer is about 4 orders of magnitude greater than in the native passivation layer but the combination of thickness and diffusion coefficient is still sufficient to protect the lithium against oxygen for at least 30 minutes, which is enough for normal cell preparation works e.g. in glovebox or dry room.

Overall the second publication shows that the plasma polymerization is a suitable method to apply protective coatings on LMAs. Especially, the possible combination of a cleaning

step and deposition step in one setup is very promising. The dwelling of the polymer layers can be a great chance for different pretreatment methods to further optimize their properties.

The first author designed and planned the experiments for this publication under the supervision of M. Rohnke and J. Janek. H. Hartmann helped with the preparation of coated LMAs and with cell building. The first author performed the XPS and ToF-SIMS measurements and was supported by H. Hartmann. S-K. Otto supported the ToF-SIMS analyses. The nanoindentation measurements were conducted together with X. Fang, who analyzed the data. The manuscript was written by the first author und edited by the co-authors.

ACS APPLIED ENERGY MATERIALS

www.acsaem.org Article

Protective Coating for the Lithium Metal Anode Prepared by Plasma Polymerization

Yannik Moryson, Hannah Hartmann, Svenja-Katharina Otto, Xufei Fang, Marcus Rohnke,* and Jürgen Janek*

Cite This: https://doi.org/10.1021/acsaem.3c00681 Read Online

ACCESS | Metrics & More | Article Recommendations | Supporting Information

ABSTRACT: The demand for batteries with higher energy densities for energy storage and electric vehicles motivates research for a stable and reversible lithium metal anode. The native passivation layer on commercial lithium foils does not enable stable cycling in liquid electrolytes due to inhomogeneities in the layer composition and impurities. These inhomogeneities and impurities result in locally varying current densities, which often lead to dendrite growth and ultimately cell failure. Artificial protection layers are one promising option to overcome these issues and enable the reversible operation of lithium metal anodes. In this study, we used plasma polymerization of 1.4 bis(trifluoromethyl)-benzene to form an artificial passivation layer on top of plasma-cleaned lithium metal. The layer was characterized with time-of-flight secondary ion mass spectrometry, X-ray photoelectron spectroscopy, and scanning electron microscopy. The mechanical properties of the layer were examined by nanoindentation. Symmetric cell tests showed stable cycling behavior for over 300 h, with overpotentials below 0.1 V at current densities between 0.1 and 1 mA/cm^2. $^{18}O_2$ isotope exchange experiments were used to get an estimation of the diffusion coefficients of oxygen in the native passivation layer of lithium foils at room temperature and for oxygen in the plasma polymer at room temperature. The combination of layer thickness and diffusion coefficient of the plasma polymer is sufficient to protect the lithium metal against oxygen for at least 30 min, which makes it a suitable protective coating.

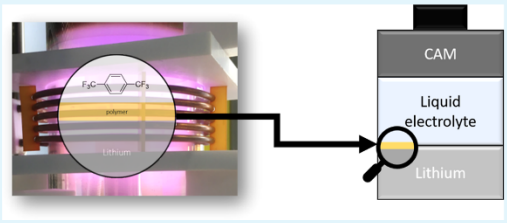

KEYWORDS: *lithium metal anode, diffusion coefficient, Young's modulus, protection layer, artificial SEI, plasma polymerization*

INTRODUCTION

The need for higher energy densities of batteries for energy storage and electric vehicles is the driving force behind the increasing effort to construct batteries with a well working lithium metal anode (LMA), despite all the challenges—such as the very high reactivity of lithium and dendrite growth.[1,2] Enabling the use of the LMA would offer an up to 10 times higher specific capacity in comparison to a graphite anode, which is used in state-of-the-art commercial lithium-ion batteries (LIBs).[3] Due to the high reactivity of lithium, the Coulomb efficiency and cycle life of batteries with an LMA are poor and yet not competitive with state-of-the-art LIBs. The native passivation layer on top of lithium is insufficient for the formation of a stable solid−electrolyte interface (SEI) due to its inhomogeneity and impurities, which result in nonuniform current densities during battery cycling and ultimately dendrite growth.[4,5] To overcome these drawbacks, one promising option is a suitable pretreatment of the LMA surface. The pretreatment could result, for example, in a coating with a thin but stable protection layer (artificial SEI, ASEI) to prevent the uncontrolled reaction between lithium and the electrolyte and to ensure a homogeneous current density across the whole surface.[6−11] An ideal ASEI should be rigid enough to prevent dendrite growth but also flexible enough to not break during cycling due to volume changes of the anode. In addition, the ASEI has to be electronically insulating but well lithium-ion-conducting and ideally allow handling at air for a short time without oxidation.

Protection layers can be classified into inorganic-based and polymer-based or a combination of both. While inorganic compounds are often chemically stable against lithium, their low elasticity leads to cracking due to the significant volume changes of the anode during cycling.[12] Polymers are flexible enough to tolerate the volume changes but also often too soft to prevent dendrite formation during long-term cycling. Furthermore, polymers may also react with lithium, which is not necessarily a drawback as stable inorganic compounds like LiF may form that show sufficient lithium ion mobility in a nanostructured form.[12,13]

Received: March 17, 2023
Accepted: May 24, 2023

https://doi.org/10.1021/acsaem.3c00681
ACS Appl. Energy Mater. XXXX, XXX, XXX−XXX

One possible route to deposit a polymer on top of lithium metal and also, if necessary, to remove the native passivation layer in one single setup is the combination of plasma sputtering and plasma polymerization. Plasma polymerization is mainly used in biomaterials engineering, and Takehara et al. used this technique already in the 1990s to deposit 1,1-difluoroethene films on cleaned lithium foils.[14−16] To the best of our knowledge, this is so far the only example for the use of plasma polymerization to create protection layers for lithium metal anodes. The produced films were pinhole-free and about 0.6 μm thick. In comparison to uncoated lithium anodes, the lithium deposition on the coated anodes during cell cycling was improved to smooth lithium structures instead of needle-like lithium on the uncoated ones. In essence, plasma polymerization appears not only promising but also complex due to the huge number of potential precursors in combination with various pretreatments before deposition. Not in the least, plasma reactors operate under vacuum conditions, and costs of plasma processing need to be considered.

In this work, we used a self-constructed inductively coupled radio frequency (rf) plasma reactor (see Supporting Information S1) to remove in a first step the native passivation layer on top of lithium foil with an argon plasma and deposit in a second step a polymer layer from a 1.4 bis(trifluoromethyl)-benzene precursor on the cleaned lithium surface. Especially the combination of a cleaning and coating step in one setup and the large number of possible precursor and gas combinations make plasma polymerization a promising coating technique. 1.4 Bis(trifluoromethyl)benzene was chosen as a precursor due to its high fluorine content and its structure that is close to parylene building units. Parylenes are polymers consisting of *p*-xylylene and halogenated derivates, which are often used as coating materials due to their protective properties against gases and water.[17] Additionally, the fluorine content in the precursor is beneficial for the potential formation of nanosized LiF, which has a lithium ion conductivity between 10^{-7} and 10^{-13} S/cm that may be sufficient in case of very thin layers.[12,13,29] Recently, parylene coatings are increasingly tested as a functional coating in different fields of application.[18−21] The coating produced in this work was characterized by X-ray photoelectron spectroscopy (XPS) with respect to its chemical composition. The layer was also examined by time-of-flight secondary ion mass spectrometry (ToF-SIMS) depth profiling, and the morphology of the layer was imaged with scanning electron microscopy (SEM). The mechanical properties, such as Young's modulus and hardness, were determined by nanoindentation. Additionally, the coated lithium foils were exposed to $^{18}O_2$ atmosphere and afterward examined by ToF-SIMS to determine the oxygen diffusion coefficient, which is correlated with the protective effect of the coating. The wetting properties of the coating were tested with a liquid electrolyte composed of LiTFSI/$LiNO_3$ in DOL (dioxolane)/DME (dimethoxyethane), which is a common electrolyte in lithium sulfur cells, and symmetrical cells were built and cycled in comparison with uncoated pristine LMA.

EXPERIMENTAL SECTION

Plasma Chamber. The argon plasma cleaning, plasma polymerization, and $^{18}O_2$ experiments were all performed in a self-constructed inductively coupled rf-plasma reactor, see Supporting Information S1 and a previous report.[22] For sample cleaning, an argon plasma (Argon, 99.999%, Nippon Gas GmbH, Germany) and for plasma polymerization 1.4 bis(trifluoromethyl)benzene (98%, Sigma-Aldrich GmbH, Germany) were used. A copper coil around the plasma chamber was powered by a rf generator (PFG RF 300, Trumpf Hüttinger, Germany) in combination with a matching network system (PFM 1500 A, Trumpf Hüttinger, Germany), operating at 13.56 MHz. Plasma cleaning was executed for 5 min with 100 W power and an argon pressure of p(Ar) = 1 mbar (gas flow = 15.5 sccm). For plasma polymerization, the lithium foils were exposed to a pure 1.4 bis(trifluoromethyl)benzene plasma at P = 50 W and 1 mbar for 1 min. For $^{18}O_2$ experiments, the plasma chamber and plasma transfer module were filled with $^{18}O_2$ (99%, Sigma-Aldrich GmbH, Germany) at p = 10 mbar and kept at room temperature. After 30 min, the transfer module was pumped, and the sample was cooled down with liquid nitrogen inside the Leica EM VCT500 (Leica GmbH, Wetzlar, Germany) transfer system to −70 °C within 2 min. The sample transfer into a ToF-SIMS M6 (IONTOF company, Münster, Germany) was carried out with the Leica EM VCT500 transfer system, which was cooled with liquid nitrogen all the time. All analytical measurements were performed on multiple samples, and representative results are shown here.

Scanning Electron Microscopy/Energy-Dispersive X-ray Spectroscopy. Images of the surface morphology were acquired in a high-resolution SEM (Merlin Zeiss, Germany). Imaging was carried out with the in-lens and SE2 secondary electron detectors at an accelerating voltage of 3 kV. The homogeneity of the coating regarding the local element distribution was examined by energy-dispersive X-ray spectroscopy (EDX) (Oxford Instruments, UK) with an X-Max Extreme detector at an accelerating voltage of 3 kV. The samples were transferred into the SEM with the Leica EM VCT500 shuttle box under inert gas conditions. The samples were attached with isolating adhesive tesa tape on Leica stubs to minimize Li plating during SEM measurements.

X-ray Photoelectron Spectroscopy. XPS measurements were carried out with a PHI VersaProbe II instrument (Physical Electronics GmbH, Germany) to get additional quantitative information about the composition of the coating layers. The coated Li foils were fixed with electrically isolating adhesive tesa tape and transferred in an airtight transfer vessel under an argon atmosphere. Charge neutralization was carried out with the low-energy electron and ion guns. Monochromatic Al Kα radiation was used for analysis (1486.6 eV). The power of the X-ray source was 100 W and the beam voltage was 20 kV (high power mode). The examined area was 0.13 mm^2. For the survey spectra, a pass energy of 93.5 eV was applied, and for the detail spectra, a pass energy of 23.5 eV was applied. The pressure during analysis was in the range of 5×10^{-7} Pa. For data evaluation, the software CasaXPS (version 2.3.18, Casa Software Ltd) was used. All data were calibrated in relation to the signal of adventitious carbon at 284.8 eV. A Shirley-type background and Gauss-Lorentz [GL (30)] line shapes were applied for data evaluation.

Time-of-Flight Secondary Ion Mass Spectrometry. ToF-SIMS depth profiles on plasma cleaned and pristine lithium foils were performed using a TOF.SIMS 5 instrument (IONTOF GmbH, Germany) equipped with a 25 keV Bi cluster primary-ion gun for analysis and a 20 kV Ar gas cluster ion beam (GCIB), as well as a 2 kV DSC (Cs^+) for sputtering. The samples were attached with tesa tape on a Leica transfer stub in the glovebox. The sample transfer was carried out with the Leica EM VCT500 (Leica GmbH, Germany) transfer system. As primary ions, Bi^+ (25 keV, 100 × 100 μm^2, 128 × 128 pixels, sawtooth mode) and as sputter species Ar_{1500}^+ clusters (10 keV, 300 × 300 μm^2) were used. For depth profiling on polymer-coated samples, Bi_3^+ (25 keV, 100 × 100 μm^2, 128 × 128-pixels, random mode) and Cs^+ (2 kV, 300 × 300 μm^2) were used to achieve faster erosion. The low-energetic electron flood gun was applied for charge compensation.

ToF-SIMS depth profiling after $^{18}O_2$ exposure was performed on a liquid nitrogen-cooled sample holder at −145 °C in a M6 Hybrid SIMS instrument (IONTOF GmbH, Germany) equipped with a 30 keV Bi cluster primary-ion gun at a main chamber pressure of 1.3×10^{-9} mbar. The samples were attached with Cu-tape on a Leica transfer stub in the glovebox. The sample transfer was carried out with

https://doi.org/10.1021/acsaem.3c00681
ACS Appl. Energy Mater. XXXX, XXX, XXX−XXX

the Leica EM VCT500 (Leica GmbH, Germany) transfer system. As primary ions, Bi_3^{2+} clusters (60 keV, 100 × 100 μm^2, 128 × 128 pixels) and for sputtering Cs^+ (2 kV, 250 × 250 μm^2 for coated samples and 1 kV, 250 × 250 μm^2 for pristine lithium foil) were used. All ToF-SIMS measurements were carried out in negative ion mode. The electron flood gun was used for charge compensation. The data evaluation was carried out with the software SurfaceLab 7.2 (IONTOF GmbH, Germany).

Nanoindentation. A commercial diamond Berkovich indenter (Synton-MDP, Switzerland) was used on a G200 nanoindenter (Keysight Technologies, USA) for the nanoindentation tests. The continuous stiffness measurement (CSM) method was used to achieve a continuous monitoring of the hardness and Young's modulus during the indentation process, with a maximum depth of up to 300 nm. The depth was chosen to avoid a possible interference of the substrate due to a limited film thickness. A strain rate of 0.05 s^{-1} was used, with a data acquisition rate of 15 Hz. 16 indents were performed for the same experimental condition to capture the reproducibility; the minimum spacing between the nearest 2 indents was 40 μm to ensure no overlapping of the possible deformation zone. Polymers on steel and silicon wafers were tested since the nanoindentation could not be performed inside an argon glovebox.

Electrochemical Characterization. Bare lithium metal anodes (punched out of lithium foil, Honjo Metal Co., Ltd., Japan, >99.0 wt %, thickness 30 μm, diameter 13 mm) and coated lithium metal anodes were assembled in an argon-filled glovebox into type CR2016 coin cells (Xiamen Tmax Battery Equipments Limited, China) with two polymer separators [Celgard LLC (25 μm), USA]. As electrolyte, a 1:1 solution of dimethoxyethane (DME, Sigma-Aldrich GmbH, Germany) and dioxolane (DOL, Sigma-Aldrich GmbH, Germany) was mixed with 1:1 2.0 M LiTFSI (99.95%, Sigma-Aldrich GmbH, Germany) and 0.5 M $LiNO_3$ (99.0%, Sigma-Aldrich GmbH, Germany) to achieve a 1 M LiTFSI and 0.25 M $LiNO_3$ solution in DOL/DME. DOL and DME had been stored over 3 Å molecular sieves to achieve H_2O contents of less than 0.4 and 1.2 ppm, respectively. The cells were fully wetted with 50 or 150 μL electrolyte, respectively. Cell testing was performed with a VMP-300 potentiostat (BioLogic, France) using current densities from 0.1 up to 1 mA/cm^2. Potentiostatic electrochemical impedance spectroscopy (PEIS) was performed at OCV using an AC amplitude of 5 mV in the frequency range from 7 or 3 MHz to 0.1 Hz with 15 points/decade and 5 measurements per frequency. The PEIS measurements were evaluated with RelaxIS software (version 3.0.17.9, rhd instruments GmbH & Co. KG, Germany). For fitting, two different semicircles were used: the semicircle at the higher frequency was attributed to the SEI impedance and the semicircle at the lower frequency to the charge transfer resistance, which was not further considered. In the literature different approaches are reported.[23−25] Since the processes take place at both (symmetric) electrodes, we assume that the resistance determined for one visible semicircle is composed of the two resistances of the two electrodes. For this reason, only half of the determined resistance value is accounted for a single electrode. Five symmetric cells with coated LMAs and 150 μL electrolyte were cycled and the best performing is shown here.

■ RESULTS AND DISCUSSION

Plasma Cleaning. To examine the cleaning effect of the argon plasma, lithium foils were transferred into the plasma chamber and exposed to argon plasma for 5 min at 100 W and 1 mbar. Afterward, ToF-SIMS and XPS measurements were conducted, and the results were compared to untreated Li foils. First of all, these experiments showed that sample handling in the plasma chamber is crucial. If the lithium foils are electrically grounded together with the sample holder, lithium metal plating can occur through the natural passivation layer due to free electrons in the plasma,[26] see Supporting Information S2 for a detailed discussion. The best way to attach the lithium foil is to clamp the edges between two ceramics to electrically isolate the foils and avoid decomposition products during the plasma process at the same time.

For the plasma cleaning experiments, lithium foil, which was before stored in a glovebox, was used. It is worth mentioning that the thickness of the native passivation layer of lithium can vary due to storage conditions and impurities.[27] We chose a lithium foil with a thicker passivation layer of about 15 nm to highlight the cleaning effect of the plasma. First, the cleaning effect of the plasma was checked by reaction with nitrogen. A pristine lithium foil shows no reaction either with nitrogen gas or nitrogen plasma, as also reported by Otto et al.[27] It is well reported that a reaction with nitrogen is only possible with either a clean lithium metal surface or with lithium foil with a partially damaged passivation layer so that the nitrogen has direct access to the bare lithium metal.[27,28] The time for effective plasma cleaning depends on the thickness of the native passivation layer, and we found that 5 min argon plasma treatment is sufficient to fully remove the passivation layer and enable the reaction with nitrogen plasma, see Figure 1a. If the passivation layer is thicker or thinner, the plasma time may be adjusted. This has to be decided individually due to the mentioned influences above; see also our other work for a detailed discussion about the passivation layer formation during storage.[27] If the passivation layer is removed, one would expect to detect pure lithium metal in the XPS and ToF-SIMS measurements, which is in fact not the case. Due to the very high reactivity of lithium, the clean metal surface immediately reacts with residuals of H_2O, O_2, and CO_2 in the gloveboxes, transfer modules, and in the ToF-SIMS and XPS chambers to form a new thin passivation layer. This new passivation layer can be distinguished from the native passivation layer formed during storage due to its much lower thickness. Otto et al.[26] showed that even a freshly prepared Li surface from a lithium rod in a glovebox shows a passivation layer in ToF-SIMS and XPS due to the reactions mentioned above. The ToF-SIMS and XPS results presented in Figure 1a,b illustrate that the native passivation layer could be removed with the plasma treatment and that a new, much thinner passivation layer was formed. The ToF-SIMS depth profiles in Figure 1b show that the LiO_2H^- signal intensity, which is specific for LiOH as part of the upper native passivation layer[26] on the cleaned lithium foil, is only present at the surface and decreases immediately. In contrast, for the pristine lithium foil, the intensity remains at its maximum until a fluence of 1 × 10^{15} ions/cm^2. The XP O 1s detail spectra in Figure 1c show the presence of Li_2O for the cleaned lithium foil together with LiOH and Li_2CO_3, which can only be probed on samples with a very thin passivation layer.[26,27] However, the pristine lithium foil shows only the signals for LiOH and Li_2CO_3 due to its higher passivation layer thickness. Peak broadening for the carbonate and hydroxide peaks of the argon-cleaned lithium foil is also observed, which can have several causes, such as charging effects of the surface due to the very thin passivation layer. The areas of the fitted carbonate peaks in the O 1s spectra were constrained with the corresponding carbonate areas in the C 1s region (not shown) in the ratio of 3:1 for the chemical component Li_2CO_3.

In summary, the results show that the native passivation layer on the lithium foil can be removed/thinned by plasma treatment. Due to the high reactivity of the clean lithium surface, a new passivation layer is immediately formed by the reaction with atmospheric residuals even under inert gas conditions and also during plasma polymerization, which will be discussed later.

https://doi.org/10.1021/acsaem.3c00681
ACS Appl. Energy Mater. XXXX, XXX, XXX−XXX

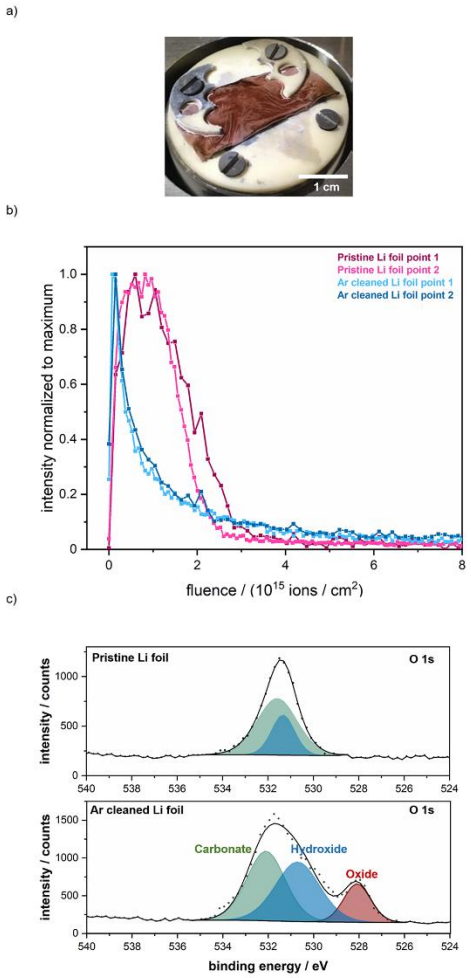

Figure 1. (a) Photograph of a lithium foil, which reacted with N_2 to Li_3N after removal of the passivation layer through plasma treatment. (b) ToF-SIMS depth profiles (area 300 × 300 μm^2, 10 keV Ar_{1500}^+ cluster) of an argon plasma cleaned lithium foil (blue) and a pristine lithium foil (red). The intensities of LiO_2H^- from two different measurement spots are shown for both samples. (c) XP O 1s spectra of a 5 min argon plasma cleaned lithium foil (bottom) and a pristine lithium foil (top).

Coating Characterization. Plasma polymerization was performed on cleaned and uncleaned lithium foils. In Figure 2a a photograph of lithium foils after plasma polymerization is shown. In contrast to the transparent parylene layers, a yellowish/golden layer is observed on the lithium foils with plasma coating. The SEM and EDX images of these samples in Figure 2b–e show a dense layer without pores consisting of spherical particles with a homogeneous distribution of fluorine and carbon. The morphology indicates a Volmer–Weber-type growth mechanism, but already after 1 min, the whole surface is covered, as the XPS and ToF-SIMS results show. Lithium is not detected at the surface, neither with XPS nor ToF-SIMS.

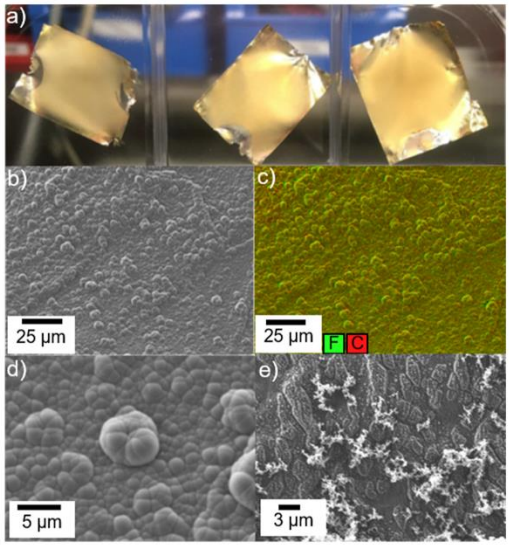

Figure 2. (a) Photographs of lithium foils (approximately 1 cm^2) coated by plasma polymerization. (b–d) SEM SE images and EDX mapping of a lithium foil coated for 15 min. (e) SEM image of a lithium foil coated for 1 min. Lithium dendrites originate from Li plating on top of the coating due to the electron beam during SEM measurements.

The layer thickness is about 2 μm after 15 min deposition time, see Supporting Information S3. The layer thickness after 1 min deposition time is about 1 μm, as alpha stepper measurements on non-air-sensitive samples showed. This indicates a non-linear growth mechanism and the setting of an equilibrium between deposition and removal of the layer by sputter effects. For XPS peak fitting of the C 1s detail spectrum in Figure 3a a Parylene HT reference sample was used, see Figure 3b for comparison. The XP spectra of the polymer coatings show the presence of sp^2 carbon, which indicates intact benzene rings, but additional CF_3 and CFH groups in comparison to Parylene HT, where only CF_2 groups are present. Also, some C–O bonds can be identified, which probably originate from contaminations in the plasma chamber. As the plasma polymerization process is less predictable than a typical chemical polymerization reaction and even a complete fragmentation of the precursor is possible, different CF_x groups and branches in the polymer network are expected compared to commercial Parylene HT. Additional ToF-SIMS measurements of the surfaces of Parylene HT and plasma-coated samples show intensities of the same m/z fragments for both samples, which also indicates the formation of a polymer chemically close to Parylene HT, see Supporting Information S4.

The coated lithium foils were also examined by ToF-SIMS depth profiling to get information on the coating composition. After removal of the passivation layer and plasma polymer coating, two or three regions are expected in a depth profile—the polymer layer, the lithium metal substrate, and possibly a thin newly formed passivation layer due to the effects mentioned above. The results in Figure 3c do not fulfill this expectation at first glance. We divided the ToF-SIMS depth

https://doi.org/10.1021/acsaem.3c00681
ACS Appl. Energy Mater. XXXX, XXX, XXX–XXX

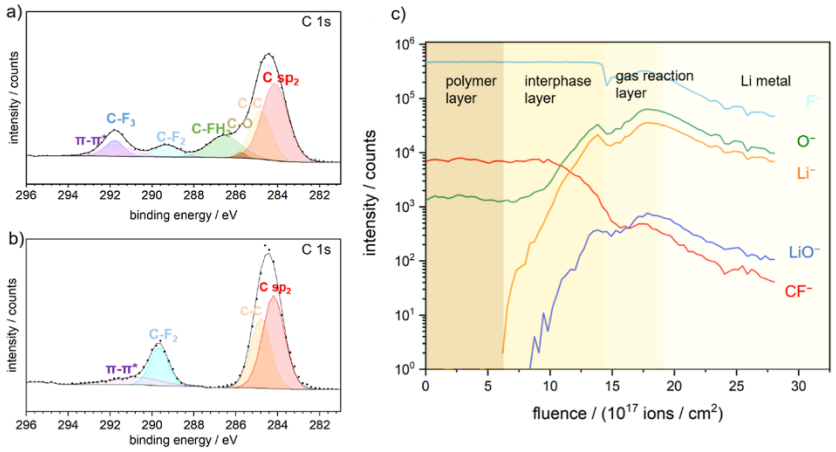

Figure 3. (a) XP C 1s detail spectrum of a lithium foil coated with a plasma polymer for 1 min. (b) C 1s detail spectrum of a commercial Parylene HT sample, which was used as a reference for peak fitting. (c) ToF-SIMS depth profile (sputter area 300 × 300 μm^2, Cs^+ ion sputtering at 2 kV) of a lithium foil coated for 1 min.

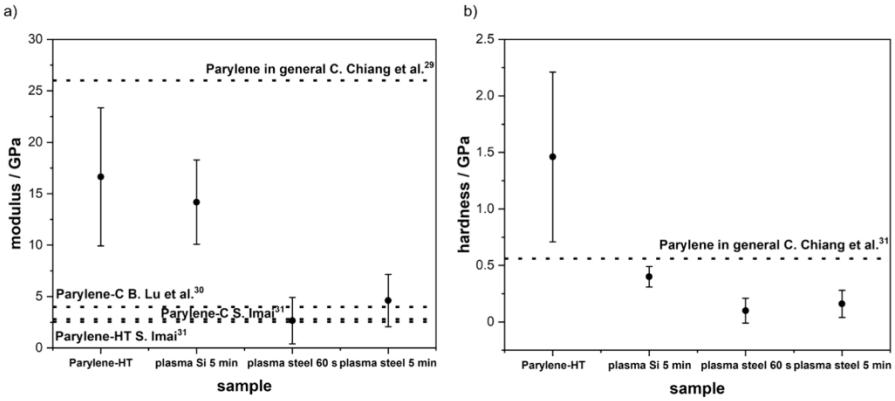

Figure 4. Data (a) for Young's modulus and (b) hardness at a displacement of 150 nm for different samples. The dotted lines represent literature values for different parylenes.

profile into different regions depending on the intensity of the chosen secondary ion signals. At the surface, the polymer is clearly identified, and no lithium is found here. This is an important observation, as it shows that indeed the whole lithium surface is protected from contact with the atmosphere. After a fluence of 7.0 × 10^{17} ions/cm^2, the Li^- intensity increases. This might indicate the diffusion of lithium from the substrate into the polymer. However, the surface roughness of the polymer layer (200 nm) can also induce this effect due to earlier probing of the lithium signal in thinner coating regions. Kern et al. also showed that the metal ion diffusion in polymers is faster in amorphous regions than in crystalline regions.[30] Therefore, the interphase layer shown in Figure 3c is probably on average thinner and the polymer layer thicker than indicated by the depth profile. Analyses at different regions of interest showed a decrease of the probable interphase layer of about 50% in areas where the lithium signal is probed later (not shown). The interphase layer shown here is the worst case (earliest lithium detection), but even there was no lithium probed at the surface. After a fluence of 1.5 × 10^{18} ions/cm^2, all intensities increase with increasing sputter fluence, which indicates a new matrix. This could be due to the formation of a reaction layer between the gaseous precursor, residuals in the plasma chamber, and the cleaned lithium foil before plasma ignition (gas reaction layer). Additional experiments showed a color change on cleaned lithium foils which were just exposed to the precursor gas, which supports the finding of higher reactivity of the cleaned foils. In our experiments, the plasma polymerization layer could also be successfully deposited on top of the native passivation layer without plasma cleaning, compare Figure 7a later. After a fluence of 1.8 × 10^{18} ions/cm^2, all intensities start to decrease, which is typical for lithium metal[26] and indicates that lithium metal is still present under the polymer layer.

Mechanical Properties of the Plasma Polymer Coating. The mechanical properties of the ASEI coatings are of

https://doi.org/10.1021/acsaem.3c00681
ACS Appl. Energy Mater. XXXX, XXX, XXX−XXX

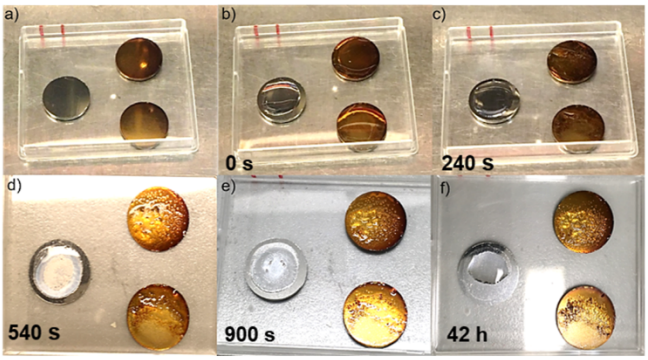

Figure 5. Pictures of uncoated (left) and coated (right) stainless-steel discs (diameter 1.5 cm) wetted with 50 μL electrolyte. (a) before wetting. (b) directly after wetting. (c) 4 min after wetting. (d) 9 min after wetting. (e) 15 min after wetting. (f) 42 h after wetting.

great interest, as a high Young's modulus of about 10 GPa is reported to be required to prevent dendrite growth.[31−33] To evaluate the mechanical properties of our plasma polymer layers, non-air sensitive substrates such as Si-wafers and steel were coated, and nanoindentation measurements were conducted and compared with commercial Parylene HT. To avoid substrate influence on the measurements, the values for Young's modulus and hardness were determined at a displacement of 150 nm (about 10% of the layer thickness). The CSMs of all samples can be found in Supporting Information S5. In Figure 4 the values of the Young's modulus and hardness for the different samples are shown in comparison to literature values for different parylenes.[34−36] The error bars represent the standard deviation. Young's modulus, hardness, and error bars for the commercial sample are the largest. The commercial sample also shows the highest roughness of about 1 μm, which results in a large scatter of the nanoindentation data (see Supporting Information S5). We cannot exclude that, due to the high surface roughness, a substrate influence may have increased the measured values. This can also be true for the plasma polymer (5 min) sample on Si. Both samples on steel are well in agreement with measured values from literature, with an average Young's modulus of 2.6 and 4.6 GPa. The very high values obtained for parylene by Chiang et al.[34] are surprising and may probably also be explained by substrate influence. For the hardness, a similar trend is found, and the plasma polymer (5 min) sample on Si is closer to the steel samples, while the commercial sample shows again a large error. The literature value for hardness from Chiang et al. is slightly larger but much closer to our measurements. All in all, the deviation for the hardness is much smaller compared to Young's modulus, with average values of 0.10 and 0.16 GPa for the steel samples and 0.40 GPa for the Si sample. This shows that the prepared polymer layers are most likely not capable of preventing longtime dendrite growth just by their stiffness—once the simple mechanical criterion is taken as correct.

Electrochemical Characterization. For a stable SEI, a homogeneous current density across the complete LMA/electrolyte interface is essential, and accordingly, a good wetting of the electrolyte is mandatory.[37] In Figure 5a−f coated and uncoated stainless steel discs, to avoid the reactivity and influence of a lithium substrate, which were wetted with 50 μL of the used electrolyte, are shown. The uncoated disc is not completely wetted, while the coated ones are completely wetted. For comparison also an uncoated LMA (diameter 13 mm) was wetted with 50 μL electrolyte, which showed bad wetting comparable to the stainless-steel disc, see Supporting Information S6. After 9 min (shown in Figure 5d) and 15 min (shown in Figure 5e), we found that the polymer layer soaks up the electrolyte and some salt remained on the surface. Finally, after 42 h (shown in Figure 5f), no electrolyte is visible any more on the surface. Considering this observation, an amount of 50 μL electrolyte (for lithium metal anodes with a diameter of 13 mm) used in symmetrical cells could be insufficient for stable battery cycling. Therefore, we used 150 μL for battery cycling to provide enough electrolyte even after absorption of electrolyte by the polymer layers. The cycling data are shown in Figure 6a−f. For cells with 50 μL electrolyte, the pristine lithium cell (Figure 6b) shows a huge overpotential after 10 h due to the SEI formation before a more or less stable overpotential is reached. After around 140 h, a short-circuit and cell failure occur. In contrast, the polymer cell (Figure 6a) does not show a high overpotential at the beginning, but after 20 h, high overpotentials occur. Considering the results of the wetting experiment, the polymer layer can protect the LMA for the first hours and enables enhanced cycling performance, but after increasing cycling time, the whole electrolyte is soaked up by the protection layer and the cell runs dry, which results in huge overpotentials. The performance of the cells with 150 μL electrolyte can be seen in Figure 6c,d. The cell with pristine lithium metal in Figure 6d shows in the beginning the same overpotentials as for 50 μL electrolyte in Figure 6b, but this time no stable overpotential was reached. Probably the formed SEI is constantly dissolving due to the excess electrolyte and being formed again, which eventually leads to dead lithium and consumption of the electrolyte, resulting in the high overpotential. Otherwise, excess electrolyte can enhance the lifetime of the cell due to longer time before the cell dries out. The cell with polymer-coated lithium shows one initial voltage spike before a stable overpotential below 0.1 V is achieved for over 300 h. Additionally, PEIS was performed to get information about the SEI resistance. In Figure 6e,f, the Nyquist plots of a cell with polymer-coated lithium (150 μL electrolyte) and a cell with pristine Li metal (50 μL electrolyte) are shown. PEIS was measured after 1 h of OCV (0) and after every cycle with 0.1 mA/cm^2. The cells with pristine lithium show a SEI resistance before cycling of 123 Ω

https://doi.org/10.1021/acsaem.3c00681
ACS Appl. Energy Mater. XXXX, XXX, XXX−XXX

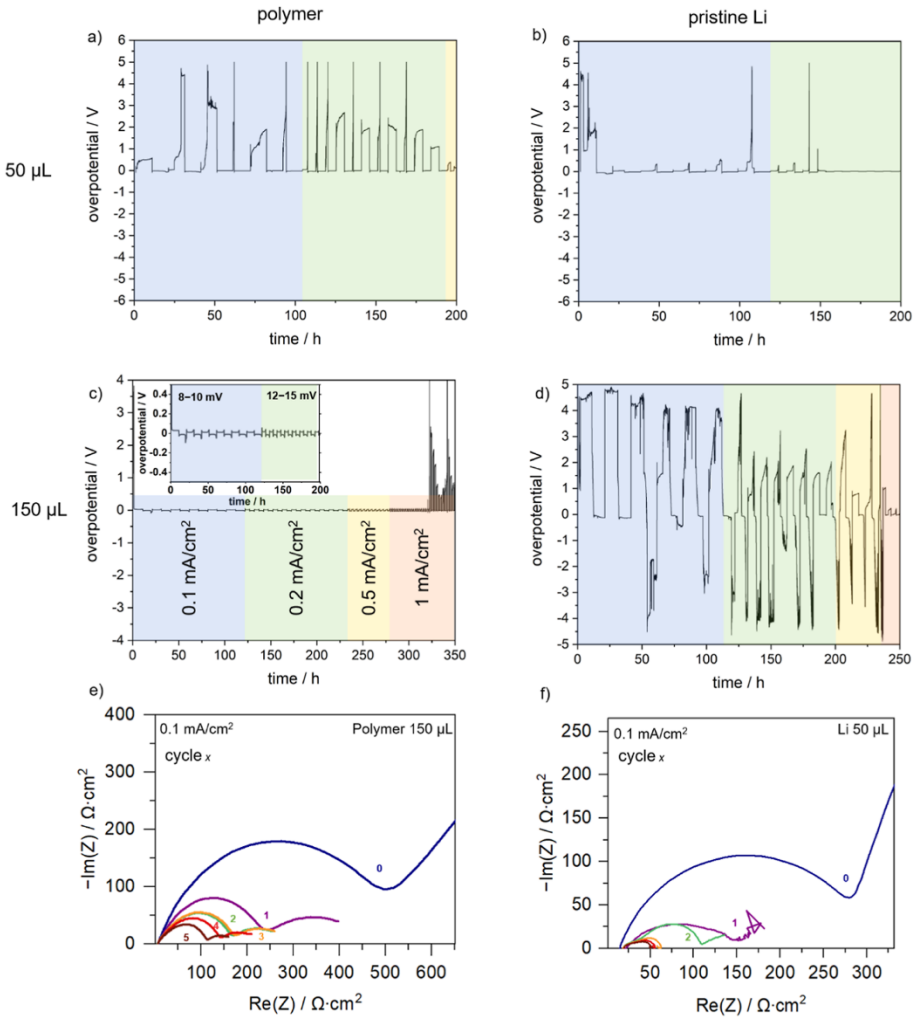

Figure 6. (a) Voltage profile of a symmetric cell with polymer-coated lithium electrodes and 50 μL electrolyte. (b) Voltage profile of a symmetric cell with pristine lithium electrodes. (c) Voltage profile of a symmetric cell with polymer-coated lithium electrodes and 150 μL electrolyte. Inset: zoom of the 0.1 and 0.2 mA/cm^2 cycling current densities. (d) Voltage profile of a symmetric cell with pristine lithium electrodes and 150 μL electrolyte. (e) Nyquist plot of the first 5 cycles at 0.1 mA/cm^2 for the cell with polymer coated lithium electrodes and 150 μL electrolyte. (f) Nyquist-plot of the first 5 cycles at 0.1 mA/cm^2 for the cell with pristine lithium and 50 μL electrolyte.

cm^2. This resistance is decreasing with increasing cycle time but also the shape of the semicircle changes. This indicates a non-uniform and instable surface/SEI due to dendrite formation. The instability of the SEI formation can be seen especially well in the PEIS measurement after the first cycle (purple) in Figure 6f. Additionally, (electro)-chemical reactions and measurement uncertainties can be expected in the lower frequency range and can have an influence on the measured data. For the cells with polymer-coated lithium, an increased resistance before cycling of about 232 Ω cm^2 is measured. This is not surprising due to the additional 1 μm thick polymer layer that was present from the start, compared to the SEI that forms over time on the uncoated lithium. After the first cycle, the resistance halves and decreases further with continuing cycling. In comparison to the pristine cell, the shape of the semicircle remains unchanged.

^{18}O Diffusion Experiments. From literature, it is not clear whether the native passivation layer (a bilayer of LiOH/Li_2CO_3 and Li_2O) on lithium foils can prevent the reaction with pure oxygen or not.[38−41] To examine the penetration of oxygen through the native passivation layer and the polymer layer, coated and uncoated samples were exposed to $^{18}O_2$ containing atmosphere for 30 min. Afterward, the samples were cooled rapidly with liquid nitrogen, and ToF-SIMS depth profiles were measured to track the local concentration and penetration depth of ^{18}O. To determine the native passivation

https://doi.org/10.1021/acsaem.3c00681
ACS Appl. Energy Mater. XXXX, XXX, XXX−XXX

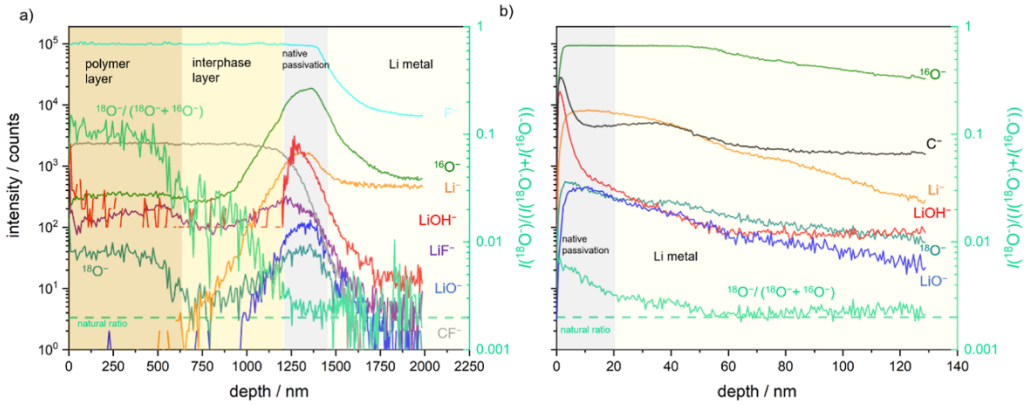

Figure 7. ToF-SIMS depth profiles of a (a) polymer-coated and (b) pristine Li foil after 30 min of $^{18}O_2$ atmosphere exposure. On the left *y*-axis, the intensities of the negative ions are plotted, and on the right *y*-axis, the $I(^{18}O^-)/(I(^{18}O^-) + I(^{16}O^-))$ (light green). The dotted line represents the natural ^{18}O fraction of 0.002, which corresponds to a concentration of 0.2%. Since the obtained ion signal intensities are proportional to the species concentration, the ^{18}O concentration can be calculated by the intensity fraction.

layer thickness, 50% of the initial LiO^- signal intensity was used. The resulting depth profiles are shown in Figure 7a,b. For the pristine Li foil in Figure 7b, the $I(^{18}O^-)/(I(^{18}O^-) + I(^{16}O^-))$ ratio is enhanced to 1% in the native passivation layer and also in the lithium metal area, which indicates diffusion of oxygen through the passivation layer but can also be influenced by the roughness of the lithium foils. The oxygen most likely reacts with the lithium metal to Li_2O, but since the amount of oxygen is very, low lithium metal is still present, and the ToF-SIMS measurements still indicate increasing lithium metal content. The coated sample in Figure 7a shows a high ratio of about 10% in the polymer layer decreasing to 1% in the interphase layer, but inhibits the oxygen diffusion strong enough to reach the natural ratio of $I(^{18}O^-)/(I(^{18}O^-) + I(^{16}O^-))$ before the beginning of the native passivation layer and lithium metal. Thus, the plasma-derived polymer layer does not only enhance the cycling performance of symmetric lithium cells considering the larger amount of electrolyte but also eases the short-term handling of LMAs and assembling of batteries due to a protective effect against residual oxygen in, e.g., gloveboxes or dry rooms. Additionally, the depth profile in Figure 7a shows that without plasma cleaning, the polymer layer is deposited on top of the native passivation layer and that no further reaction layer with atmospheric gas is formed (compare the gas reaction layer in Figure 3c).

With the sputter yields and erosion rates determined by Otto et al.,[26] the depth in Figure 7b can be calibrated, and the diffusion coefficient of oxygen in the native passivation layer of lithium can be estimated using the appropriate solution of Fick's second law. For depth calibration of the data in Figure 7a, the sputter yield of the polymer was determined by alpha stepper measurements of a ToF-SIMS crater from a polymer deposited on a non-air sensitive sample; see Supporting Information S7 for a detailed discussion. The resulting diffusion coefficient of oxygen in the native passivation layer of lithium at room temperature is $D = (4.5 \pm 0.3) \times 10^{-16}$ cm^2/s, and for oxygen in the plasma polymer, $D = (1.0 \pm 0.5) \times 10^{-12}$ cm^2/s.

DISCUSSION

The results from Takehara et al. showed that argon plasma treatment can remove the native passivation layer consisting of Li_2CO_3, LiOH, and Li_2O on top of lithium metal foils.[14,15] Following plasma polymerization with 1.1 difluorethene produced a uniform pinhole-free polymerization layer with additional crosslinking. Our experiments demonstrate the plasma polymerization of 1.4 bis(trifluoromethyl)benzene. Obviously, plasma processing can be applied to many different precursors, as long as they can be successfully added to the plasma chamber as a gas. Our analytical, mechanical, and electrochemical investigations revealed the structure of the plasma polymerized layer in detail. Not only one homogeneous layer is obtained. Depending on the reaction between the precursor and the cleaned lithium foil, up to three layers are formed during the polymerization process. Better wetting of the coated electrodes could be confirmed, as well as a major uptake of liquid electrolyte by the polymer layer. Takehara et al.[14,15] neglected the absorption of the electrolyte into the polymer layer and justified it with the low surface energy of the plasma polymer layer, but our long time wetting and cell tests showed that additional electrolyte is needed to avoid drying out of the cells. Ogumi et al.[42] produced plasma polymer layers from octamethlycyclotetrasiloxane (OMCTS). The ionic conductivity could be increased to 2.6×10^{-6} S/cm by soaking the polymer layer with butanol, poly (propylene oxide), and $LiClO_4$. This indicates that the soaking of the polymer layer with the electrolyte might not only be an additional phenomenon but also a requirement to obtain sufficient lithium ion conductivity. This gives also the possibility to pretreat the polymer layers with different solutions before assembling the batteries and construct gel-type polymer layers. The positive influence of the polymer layers was shown by Takehara et al. by suppressed dendrite growth and smoother Li plating on the coated electrodes. Our symmetric cell tests confirmed the enhanced cycling stability due to homogeneous plating and stripping. Additionally, our ^{18}O isotopic exchange experiments showed that the plasma polymerization layer can also ease the handling of LMAs and the fabrication of lithium ion batteries due to its short time

https://doi.org/10.1021/acsaem.3c00681
ACS Appl. Energy Mater. XXXX, XXX, XXX−XXX

protection against oxygen. The mechanical tests showed typical values from other parylenes from literature and a Young's modulus that is lower than the theoretically derived limit that is claimed to block dendrite growth. We assume that Young's modulus will decrease after soaking with the electrolyte such that the mechanical properties are probably decreased to even lower values. However, the electrochemical results are promising. All in all, the combined results show that plasma polymerization may well be used in producing protective layers for LMAs but that the choice of the polymer and pretreatment are critical.[14,15]

■ CONCLUSIONS

Plasma polymerization of 1.4 bis(trifluoromethyl)benzene was applied to form protecting polymer coatings on lithium metal anodes, which enable stable cycling with overpotentials below 0.1 V for over 300 h at current densities between 0.1 and 1.0 mA h/cm^2. The resulting coating layers were characterized with SEM, EDX, ToF-SIMS, and XPS and showed a dense Parylene HT like structure on top of a polymer lithium interphase layer and a layer that has formed by reaction with atmospheric gas or is a native passivation layer. Young's modulus and hardness of the formed polymer were measured by nanoindentation and resulted in average values of 2.6 and 0.10 GPa (1 min deposition) and 4.6 and 0.16 GPa (5 min deposition) for coated steel samples, respectively. With the ^{18}O diffusion experiments, the diffusion coefficients of oxygen in the native passivation layer of Li and the plasma polymer at room temperature could be estimated, and the experiments showed that the protection layer prevents oxygen diffusion through the native passivation layer and the formation of additional Li_2O for exposure times of at least 30 min despite the larger diffusion coefficient, which eases the handling and assembling of LMAs in batteries. The results show that plasma treatment/cleaning and plasma polymerization are promising approaches for the fabrication of an ASEI to enhance the cycling performance of lithium metal anodes.

■ ASSOCIATED CONTENT

Supporting Information

The Supporting Information is available free of charge at https://pubs.acs.org/doi/10.1021/acsaem.3c00681.

Schematic sketch of the plasma chamber, gas lines, and transfer module; images of different sample attachments and explanation of lithium plating during plasma treatment; SEM image of the cracked polymer; ToF-SIMS surface spectra of plasma polymer and Parylene HT; CSM measurements of Si-wafer, Parylene HT, and plasma polymer; images of wetting pristine lithium foil with electrolyte; and solution for Fick's second law and diffusion discussion (PDF)

■ AUTHOR INFORMATION

Corresponding Authors

Marcus Rohnke − *Institute of Physical Chemistry, Justus Liebig University Giessen, D-35392 Giessen, Germany; Center for Materials Research (ZfM), Justus Liebig University Giessen, D-35392 Giessen, Germany;* orcid.org/0000-0002-8867-950X; Email: Marcus.Rohnke@phys.chemie.uni-giessen.de

Jürgen Janek − *Institute of Physical Chemistry, Justus Liebig University Giessen, D-35392 Giessen, Germany; Center for Materials Research (ZfM), Justus Liebig University Giessen, D-35392 Giessen, Germany;* orcid.org/0000-0002-9221-4756; Email: Juergen.Janek@phys.chemie.uni-giessen.de

Authors

Yannik Moryson − *Institute of Physical Chemistry, Justus Liebig University Giessen, D-35392 Giessen, Germany; Center for Materials Research (ZfM), Justus Liebig University Giessen, D-35392 Giessen, Germany*

Hannah Hartmann − *Institute of Physical Chemistry, Justus Liebig University Giessen, D-35392 Giessen, Germany; Center for Materials Research (ZfM), Justus Liebig University Giessen, D-35392 Giessen, Germany*

Svenja-Katharina Otto − *Institute of Physical Chemistry, Justus Liebig University Giessen, D-35392 Giessen, Germany*

Xufei Fang − *Department of Materials and Earth Sciences, Technical University of Darmstadt, D-64287 Darmstadt, Germany;* orcid.org/0000-0002-3887-0111

Complete contact information is available at: https://pubs.acs.org/10.1021/acsaem.3c00681

Notes

The authors declare no competing financial interest.

■ ACKNOWLEDGMENTS

Y.M. and H.H. thank Specialty Coating Systems, Inc. for providing Parylene HT reference samples. The authors acknowledge financial support by the BMBF (Bundesministerium für Bildung und Forschung, Germany) within the MaLiBa (03XP0185D) project. S.K.O. acknowledges financial support (Kékulé scholarship) by the Funds of the Chemical Industry (FCI). M.R. and J.J. thank the DFG for funding of the Hybrid-SIMS (M6, IONTOF GmbH, Münster, Germany) under grant number INST 162/544-1 FUGG.

■ REFERENCES

(1) Aurbach, D. Review of selected electrode−solution interactions which determine the performance of Li and Li ion batteries. *J. Power Sources* **2000**, *89*, 206−218.

(2) Janek, J.; Zeier, W. G. A solid future for battery development. *Nat. Energy* **2016**, *1*, 16141−16144.

(3) Becking, J.; Gröbmeyer, A.; Kolek, M.; Rodehorst, U.; Schulze, S.; Winter, M.; Bieker, P.; Stan, M. C. Lithium-Metal Foil Surface Modification: An Effective Method to Improve the Cycling Performance of Lithium-Metal Batteries. *Adv. Mater. Interfaces* **2017**, *4*, 1700166−1700169.

(4) Ghazi, Z. A.; Sun, Z.; Sun, C.; Qi, F.; An, B.; Li, F.; Cheng, H. Key Aspects of Lithium Metal Anodes for Lithium Metal Batteries. *Small* **2019**, *15*, 1900687.

(5) Bai, P.; Li, J.; Brushett, F. R.; Bazant, M. Z. Transition of lithium growth mechanisms in liquid electrolytes. *Energy Environ. Sci.* **2016**, *9*, 3221−3229.

(6) Kozen, A. C.; Lin, C. F.; Zhao, O.; Lee, S. B.; Rubloff, G. W.; Noked, M. Stabilization of Lithium Metal Anodes by Hybrid Artificial Solid Electrolyte Interphase. *Chem. Mater.* **2017**, *29*, 6298−6307.

(7) Kozen, A. C.; Lin, C. F.; Pearse, A. J.; Schroeder, M. A.; Han, X.; Hu, L.; Lee, S. B.; Rubloff, G. W.; Noked, M. Next-Generation Lithium Metal Anode Engineering via Atomic Layer Deposition. *ACS Nano* **2015**, *9*, 5884−5892.

(8) Lin, C. F.; Kozen, A. C.; Noked, M.; Liu, C.; Rubloff, G. W. ALD Protection of Li-Metal Anode Surfaces - Quantifying and Preventing Chemical and Electrochemical Corrosion in Organic Solvent. *Adv. Mater. Interfaces* **2016**, *3*, 1600426.

(9) Li, G.; Huang, Q.; He, X.; Gao, Y.; Wang, D.; Kim, S. H.; Wang, D. Self-Formed Hybrid Interphase Layer on Lithium Metal for High-

Performance Lithium-Sulfur Batteries. *ACS Nano* **2018**, *12*, 1500−1507.
(10) Tao, T.; Lu, S.; Fan, Y.; Lei, W.; Huang, S.; Chen, Y. Anode Improvement in Rechargeable Lithium−Sulfur Batteries. *Adv. Mater.* **2017**, *29*, 1700542−1700619.
(11) Chen, K.; Pathak, R.; Gurung, A.; Adhamash, E. A.; Bahrami, B.; He, Q.; Qiao, H.; Smirnova, A. L.; Wu, J. J.; Qiao, Q.; Zhou, Y. Flower-shaped lithium nitride as a protective layer via facile plasma activation for stable lithium metal anodes. *Energy Storage Mater.* **2019**, *18*, 389−396.
(12) Wang, Y.; Sahadeo, E.; Rubloff, G.; Lin, C. F.; Lee, S. B. High-capacity lithium sulfur battery and beyond: a review of metal anode protection layers and perspective of solid-state electrolytes. *J. Mater. Sci.* **2018**, *54*, 3671−3693.
(13) Cheng, X.-B.; Huang, J.-Q.; Zhang, Q. Review—Li Metal Anode in Working Lithium-Sulfur Batteries. *J. Electrochem. Soc.* **2018**, *165*, A6058−A6072.
(14) Takehara, Z.; Ogumi, Z.; Uchimoto, Y.; Yasuda, K.; Yoshida, H. . Modification of lithium/electrolyte interface polymerization of 1,1-difluoroethene. *J. Power Sources* **1993**, *44*, 377−383.
(15) Takehara, Z. Future prospects of the lithium metal anode. *J. Power Sources* **1997**, *68*, 82−86.
(16) Macgregor, M.; Vasilev, K. Perspective on Plasma Polymers for Applied Biomaterials Nanoengineering and the Recent Rise of Oxazolines. *Materials* **2019**, *12*, 191.
(17) Golda-Cepa, M.; Engvall, K.; Hakkarainen, M.; Kotarba, A. Recent progress on parylene C polymer for biomedical applications: A review. *Prog. Org. Coat.* **2020**, *140*, 105493.
(18) Jung, Y. H.; Qiu, Y.; Lee, S.; Shih, T.-Y.; Xu, Y.; Xu, R.; Lee, J.; Schendel, A. A.; Lin, W.; Williams, J. C.; Behdad, N.; Ma, Z. A Compact Parylene-Coated WLAN Flexible Antenna for Implantable Electronics. *IEEE Antennas Wirel. Propag. Lett.* **2016**, *15*, 1382−1385.
(19) Lu, B.; Zhu, D.; Hinton, D.; Humayun, M. S.; Tai, Y.-C. Mesh-supported submicron parylene-C membranes for culturing retinal pigment epithelial cells. *Biomed. Microdevices* **2012**, *14*, 659−667.
(20) Kim, B. J.; Meng, E. Micromachining of Parylene C for bioMEMS. *Polym. Adv. Technol.* **2016**, *27*, 564−576.
(21) Shin, Y. S.; Cho, K.; Lim, S. H.; Chung, S.; Park, S.-J.; Chung, C.; Han, D.-C.; Chang, J. K. PDMS-based micro PCR chip with Parylene coating. *J. Micromech. Microeng.* **2003**, *13*, 768−774.
(22) Rohnke, M.; Janek, J.; Kilner, J. A.; Chater, R. J. Surface oxygen exchange between yttria-stabilised zirconia and a low-temperature oxygen rf-plasma. *Solid State Ionics* **2004**, *166*, 89−102.
(23) Drvarič Talian, S.; Bobnar, J.; Sinigoj, A. R.; Humar, I.; Gaberšček, M. Transmission Line Model for Description of the Impedance Response of Li Electrodes with Dendritic Growth. *J. Phys. Chem. C* **2019**, *123*, 27997−28007.
(24) Ran, Q.; Han, C.; Tang, A.; Chen, H.; Tang, Z.; Jiang, K.; Mai, Y.; Wang, J. Multifunctional artificial solid electrolyte interphase layer for lithium metal anode in carbonate electrolyte. *Solid State Ionics* **2020**, *344*, 115095.
(25) Pang, Q.; Liang, X.; Shyamsunder, A.; Nazar, L. F. An In Vivo Formed Solid Electrolyte Surface Layer Enables Stable Plating of Li Metal. *Joule* **2017**, *1*, 871−886.
(26) Otto, S.-K.; Moryson, Y.; Krauskopf, T.; Peppler, K.; Sann, J.; Janek, J.; Henss, A. In-Depth Characterization of Lithium-Metal Surfaces with XPS and ToF-SIMS: Toward Better Understanding of the Passivation Layer. *Chem. Mater.* **2021**, *33*, 859−867.
(27) Otto, S. K.; Fuchs, T.; Moryson, Y.; Lerch, C.; Mogwitz, B.; Sann, J.; Janek, J.; Henss, A. Storage of Lithium Metal: The Role of the Native Passivation Layer for the Anode Interface Resistance in Solid State Batteries. *ACS Appl. Energy Mater.* **2021**, *4*, 12798−12807.
(28) Jain, A.; Miyaoka, H.; Kumar, S.; Ichikawa, T.; Kojima, Y. A new synthesis route of ammonia production through hydrolysis of metal−Nitrides. *Int. J. Hydrogen Energy* **2017**, *42*, 24897−24903.
(29) Yildirim, H.; Kinaci, A.; Chan, M. K. Y.; Greeley, J. P. First-Principles Analysis of Defect Thermodynamics and Ion Transport in Inorganic SEI Compounds: LiF and NaF. *ACS Appl. Mater. Interfaces* **2015**, *7*, 18985−18996.
(30) Kern, S.; Kern, C.; Pradja, M. M.; Düring, R. A.; Rohnke, M. Spatially resolved indiffusion behavior of Cu^{2+} and Ni^{2+} in polypropylene. *J. Appl. Polym. Sci.* **2021**, *138*, 49655−49713.
(31) Cheng, X. B.; Zhang, R.; Zhao, C. Z.; Zhang, Q. Toward Safe Lithium Metal Anode in Rechargeable Batteries: A Review. *Chem. Rev.* **2017**, *117*, 10403−10473.
(32) Xu, W.; Wang, J.; Ding, F.; Chen, X.; Nasybulin, E.; Zhang, Y.; Zhang, J. G. Lithium metal anodes for rechargeable batteries. *Energy Environ. Sci.* **2014**, *7*, 513−537.
(33) Yu, Z.; Cui, Y.; Bao, Z. Design Principles of Artificial Solid Electrolyte Interphases for Lithium-Metal Anodes. *Cell Rep. Phys. Sci.* **2020**, *1*, 100119.
(34) Chiang, C.; Neubauer, G.; Mack, A. S.; Yoshioka, K.; Cuan, G.; Flinn, P. A.; Fraser, D. B. Hardness and Modulus studies on dielectric thin films. *Mater. Res. Soc. Symp. Proc.* **1992**, *265*, 219−230.
(35) Lu, B.; Zheng, S.; Quach, B. Q.; Tai, Y. C. A study of the autofluorescence of parylene materials for μtAS applications. *Lab Chip* **2010**, *10*, 1826−1834.
(36) Imai, S. Fabrication of three-dimensional parylene HT diaphragms using D-RIE with a Si substrate. *Sens. Actuators, A* **2017**, *253*, 146−155.
(37) Cao, Y.; Meng, X.; Elam, J. W. Atomic Layer Deposition of Li_xAl_yS Solid-State Electrolytes for Stabilizing Lithium-Metal Anodes. *ChemElectroChem* **2016**, *3*, 858−863.
(38) Zhuang, G.; Ross, P. N.; Kong, F.; McLarnon, F. The Reaction of Clean Li Surfaces with Small Molecules in Ultrahigh Vacuum: II. Water. *J. Electrochem. Soc.* **1998**, *145*, 159−164.
(39) Grossweiner, L. I.; Seifert, R. L. The Reaction of Lithium with Water Vapor. *J. Am. Chem. Soc.* **1952**, *74*, 2701−2704.
(40) Markowitz, M. M.; Boryta, D. A. Lithium Metal-Gas Reactions. *J. Chem. Eng. Data* **1962**, *7*, 586−591.
(41) Skinner, C. H.; Sullenberger, R.; Koel, B. E.; Jaworski, M. A.; Kugel, H. W. Plasma facing surface composition during NSTX Li experiments. *J. Nucl. Mater.* **2013**, *438*, S647−S650.
(42) Ogumi, Z.; Uchimoto, Y.; Takehara, Z. Ionically Conductive Thin Polymer Film Prepared by Plasma Polymerization: I . Hybrid Film of Plasma Polymer Formed from Octamethylcyclotetrasiloxane, Poly(propylene oxide), and Lithium Perchlorate. *J. Electrochem. Soc.* **1989**, *136*, 625−630.

https://doi.org/10.1021/acsaem.3c00681
ACS Appl. Energy Mater. XXXX, XXX, XXX−XXX

4. Conclusions

On the cathode side in LIBs or ASSBs, NCM-based CAMs are used in the majority. Despite the change in composition and the resulting increase in stability, it is still not sufficient to ensure long-term cycling. This is due to (electro)chemical degradation processes, which occur mainly at the interfaces between the CAM and the electrolyte. To suppress these degradation processes, thin protective layers are applied to the CAM particles. The most important properties of the protective layers are their ionic conductivity and very low electronic conductivity. In addition, their chemical stability with respect to the electrolyte and their mechanical deformability are of decisive importance. Suitable coating materials are e.g. $LiNbO_3$ or high *k* materials such as Al_2O_3. The coatings can be applied to the NCM particles in various ways, with ALD being a particularly suitable option due to its high conformity. Since the dimensions and topography of the coated particles are very small and challenging, the analysis of the layers and interfaces is very difficult. In publication 1, this problem was addressed and the conventional methods were supplemented with new methods, as well as guidelines for a comprehensive analysis and to avoid pitfalls were given.

It should be mentioned once again that an understanding of the protective properties of the protective coatings is only possible through comprehensive analysis and thus plays an important role in the development of new coatings. The results of publication 1 show that, in addition to established methods such as XPS and SEM, LEIS and ToF-SIMS in particular are useful additions to the investigation of protective coatings. LEIS, the most surface-sensitive method, can be used to elucidate the elemental compositions at the surface, which later has contact with the electrolyte. Additionally, LEIS can provide information on whether most of the substrate is completely coated, since the investigated area is very large (mm). ToF-SIMS imaging combines the ability to combine semi-quantitative chemical information with imaging information to provide a more accurate picture of the protective layer and degradation products. For XPS the energy calibration is very important, since a shift from the surface into the bulk can be attributed to charging effects due to carbon impurities at the surface and vertical charging due to insulating layers on conductive samples[89]. With SEM/FIB-SEM the determination of the protection layer can be very challenging, since contrast differences depend on the composition of the protection layer and might not be sufficient. Additionally, re-deposition takes places and may form a much thicker and better visible layer than the original protection layer. Nevertheless, it might still be a rather fast and easy method to see if a coating process was successful. The Raman spectroscopy offers in combination with reference samples of the pure coating material a fast and experimental easy approach to check if a coating process was successful, as long as the used material is Raman-active. Furthermore, it has been shown that a proper sample preparation plays an important role in obtaining meaningful results. For ToF-SIMS, embedding of the coated NCM particles in Technovit® enables the analysis in the same *z*-plane and suppresses differential sputter effects at the cost of total ion intensity. With TEM it is possible to grind the coated particles beforehand with ethanol, which breaks the secondary particle structure and enables the examination of the single particles. Since a large number of “inner” primary particles are not coated, it is statistically harder to find a coated particle but if found the layer thickness can be easily determined. Last but not least a clean working environment during sample preparation and the measurement are mandatory to avoid degradation and sample changes.

In the second publication the composition of the native passivation layer of lithium metal (foils) could be elucidated which is an important step for enabling the LMA, which is considered the holy grail for battery systems. The native passivation layer, which is always present and also forms immediately after removal consists of a bilayer of Li_2CO_3/LiOH and Li_2O. For lithium metal the sample handling and preparation are even more crucial than for NCM, since lithium metal will react with residuals such as water, oxygen or nitrogen.[15] Another very important point to be considered is to avoid lithium plating during the analysis due to electron beams and an electronically grounded sample.

Since the native passivation is not sufficient to protect the lithium during cycling, ASEIs have to be applied. The plasma polymerization presented in publication 3 is a very promising method due to the possible combination of a cleaning step with e.g. an Ar plasma and a coating step in one setup. Plasma polymerization has not been utilized for battery materials since the 1990s by Takehara et al.[67,68,90]. Especially the high number of possible precursors makes the plasma polymerization an interesting method. To ensure a proper deposition the lithium plating has to be avoided. Since free electrons are also present in the plasma, the samples must not be grounded. A possible solution is to affix the lithium foils with ceramic clamps onto a ceramic plate. Plasma polymerization of 1.4-bis(trifluoromethyl)benzene lead to a polymer with a similar structure as Parylene HT® with additional crosslinking. Symmetrical cell tests with coated LMAs showed an enhanced cycling stability with low overpotentials for over 300 h at current densities between 0.1 and 1 mA/cm^2 in comparison to uncoated LMAs. Since the polymer layers soak up electrolyte more electrolyte is needed to avoid cell dry out. Protection layers should ideally also ease the handling and cell manufacturing of LMAs. The results of ^{18}O diffusion experiments showed that even though the diffusion coefficient of oxygen in the polymer layer is several times greater than in the native passivation layer, the combination of thickness and diffusion coefficient is sufficient to protect the LMA at least for 30 minutes against oxygen.

Overall this thesis emphasizes that the combination of electrochemistry and comprehensive analytics is key to understand the protective effects and develop new coatings. The thesis shows that ALD and plasma polymerization are two very promising methods to apply coatings on battery electrode materials. It gives an overview of different coating materials, as well as advice and guidelines on a proper analysis in order to avoid pitfalls with the available analytical machines. Last but not least the presented polymer coating enhances the cycling stability of symmetric LMA cells and might be another step into enabling next generation batteries with a working LMA.

5. Outlook

i. Compiling a database of electrochemical performance and coating properties

A systematic and comprehensive analyses is key to ensure reproducibility and a deeper understanding of the protective properties of coatings. Therefore, different coating thicknesses have to be applied and correlated to their electrochemical performance. A thorough analysis with a combination of the presented methods in this thesis could then be the start of databases, which help to predict ideal precursors and requirements for protective coatings. This can be done both on the cathode and anode (LMA) side. It is also important to have a look at the coatings post-mortem to examine the degradation products that form during cycling.

ii. Pretreatment

Of course, other coating techniques besides the ALD and plasma polymerization are usable in further studies but the high conformity and controllability of the ALD make a strong case to be a leading technique for applying coatings on CAMs. The plasma polymerization gives the great opportunity to combine a cleaning step and coating step in one setup under vacuum conditions, which minimizes the risk of contaminations during the coating process in contrast to e.g. liquid based processes. The produced polymer layers can be pre-treated with different electrolyte solutions to enhance the Li-ion conductivity and reduce the uptake of electrolyte in the liquid cells.

iii. Coating of different battery parts

It is also thinkable to apply the protective coatings on the electrolyte in ASSBs or current collectors in anode free setups. The mentioned techniques should work for that as well, since the requirements for lithium metal a much greater. Nevertheless, the coatings might behave different on these substrates and therefore have to be analyzed again.

iv. Coordination between research and industry

Regardless of which coating technique or substrates are selected, close communication and cooperation between research and industry is very important, which has been partially neglected in the past. In industry, equipment is already available for many processes, so it would be advantageous to develop improvements for such approaches. In addition, the coatings produced on a laboratory scale must also be realistically scalable in order to become a competitive product. Especially when it comes to large-scale production, the systematic analysis and influencing factors of protective coatings should have been thoroughly investigated in advance in order to avoid expensive re-designs.

6. References

1. Whittingham M.S. Electrical Energy Storage and Intercalation Chemistry. *Science (80-.).* **192**, 1126–1127 (1976).

2. Mizushima, K., Jones, P. C., Wiseman, P. J. & Goodenough, J. B. Li_xCoO_2 (0<x≤1): A new cathode material for batteries of high energy density. *Mater. Res. Bull.* **15**, 783–789 (1980).

3. Lin, D., Liu, Y. & Cui, Y. Reviving the lithium metal anode for high-energy batteries. *Nat. Nanotechnol.* **12**, 194–206 (2017).

4. Janek, J. & Zeier, W. G. A solid future for battery development. *Nat. Energy* **1**, 1–4 (2016).

5. Ping, P., Wang, Q. S., Huang, P. F., Li, K., Sun, J., Kong, D. P. & Chen, C. H. Study of the fire behavior of high-energy lithium-ion batteries with full-scale burning test. *J. Power Sources* **285**, 80–89 (2015).

6. Zhou, H., Yu, S., Liu, H. & Liu, P. Protective coatings for lithium metal anodes: Recent progress and future perspectives. *J. Power Sources* **450**, 227632 (2020).

7. Koerver, R., Zhang, W., De Biasi, L., Schweidler, S., Kondrakov, A. O., Kolling, S., Brezesinski, T., Hartmann, P., Zeier, W. G. & Janek, J. Chemo-mechanical expansion of lithium electrode materials-on the route to mechanically optimized all-solid-state batteries. *Energy Environ. Sci.* **11**, 2142–2158 (2018).

8. Koerver, R., Aygün, I., Leichtweiß, T., Dietrich, C., Zhang, W., Binder, J. O., Hartmann, P., Zeier, W. G. & Janek, J. Capacity Fade in Solid-State Batteries: Interphase Formation and Chemomechanical Processes in Nickel-Rich Layered Oxide Cathodes and Lithium Thiophosphate Solid Electrolytes. *Chem. Mater.* **29**, 5574–5582 (2017).

9. Culver, S. P., Koerver, R., Zeier, W. G. & Janek, J. On the Functionality of Coatings for Cathode Active Materials in Thiophosphate-Based All-Solid-State Batteries. *Adv. Energy Mater.* **9**, (2019).

10. Qin, C., Cao, J., Chen, J., Dai, G., Wu, T., Chen, Y., Tang, Y., Li, A. & Chen, Y. Improvement of electrochemical performance of nickel rich $LiNi_{0.6}Co_{0.2}Mn_{0.2}O_2$ cathode active material by ultrathin TiO_2 coating. *Dalt. Trans.* **45**, 9669–9675 (2016).

11. Zou, G., Yang, X., Wang, X., Ge, L., Shu, H., Bai, Y., Wu, C., Guo, H., Hu, L., Yi, X., Ju, B., Hu, H., Wang, D. & Yu, R. Improvement of electrochemical performance for Li-rich spherical $Li_{1.3}[Ni_{0.35}Mn_{0.65}]O_2$+x modified by Al_2O_3. *J. Solid State Electrochem.* **18**, 1789–1797 (2014).

12. Woo, S.-U., Park, B.-C., Yoon, C. S., Myung, S.-T., Prakash, J. & Sun, Y.-K. Improvement of Electrochemical Performances of $Li[Ni_{0.8}Co_{0.1}Mn_{0.1}]O_2$ Cathode Materials by Fluorine Substitution. *J. Electrochem. Soc.* **154**, A649 (2007).

13. Woo, S.-U., Yoon, C. S., Amine, K., Belharouak, I. & Sun, Y.-K. Significant Improvement of Electrochemical Performance of AlF_3-Coated $Li[Ni_{0.8}Co_{0.1}Mn_{0.1}]O_2$ Cathode Materials. *J. Electrochem. Soc.* **154**, A1005 (2007).

14. Otto, S.-K., Moryson, Y., Krauskopf, T., Peppler, K., Sann, J., Janek, J. & Henss, A. In-Depth Characterization of Lithium-Metal Surfaces with XPS and ToF-SIMS: Toward Better Understanding of the Passivation Layer. *Chem. Mater.* (2021)

doi:10.1021/acs.chemmater.0c03518.

15. Otto, S. K., Fuchs, T., Moryson, Y., Lerch, C., Mogwitz, B., Sann, J., Janek, J. & Henss, A. Storage of Lithium Metal: The Role of the Native Passivation Layer for the Anode Interface Resistance in Solid State Batteries. *ACS Appl. Energy Mater.* **4**, 12798–12807 (2021).

16. Liu, W., Oh, P., Liu, X., Lee, M. J., Cho, W., Chae, S., Kim, Y. & Cho, J. Nickel-Rich Layered Lithium Transition-Metal Oxide for High-Energy Lithium-Ion Batteries. *Angew. Chemie - Int. Ed.* **54**, 4440–4457 (2015).

17. Ahmed, S., Bianchini, M., Pokle, A., Munde, M. S., Hartmann, P., Brezesinski, T., Beyer, A., Janek, J. & Volz, K. Visualization of Light Elements using 4D STEM: The Layered-to-Rock Salt Phase Transition in $LiNiO_2$ Cathode Material. *Adv. Energy Mater.* **2001026**, 1–9 (2020).

18. Thackeray, M. M., David, W. I. F., Bruce, P. G. & Goodenough, J. B. Lithium insertion into manganese spinels. *Mater. Res. Bull.* **18**, 461–472 (1983).

19. Noh, H. J., Youn, S., Yoon, C. S. & Sun, Y. K. Comparison of the structural and electrochemical properties of layered $Li[Ni_xCo_yMn_z]O_2$ (x = 1/3, 0.5, 0.6, 0.7, 0.8 and 0.85) cathode material for lithium-ion batteries. *J. Power Sources* **233**, 121–130 (2013).

20. Walther, F., Koerver, R., Fuchs, T., Ohno, S., Sann, J., Rohnke, M., Zeier, W. G. & Janek, J. Visualization of the Interfacial Decomposition of Composite Cathodes in Argyrodite-Based All-Solid-State Batteries Using Time-of-Flight Secondary-Ion Mass Spectrometry. *Chem. Mater.* (2019) doi:10.1021/acs.chemmater.9b00770.

21. Kondrakov, A. O., Schmidt, A., Xu, J., Geßwein, H., Mönig, R., Hartmann, P., Sommer, H., Brezesinski, T. & Janek, J. Anisotropic Lattice Strain and Mechanical Degradation of High- and Low-Nickel NCM Cathode Materials for Li-Ion Batteries. *J. Phys. Chem. C* **121**, 3286–3294 (2017).

22. Visbal, H., Aihara, Y., Ito, S., Watanabe, T., Park, Y. & Doo, S. The effect of diamond-like carbon coating on $LiNi_{0.8}Co_{0.15}Al_{0.05}O_2$ particles for all solid-state lithium-ion batteries based on Li2S-P2S5 glass-ceramics. *J. Power Sources* **314**, 85–92 (2016).

23. Minnmann, P., Strauss, F., Bielefeld, A., Ruess, R., Adelhelm, P., Burkhardt, S., Dreyer, S. L., Trevisanello, E., Ehrenberg, H., Brezesinski, T., Richter, F. H. & Janek, J. Designing Cathodes and Cathode Active Materials for Solid-State Batteries. *Adv. Energy Mater.* (2022) doi:10.1002/aenm.202201425.

24. Neudeck, S., Mazilkin, A., Reitz, C., Hartmann, P., Janek, J. & Brezesinski, T. Effect of Low-Temperature Al_2O_3 ALD Coating on Ni-Rich Layered Oxide Composite Cathode on the Long-Term Cycling Performance of Lithium-Ion Batteries. *Sci. Rep.* **9**, 1–11 (2019).

25. Razmjoo Khollari, M. A., Paknahad, P. & Ghorbanzadeh, M. Improvement of the electrochemical performance of a nickel rich $LiNi_{0.5}Co_{0.2}Mn_{0.3}O_2$ cathode material by reduced graphene oxide/SiO_2 nanoparticle double-layer coating. *New J. Chem.* **43**, 2766–2775 (2019).

26. Shi, Y., Zhang, M., Qian, D. & Meng, Y. S. Ultrathin Al_2O_3 Coatings for Improved Cycling Performance and Thermal Stability of $LiNi_{0.5}Co_{0.2}Mn_{0.3}O_2$ Cathode Material. *Electrochim. Acta* **203**, 154–161 (2016).

27. Wu, Y., Li, M., Wahyudi, W., Sheng, G., Miao, X., Anthopoulos, T. D., Huang, K.

W., Li, Y. & Lai, Z. Performance and Stability Improvement of Layered NCM Lithium-Ion Batteries at High Voltage by a Microporous Al_2O_3 Sol-Gel Coating. *ACS Omega* **4**, 13972–13980 (2019).

28. Strauss, F., Teo, J. H., Maibach, J., Kim, A. Y., Mazilkin, A., Janek, J. & Brezesinski, T. Li_2ZrO_3-Coated NCM622 for Application in Inorganic Solid-State Batteries: Role of Surface Carbonates in the Cycling Performance. *ACS Appl. Mater. Interfaces* **12**, 57146–57154 (2020).

29. Kim, A. Y., Strauss, F., Bartsch, T., Teo, J. H., Hatsukade, T., Mazilkin, A., Janek, J., Hartmann, P. & Brezesinski, T. Stabilizing Effect of a Hybrid Surface Coating on a Ni-Rich NCM Cathode Material in All-Solid-State Batteries. *Chem. Mater.* **31**, 9664–9672 (2019).

30. Neudeck, S., Walther, F., Bergfeldt, T., Suchomski, C., Rohnke, M., Hartmann, P., Janek, J. & Brezesinski, T. Molecular Surface Modification of NCM622 Cathode Material Using Organophosphates for Improved Li-Ion Battery Full-Cells. *ACS Appl. Mater. Interfaces* **10**, 20487–20498 (2018).

31. Herzog, M. J., Gauquelin, N., Esken, D., Verbeeck, J. & Janek, J. Facile Dry Coating Method of High-Nickel Cathode Material by Nanostructured Fumed Alumina (Al_2O_3) Improving the Performance of Lithium-Ion Batteries. *Energy Technol.* **2100028**, (2021).

32. Yada, C., Lee, C. E., Laughman, D., Hannah, L., Iba, H. & Hayden, B. E. A High-Throughput Approach Developing Lithium-Niobium-Tantalum Oxides as Electrolyte/Cathode Interlayers for High-Voltage All-Solid-State Lithium Batteries. *J. Electrochem. Soc.* **162**, A722–A726 (2015).

33. Yada, C., Ohmori, A., Ide, K., Yamasaki, H., Kato, T., Saito, T., Sagane, F. & Iriyama, Y. Dielectric modification of 5V-class cathodes for high-voltage all-solid-state lithium batteries. *Adv. Energy Mater.* **4**, 1–5 (2014).

34. Ito, S., Fujiki, S., Yamada, T., Aihara, Y., Park, Y., Kim, T. Y., Baek, S. W., Lee, J. M., Doo, S. & Machida, N. A rocking chair type all-solid-state lithium ion battery adopting Li_2O-ZrO_2 coated $LiNi_{0.8}Co_{0.15}Al_{0.05}O_2$ and a sulfide based electrolyte. *J. Power Sources* **248**, 943–950 (2014).

35. Walther, F., Strauss, F., Wu, X., Mogwitz, B., Hertle, J., Sann, J., Rohnke, M., Brezesinski, T. & Janek, J. The Working Principle of a Li_2CO_3 /$LiNbO_3$ Coating on NCM for Thiophosphate-Based All-Solid-State Batteries . *Chem. Mater.* (2021) doi:10.1021/acs.chemmater.0c04660.

36. Ohta, N., Takada, K., Sakaguchi, I., Zhang, L., Ma, R., Fukuda, K., Osada, M. & Sasaki, T. $LiNbO_3$-coated $LiCoO_2$ as cathode material for all solid-state lithium secondary batteries. *Electrochem. commun.* **9**, 1486–1490 (2007).

37. Neudeck, S., Walther, F., Bergfeldt, T., Suchomski, C., Rohnke, M., Hartmann, P., Janek, J. & Brezesinski, T. Molecular Surface Modification of NCM622 Cathode Material Using Organophosphates for Improved Li-Ion Battery Full-Cells. *ACS Appl. Mater. Interfaces* **10**, 20487–20498 (2018).

38. Wang, Z., Zhong, H. & Song, G. Enhancing high-voltage performance of $LiNi_{0.8}Co_{0.1}Mn_{0.1}O_2$ by coating with NASICON fast ionic conductor $Li_{1.5}Al_{0.5}Zr_{1.5}(PO_4)_3$. *J. Alloys Compd.* **849**, 156467 (2020).

39. MacHida, N., Kashiwagi, J., Naito, M. & Shigematsu, T. Electrochemical properties of all-solid-state batteries with ZrO_2-coated $LiNi_{1/3}Mn_{1/3}Co_{1/3}O_2$ as cathode materials. *Solid State Ionics* **225**, 354–358 (2012).

40. Dannehl, N., Steinmüller, S. O., Szabó, D. V., Pein, M., Sigel, F., Esmezjan, L., Hasenkox, U., Schwarz, B., Indris, S. & Ehrenberg, H. High-Resolution Surface Analysis on Aluminum Oxide-Coated $Li_{1.2}Mn_{0.55}Ni_{0.15}Co_{0.1}O_2$ with Improved Capacity Retention. *ACS Appl. Mater. Interfaces* acsami.8b09550 (2018) doi:10.1021/acsami.8b09550.

41. Kang, Y. J., Kim, J. H., Lee, S. W. & Sun, Y. K. The effect of $Al(OH)_3$ coating on the $Li[Li_{0.2}Ni_{0.2}Mn_{0.6}]O_2$ cathode material for lithium secondary battery. *Electrochim. Acta* **50**, 4784–4791 (2005).

42. Takada, K., Ohta, N., Zhang, L., Xu, X., Hang, B. T., Ohnishi, T., Osada, M. & Sasaki, T. Interfacial phenomena in solid-state lithium battery with sulfide solid electrolyte. *Solid State Ionics* **225**, 594–597 (2012).

43. Huang, Y., Huang, Y. & Hu, X. Enhanced electrochemical performance of $LiNi_{0.8}Co_{0.15}Al_{0.05}O_2$ by nanoscale surface modification with Co_3O_4. *Electrochim. Acta* **231**, 294–299 (2017).

44. Lai, Y. Q., Xu, M., Zhang, Z. A., Gao, C. H., Wang, P. & Yu, Z. Y. Optimized structure stability and electrochemical performance of $LiNi_{0.8}Co_{0.15}Al_{0.05}O_2$ by sputtering nanoscale ZnO film. *J. Power Sources* **309**, 20–26 (2016).

45. Chen, Z. & Zhang, Q. Carbon-Coatings Improve Performance of Li-Ion Battery. 1–27 (2022).

46. Yamagishi, Y., Morita, H., Nomura, Y. & Igaki, E. Visualizing Lithium Distribution and Degradation of Composite Electrodes in Sul fi de-based All-Solid-State Batteries Using Operando Time-of-Flight Secondary Ion Mass Spectrometry. (2021) doi:10.1021/acsami.0c18505.

47. Tornheim, A., Maroni, V. A., He, M., Gosztola, D. J. & Zhang, Z. Enhanced Raman Scattering from NCM523 Cathodes Coated with Electrochemically Deposited Gold. *J. Electrochem. Soc.* **164**, A3000–A3005 (2017).

48. Hoskins, A. L., McNeary, W. W., Millican, S. L., Gossett, T. A., Lai, A., Gao, Y., Liang, X., Musgrave, C. B. & Weimer, A. W. Nonuniform Growth of Sub-2 Nanometer Atomic Layer Deposited Alumina Films on Lithium Nickel Manganese Cobalt Oxide Cathode Battery Materials. *ACS Appl. Nano Mater.* 6989–6997 (2019) doi:10.1021/acsanm.9b01490.

49. Moryson, Y., Walther, F., Sann, J., Mogwitz, B., Ahmed, S., Burkhardt, S., Chen, L., Klar, P. J., Volz, K., Fearn, S., Rohnke, M. & Janek, J. Analyzing Nanometer-Thin Cathode Particle Coatings for Lithium-Ion Batteries—The Example of TiO_2 on NCM622. *ACS Appl. Energy Mater.* **4**, 7168–7181 (2021).

50. Becking, J., Gröbmeyer, A., Kolek, M., Rodehorst, U., Schulze, S., Winter, M., Bieker, P. & Stan, M. C. Lithium-Metal Foil Surface Modification: An Effective Method to Improve the Cycling Performance of Lithium-Metal Batteries. *Adv. Mater. Interfaces* **4**, 1–9 (2017).

51. Wang, Y., Sahadeo, E., Rubloff, G., Lin, C. F. & Lee, S. B. High-capacity lithium sulfur battery and beyond: a review of metal anode protection layers and perspective of solid-state electrolytes. *J. Mater. Sci.* **54**, 3671–3693 (2018).

52. Schily, U. & Heitbaum, J. Surface analysis of freshly cut Li samples: Na-segregation and film forming reaction by O_2, SO_2, and liquid $LiAlCl_4 \cdot 3(SO_2)$. *Electrochim. Acta* **37**, 731–738 (1992).

53. Meyerson, M. L., Sheavly, J., Dolocan, A., Griffin, M., Pandit, A., Rodriguez, R.,

Stephens, R. M., Vanden Bout, D., Heller, A. & Mullins, C. The Effect of Local Lithium Surface Chemistry and Topography on Solid Electrolyte Interphase Composition and Dendrite Nucleation. *J. Mater. Chem. A* (2019) doi:10.1039/C9TA03371H.

54. Maslyn, J. A., Frenck, L., Loo, W. S., Parkinson, D. Y. & Balsara, N. P. Extended cycling through rigid block copolymer electrolytes enabled by reducing impurities in lithium metal electrodes. *ACS Appl. Energy Mater.* **2**, 8197–8206 (2019).

55. Harry, K. J., Hallinan, D. T., Parkinson, D. Y., MacDowell, A. A. & Balsara, N. P. Detection of subsurface structures underneath dendrites formed on cycled lithium metal electrodes. *Nat. Mater.* **13**, 69–73 (2014).

56. Yu, Z., Cui, Y. & Bao, Z. Design Principles of Artificial Solid Electrolyte Interphases for Lithium-Metal Anodes. *Cell Reports Phys. Sci.* **1**, 100119 (2020).

57. Chen, L., Connell, J. G., Nie, A., Huang, Z., Zavadil, K. R., Klavetter, K. C., Yuan, Y., Sharifi-Asl, S., Shahbazian-Yassar, R., Libera, J. A., Mane, A. U. & Elam, J. W. Lithium metal protected by atomic layer deposition metal oxide for high performance anodes. *J. Mater. Chem. A* **5**, 12297–12309 (2017).

58. Kozen, A. C., Lin, C. F., Pearse, A. J., Schroeder, M. A., Han, X., Hu, L., Lee, S. B., Rubloff, G. W. & Noked, M. Next-Generation Lithium Metal Anode Engineering via Atomic Layer Deposition. *ACS Nano* **9**, 5884–5892 (2015).

59. Chen, L., Chen, K. S., Chen, X., Ramirez, G., Huang, Z., Geise, N. R., Steinrück, H. G., Fisher, B. L., Shahbazian-Yassar, R., Toney, M. F., Hersam, M. C. & Elam, J. W. Novel ALD Chemistry Enabled Low-Temperature Synthesis of Lithium Fluoride Coatings for Durable Lithium Anodes. *ACS Appl. Mater. Interfaces* **10**, 26972–26981 (2018).

60. Yuan, Y., Wu, F., Bai, Y., Li, Y., Chen, G., Wang, Z. & Wu, C. Regulating Li deposition by constructing LiF-rich host for dendrite-free lithium metal anode. *Energy Storage Mater.* **16**, 411–418 (2019).

61. Yildirim, H., Kinaci, A., Chan, M. K. Y. & Greeley, J. P. First-Principles Analysis of Defect Thermodynamics and Ion Transport in Inorganic SEI Compounds: LiF and NaF. *ACS Appl. Mater. Interfaces* **7**, 18985–18996 (2015).

62. Jing, H. K., Kong, L. L., Liu, S., Li, G. R. & Gao, X. P. Protected lithium anode with porous Al_2O_3 layer for lithium-sulfur battery. *J. Mater. Chem. A* **3**, 12213–12219 (2015).

63. Kim, Y., Koo, D., Ha, S., Jung, S. C., Yim, T., Kim, H., Oh, S. K., Kim, D. M., Choi, A., Kang, Y., Ryu, K. H., Jang, M., Han, Y. K., Oh, S. M. & Lee, K. T. Two-Dimensional Phosphorene-Derived Protective Layers on a Lithium Metal Anode for Lithium-Oxygen Batteries. *ACS Nano* **12**, 4419–4430 (2018).

64. Krauskopf, B., Otto, S., Moryson, Y., Hoffmann, F., Sann, J. & Janek, J. Thin and Homogenous Surface Functionalization of Lithium Metal Anodes by Defined Molecular Treatment. *J. Electrochem. Soc.* **170**, 030537 (2023).

65. Zhu, B., Jin, Y., Hu, X., Zheng, Q., Zhang, S., Wang, Q. & Zhu, J. Poly(dimethylsiloxane) Thin Film as a Stable Interfacial Layer for High-Performance Lithium-Metal Battery Anodes. *Adv. Mater.* **29**, 2–7 (2017).

66. Li, Q., Zeng, F. L., Guan, Y. P., Jin, Z. Q., Huang, Y. Q., Yao, M., Wang, W. K. & Wang, A. B. Poly (dimethylsiloxane) modified lithium anode for enhanced performance of lithium-sulfur batteries. *Energy Storage Mater.* **13**, 151–159

(2018).

67. Takehara, Z., Ogumi, Z., Uchimoto, Y., Yasuda, K., Yoshida, H. Modification of lithium/electrolyte interface polymerization of 1,1-difluoroethene. *J. Power Sources* **44**, 377–383 (1993).

68. Takehara, Z. Future prospects of the lithium metal anode. *J. Power Sources* **68**, 82–86 (1997).

69. Kozen, A. C., Lin, C. F., Zhao, O., Lee, S. B., Rubloff, G. W. & Noked, M. Stabilization of Lithium Metal Anodes by Hybrid Artificial Solid Electrolyte Interphase. *Chem. Mater.* **29**, 6298–6307 (2017).

70. Chen, L., Huang, Z., Shahbazian-Yassar, R., Libera, J. A., Klavetter, K. C., Zavadil, K. R. & Elam, J. W. Directly Formed Alucone on Lithium Metal for High-Performance Li Batteries and Li-S Batteries with High Sulfur Mass Loading. *ACS Appl. Mater. Interfaces* **10**, 7043–7051 (2018).

71. Kamphaus, E. P., Angarita-Gomez, S., Qin, X., Shao, M., Engelhard, M. H., Mueller, K. T., Murugesan, V. & Balbuena, P. B. Role of inorganic surface layer on solid electrolyte interphase evolution at Li-metal anodes. *ACS Appl. Mater. Interfaces* acsami.9b07587 (2019) doi:10.1021/acsami.9b07587.

72. Leskelä, M. & Ritala, M. Atomic layer deposition (ALD): From precursors to thin film structures. *Thin Solid Films* **409**, 138–146 (2002).

73. Tsyganenko, A. A., Manoilova, O. V., Bulanin, K. M., Storozhev, P. Y., Haukka, S., Palukka, A. & Lindblad, M. Study of layer-by-layer growth of silica on alumina and alumina on silica using IR spectroscopy of adsorbed CO. *Stud. Surf. Sci. Catal.* **130 D**, 3149–3154 (2000).

74. Mikko Ritala & Markku Leskela. Atomic layer epitaxy--a valuable tool for nanotechnology? *Nanotechnology* **10**, 19–24 (1999).

75. Qin, C., Cao, J., Chen, J., Dai, G., Wu, T., Chen, Y., Tang, Y., Li, A. & Chen, Y. Improvement of electrochemical performance of nickel rich $LiNi_{0.6}Co_{0.2}Mn_{0.2}O_2$ cathode active material by ultrathin TiO_2 coating. *Dalt. Trans.* **45**, 9669–9675 (2016).

76. Johnson, R. W., Hultqvist, A. & Bent, S. F. A brief review of atomic layer deposition: From fundamentals to applications. *Mater. Today* **17**, 236–246 (2014).

77. Mallick, B. C., Hsieh, C.-T., Yin, K.-M., Gandomi, Y. A. & Huang, K.-T. Review—On Atomic Layer Deposition: Current Progress and Future Challenges. *ECS J. Solid State Sci. Technol.* **8**, N55–N78 (2019).

78. Friedrich, J. Mechanisms of Plasma Polymerization – Reviewed from a Chemical Point of View. **8**, 783–802 (2011).

79. A. Westwood. Glow discharge polymerization--i. *Eur. Polym. J.* **7**, 363–375 (1971).

80. Denaro, A. R., Owens, P. A. & Crawshaw, A. Glow discharge polymerization-styrene. *Eur. Polym. J.* **4**, 93–106 (1968).

81. Yasuda, H. & Hirotsu, T. Critical Evaluation of Conditions of Plasma Polymerization. *J Polym Sci Polym Chem Ed* **16**, 743–759 (1978).

82. Hegemann, D., Steele, D. A. & Short, R. D. Editorial: Joint commentary to the debate. *Plasma Process. Polym.* **7**, 365 (2010).

83. Kumar, A., Al-Jumaili, A., Bazaka, K., Mulvey, P., Warner, J. & Jacob, M. V. In-

Situ surface modification of terpinen-4-ol plasma polymers for increased antibacterial activity. *Materials (Basel).* **13**, 1–13 (2020).

84. Macgregor, M. & Vasilev, K. Perspective on Plasma Polymers for Applied Biomaterials Nanoengineering and the Recent Rise of Oxazolines. *Materials (Basel).* **12**, 191 (2019).

85. Yasuda, H. & Gazicki, M. Biomedical applications of plasma polymerization and plasma treatment of polymer surfaces. **3**, 68–77 (1982).

86. Rohnke, M., Janek, J., Kilner, J. A. & Chater, R. J. Surface oxygen exchange between yttria-stabilised zirconia and a low-temperature oxygen rf-plasma. *Solid State Ionics* **166**, 89–102 (2004).

87. Meiss, S. A., Rohnke, M., Rettig, F., Moos, R. & Janek, J. Ion-conducting probes for low temperature plasmas. *Contrib. to Plasma Phys.* **48**, 473–479 (2008).

88. Vickerman, J. C. & Gilmore, I. S. *Surface Analysis - The Principal Techniques: Second Edition*. *Surface Analysis - The Principal Techniques: Second Edition* (2009). doi:10.1002/9780470721582.

89. Yu, X. -R & Hantsche, H. Vertical differential charging in monochromatized small spot X-ray photoelectron spectroscopy. *Surf. Interface Anal.* **20**, 555–558 (1993).

90. Ogumi, Z., Uchimoto, Y. & Takehara, Z. Ionically Conductive Thin Polymer Film Prepared by Plasma Polymerization: I . Hybrid Film of Plasma Polymer Formed from Octamethylcyclotetrasiloxane, Poly(propylene oxide), and Lithium Perchlorate. *J. Electrochem. Soc.* **136**, 625–630 (1989).

7. Appendix

7.1 Supporting Information

7.1.1 Publication 1

Supporting Information

Analyzing nm-thin cathode particle coatings for lithium-ion batteries – The example of TiO_2 on NCM622

Yannik Moryson[a,b], Felix Walther[a,b], Joachim Sann[a,b], Boris Mogwitz[a,b], Shamail Ahmed[d], Simon Burkhardt[a, b], Limei Chen[e], Peter J. Klar[e], Kerstin Volz[d], Sarah Fearn[c], Marcus Rohnke[a,b *], Jürgen Janek[a,b *]

[a]*Institute of Physical Chemistry, Justus Liebig University Giessen, Heinrich-Buff-Ring 17, D-35392 Giessen, Germany*

[b]*Center for Materials Research (LaMa), Justus Liebig University Giessen, Heinrich-Buff-Ring 16, D-35392 Giessen, Germany*

[c]*Department of Materials, Imperial College London, Exhibition Road, SW7 2AZ, London, UK*

[d]*Materials Science Centre and Faculty of Physics, Philipps University Marburg, Hans-Meerwein-Strasse 6, D-35043 Marburg, Germany*

[e]*Institute of Experimental Physics I, Justus Liebig University Giessen, Heinrich-Buff-Ring 16, D-35392 Giessen, Germany*

Corresponding Authors:

* E-Mail: Marcus.Rohnke@phys.chemie.uni-giessen.de, Juergen.Janek@phys.chemie.uni-giessen.de

In **Figure S1**, the SE image and EDX mapping of a coated NCM622 cross-section are shown. The image quality is influenced by charging effects and also shadowing because of the EDX detector position. All in all, EDX can be used to identify Ti around the particles but the quality is not good enough to use a FIB-EDX analysis as definite proof for a successful coating.

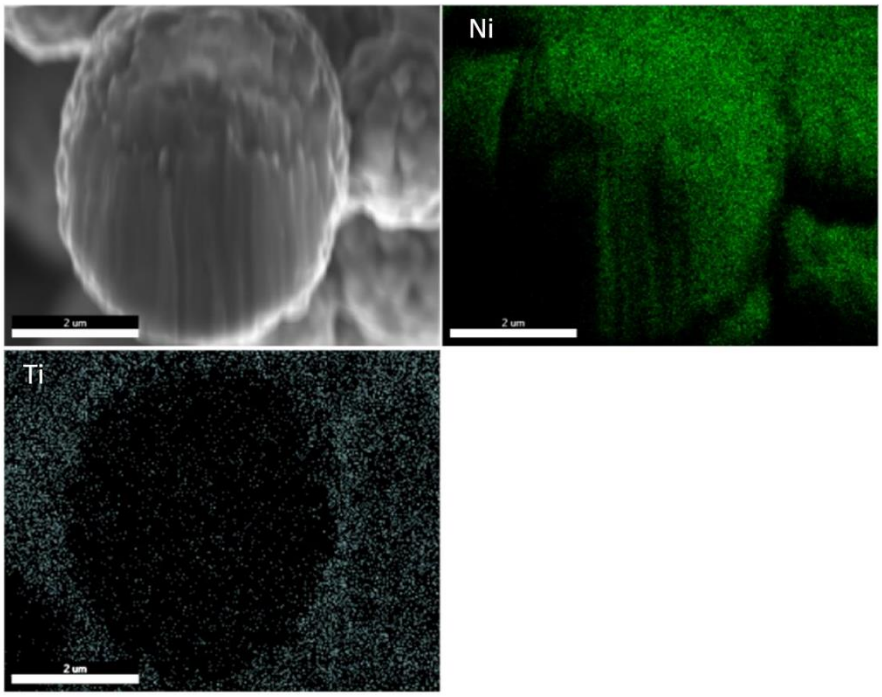

Figure S1: SE image and EDX Mapping of Ni and Ti of the NCM particle cross-section. While Ni can be detected on the whole particle, Ti is only visible around the particle and not in the cross-section.

Figure S2 shows the BSE image of TiO_2 coated NCM851005 particles. At a first glance, one could identify the brighter part as the coating layer but it consists of redeposition products due to the FIB process. The bright layer is also too thick to represent the coating. Interpretation of FIB-SEM images requires care, and needs to be complemented by other techniques.

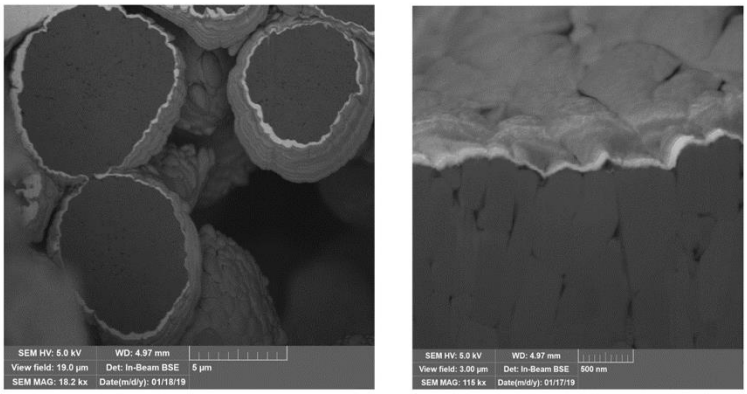

Figure S2: BSE images of the cross-section of TiO_2 coated NCM851005 particles. The big contrast difference is misleading and not showing the original coating layer. It is a layer which formed due to redeposition during the FIB process, because the thickness is considerable too thick for a coating layer.

Figure S3 shows a sketch of coated NCM primary particles after the ALD process. Depending on the position and tilt of the primary particles in the secondary particle structure different coating thicknesses result. It is also possible that some primary particles or areas of primary particles are not coated at all because of missing surface contacts.

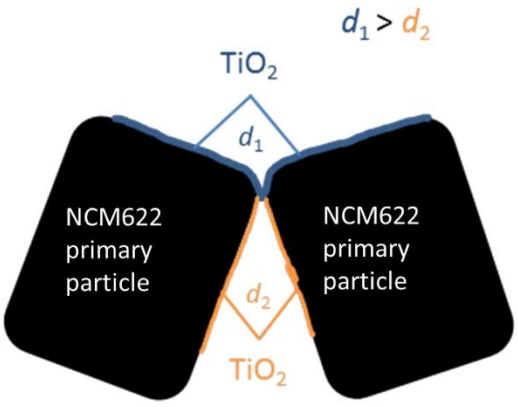

Figure S3: Sketch of the NCM primary particles after the coating process. Depending on their position and tilt in the secondary particle structure different coating thicknesses can result. Primary particles with no surface contact are not being coated.

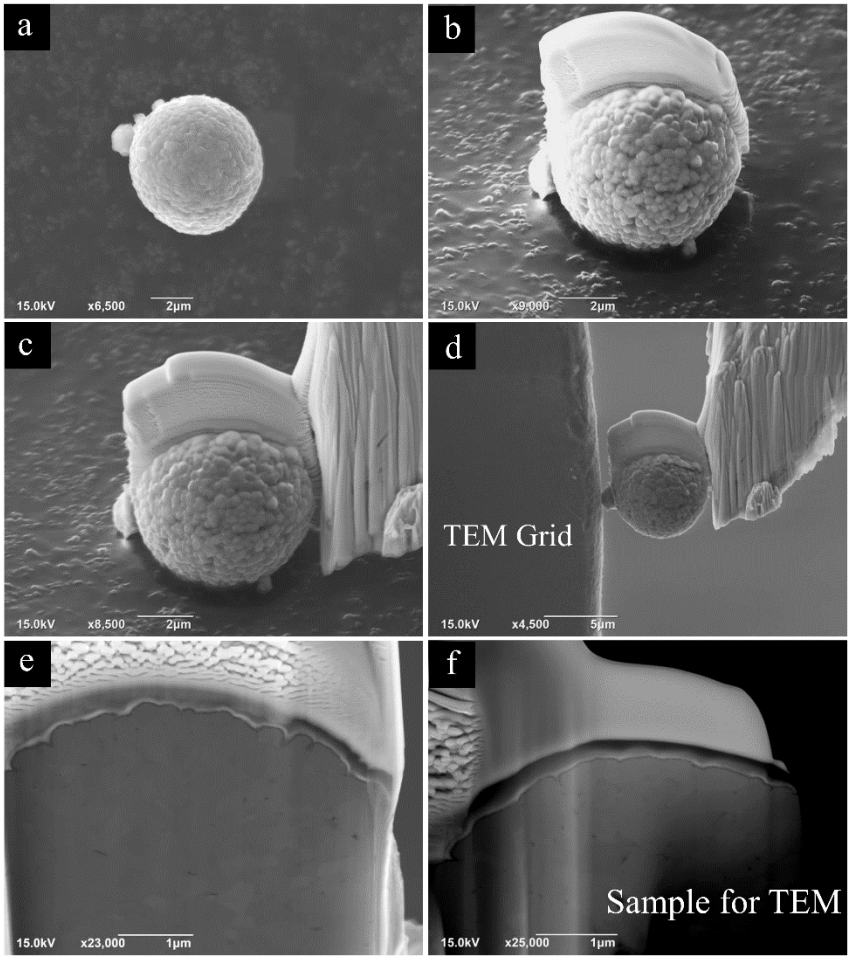

Figure S4: SEM secondary electron images, (a) coated secondary particle, (b) coated secondary particles protected with surface protection layers, (c) particle attached to FIB micro-manipulator needle, (d) particle being attached to TEM grid, (e) cross-section of the secondary particle and (f) sample for TEM analysis.

In Figure S5 (a) the XPS detail spectra of C1s of all samples are shown. The carbon signal decreases with increasing ALD cycles. Only the C1s component which was used for calibration is shown. In Figure S5 (b) the Cl 2p spectrum from the survey spectrum of the 50 ALD cycles sample is shown. The binding energy of the Cl 2p peak is at the position for metal chlorides.

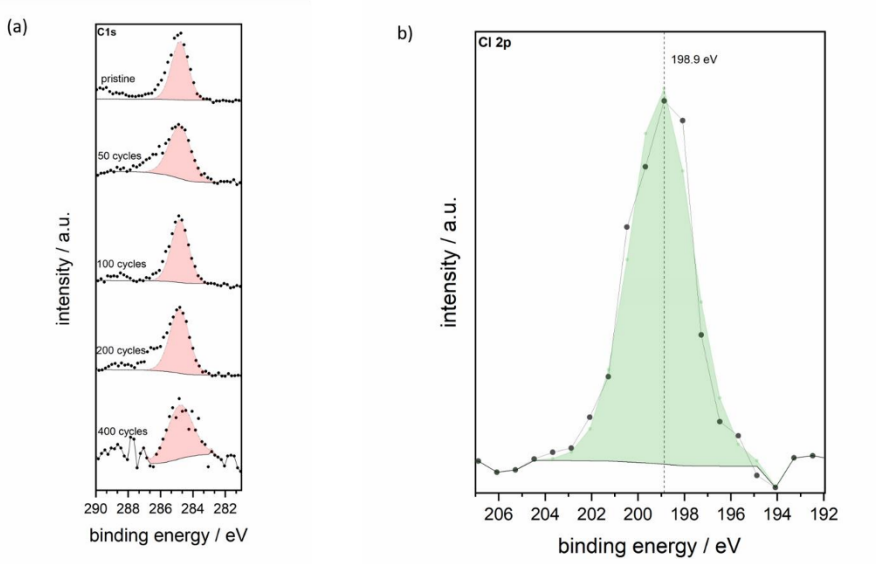

Figure S5: XPS detail spectra of C1s of the different samples (a) and Cl 2p spectrum from the survey spectrum of the 50 ALD cycles sample (b). Only the C1s component which was used for calibration is shown in (a).

In **Figure S6** the different sample preparation methods for ToF-SIMS and their results are depicted schematically. The easiest method is to attach the particles to a copper tape, which is shown in A). But this preparation technique has several disadvantages. Firstly, the particles can fly into the analyzer and secondly because of the valleys between the particles different heights are analyzed at the same time resulting in information from deeper regions projeceted to the top. If depth profiling is executed on attached particles, this will result in triangle formation, which is shown in B), due to the formation of preferred surface orientations. The coating will also be destroyed before it can be analyzed. The second preparation method is to press the particles into a pellet, which is shown in C). This will lead to improved results compared to A), because the void between the particles are reduced. However, the particles will be mechanically damaged and cracks in the coating result. The most promising sample preparation method is to embed the particles in an embedding material, as depicted in D). In the ideal case,

embedding material and sample have the same sputter yield and no differential sputtering is observed. E) depicts a situation, in which the sputter yield of the embedding material is much larger compared to the sputter yield of the coated CAM.

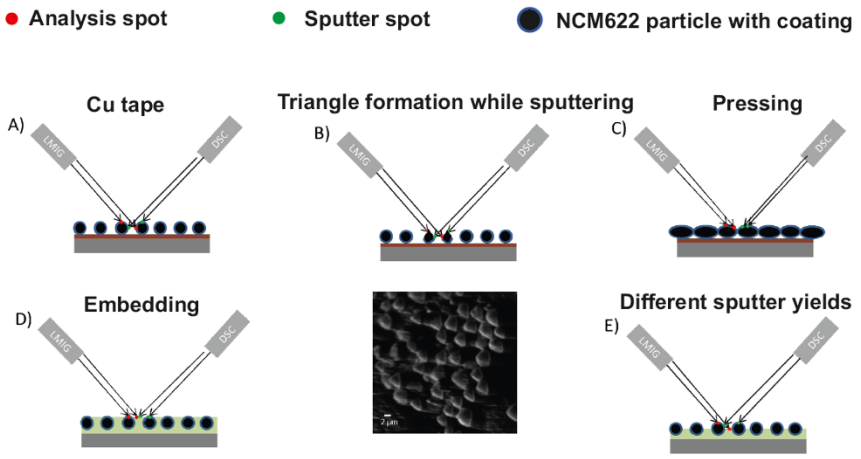

Figure S6: Illustration of different sample preparation methods for ToF-SIMS and challenges. A) Attaching particles to a Cu tape, which leads to analysis in different heights. B) Triangle formation while sputtering due to formation of preferred surface orientations. SE image of the triangle formation. C) Pressing of particles, which improves imaging in different heights, but deforms the particles. D) Embedding of the particles in an embedding material, which leads to imaging within a horizontal plane. E) A greater sputter yield of the embedding material compared to the particles leads to A) and finally B).

Figure S7 shows the sputter rates of the different mixing ratios for Technovit 4004. The sputter rate gets smaller with an increasing amount of powder. As a reference, a Si-Wafer was also sputtered. To get a sputter rate as low as for the Si-Wafer, a ratio of almost 3:1 of powder and liquid would be required. Since a ratio larger than 2:1 leads to a comparably high viscosity of the polymer, the handling becomes unpractical and is therefore not recommended.

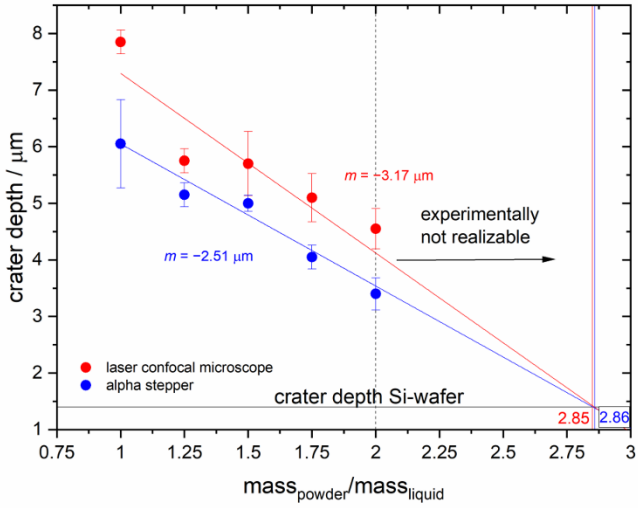

Figure S7: Sputter depth vs. mass ratio of Technovit 4004 powder and liquid. The crater depths (Cs^+ 2 keV, 200 µm x 200 µm, 900 s, 451 sputter frames) were measured by an optical profilometer (red) and an alpha stepper (blue). As a reference, the crater depth under the same conditions in a Si-Wafer is given. The experiment shows that the sputter rate of Technovit 4004 can be tailored by the mixing ratio of the two compounds but is still much higher than the sputter yield of the used particles, which is comparable to SiO_2.

7.1.2 Publication 2

Supporting Information

In-Depth Characterization of Lithium Metal Surfaces with XPS and ToF-SIMS: Toward better Understanding of the Passivation Layer

Svenja-K. Otto [a], Yannik Moryson [a], Thorben Krauskopf [a], Klaus Peppler [a], Joachim Sann [a], Jürgen Janek [a,b] and Anja Henss [a,b] *

[a] *Institute of Physical Chemistry, Justus-Liebig-Universität Giessen, Heinrich-Buff-Ring 17, D-35392 Giessen, Germany*

[b] *Center for Materials Research (LaMa), Justus-Liebig-Universität Giessen, Heinrich-Buff-Ring 16, D-35392 Giessen, Germany*

* E-Mail: anja.henss@phys.chemie.uni-giessen.de

This PDF file includes:

S1: Characterization of reference samples with XPS

To enable the identification of the different compounds on the lithium samples, we analyzed reference samples of several lithium compounds. Since XPS is one of the most common characterization methods for the investigation of lithium metal anodes, the binding energies for common lithium compounds have been reported by many authors and were for example reviewed by Wood *et al.* in 2018.[1] In their publication, the authors discuss that charging during the XPS measurements is the main reason for the wide spread of the reported absolute XPS core level binding energies. They used the separations between different core levels and the valence band of the different compounds to define a set of binding energies for lithium compounds. In addition to this report, we analyzed the lithium compounds LiOH, Li_2O_2, Li_2CO_3, Li_2O and LiH as reference samples, to determine the absolute binding energies for our study, *i.e.* for our XPS instrument. Besides, to clean the compounds and to evaluate their stability against Ar^+-sputtering, depth profiles were measured. The carbon contaminations were removed through sputtering. Also, LiOH, Li_2O_2 and Li_2CO_3 partly decomposed to Li_2O, as reported previously.[2,3] The influence of this decomposition on the investigation of lithium samples is discussed in S3. The decomposition was more pronounced for Li_2O_2 and LiOH than for Li_2CO_3. Furthermore, a little amount of carbide formed on the Li_2CO_3 sample through sputtering. The Li_2O sample was sputter cleaned without any sights of decomposition. For LiH, the carbonate and hydroxide peaks in the O 1 s region vanished completely through sputtering and only the oxide peak remained. In the Li 1s region a peak evolved at 52.6 eV and plasmon-loss features appeared. These observations indicate the formation of lithium metal. Possibly LiH decomposes to Li and H_2 through sputtering. Therefore, no Li 1s binding energy for LiH was determined. The O 1s and Li 1s binding energies for the other measured lithium compounds are summarized in Figure S1. We like to emphasize that the absolute values can vary due to charging, as discussed above.[1] Nevertheless, the relative positions of the different compounds do not change and were used by us for the interpretation of XPS spectra. The Li 1s binding energy for lithium metal is also shown in Figure S1. The value was determined from depth profiles of lithium foils.

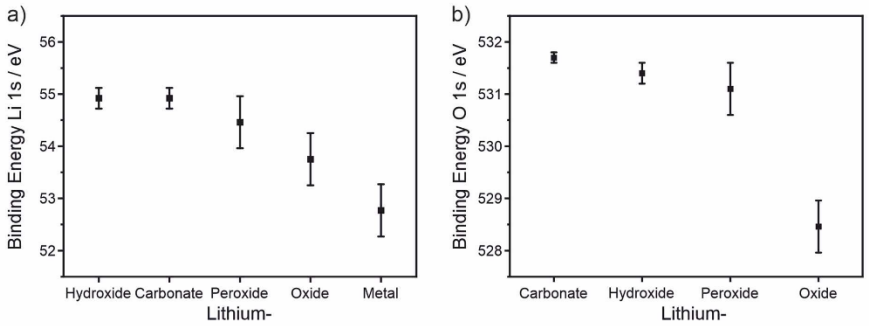

Figure S1. a) Li 1s and b) O 1s binding energies of lithium compounds and lithium metal. The sigma values are displayed as error bars. The error of the values for lithium oxide was applied to the values for lithium metal and peroxide, as the oxide signal was used for calibration of the corresponding spectra.

S2: XPS depth profiling

On the surface of all lithium samples (before sputtering), peaks were observed at 531.7 eV for O 1s and at 54.6 eV for Li 1s. These values fit in general with the ones determined for LiOH, Li_2CO_3 and Li_2O_2, as well as with common surface adsorbates. However, the existence of Li_2O_2 is unlikely, as the peroxide is thermodynamically unstable against lithium metal. Therefore, Li_2O_2 is not taken into further account. Apart from this assumption, LiOH and Li_2O_2 are hard to distinguish in the XPS by just evaluating the O 1s and Li 1s spectra. Even though the binding energies for Li_2CO_3 and LiOH are also very similar, the

compounds can be fitted with separate peaks using an area constraint from the C 1s carbonate peak for the corresponding O 1s and Li 1s peaks. Surface adsorbates were minimized by always keeping the samples under inert gas or vacuum and were neglected as the fit quality was satisfying without considering them. Adventitious carbon was detected on the surface and removed through sputtering. After longer sputtering, the formation of minor amounts of carbide was observed. Schmitz *et al.* highlighted Li_2C_2 as important surface and bulk contamination of battery grade lithium metal based on Raman, MS, ICP-OES and EDX analyses.[4] Nevertheless, Ar^+-sputtering of metal carbonates or oxides with carbon contaminations is known to induce the formation of carbides. Therefore, carbide is not regarded as a component of the passivation layer but as a decomposition product of carbon from different sources. This interpretation is in accordance with previous XPS studies.[4,5] After the first sputter cycle, additional peaks at lower binding energy appeared for the O 1s and Li 1s regions. These peaks were attributed to Li_2O (528.5 eV for O 1s and 53.8 eV for Li 1s). With longer sputter time, the carbonate vanished completely, the intensity of the hydroxide peak dropped significantly and the oxide peak intensity became virtually stable. At the same time, another peak at even lower binding energy evolved in the Li 1 s region (52.6 eV). The peak came with plasmon-loss features at around 60 eV, which is a clear indication for lithium metal.

The residual standard deviations (STDs) of all fits were between 1 and 2 for the Li 1s and O 1s regions. These values are sufficiently low to guarantee that no major fraction of other compounds, such as LiH, was probed, but minor amounts in the range of the quantification error cannot be ruled out. The quantification error was estimated to be +/- 5 at% and is dominated by the low sensitivity of XPS towards Li. It is worth mentioning that the STD is a measure for the mathematical fit quality and a low value does not ensure that the sample composition is determined correctly, as the physicochemical model underlying the fit is more important. Also, it should be emphasized that oxidation of lithium metal during measurement and decomposition of lithium compounds through sputtering influence the quantitative results and the accuracy of the fit. Still, since the carbonate vanished completely, the compound can only be present on the sample surface. The LiOH fraction was most likely reduced through decomposition (see S3) and the fraction of lithium metal decreased through reactions. It is also important to note that the spectra were measured after each other and therefore represent different reaction states, what influences the accuracy of the fit which is based on area constraints, too.

S3: Decomposition by argon sputtering

In order to evaluate the influence of argon sputtering and the extent of sputter-induced decomposition during depth profiling of the lithium foils, the decomposition by argon sputtering was evaluated on reference compounds and compared to the lithium samples. As mentioned before, LiOH and Li_2CO_3 were identified on the lithium foil (S2) and were found to decompose partly to Li_2O by argon sputtering (S1). Pure carbonate was observed on the surface of the Li_2CO_3 reference sample (Figure S2a). After two sputter intervals of 3 min at 1 kV and 8 min at 2 kV, the composition changed to about 79% carbonate and 21% oxide. For the LiOH reference sample (Figure S2b), some carbonate contamination was observed on the surface. Neglecting the carbonate and its decomposition to obtain the highest possible degree of hydroxide decomposition, the same sputtering steps yield 59% hydroxide and 41% oxide. However, for a lithium sample 17% hydroxide and 83% oxide were observed after the same sputter steps under the same conditions. Even the calculated maximum degree of decomposition of hydroxide cannot explain this ratio, what leaves an oxide-rich region under the carbonate and hydroxide passivation layer as most likely explanation. Please note that sputter steps were chosen which do not lead to lithium metal for the lithium sample, so that the reactivity of lithium metal does not need to be considered for this comparison. Also, the ratio of hydroxide to oxide always shifted towards a higher hydroxide fraction during these XPS measurements. Accordingly, detrimental reactions cannot explain the observed excess oxide fraction. However, the decomposition by sputtering is an important factor which underlines that conclusions based on absolute quantification are not valid for the discussed measurements. Although other groups published nondestructive methods to probe lithium-containing

samples, for example by using high-energy photons to increase the XPS probing depth[6], our approach has the advantage that most XPS machines are capable of such measurements.

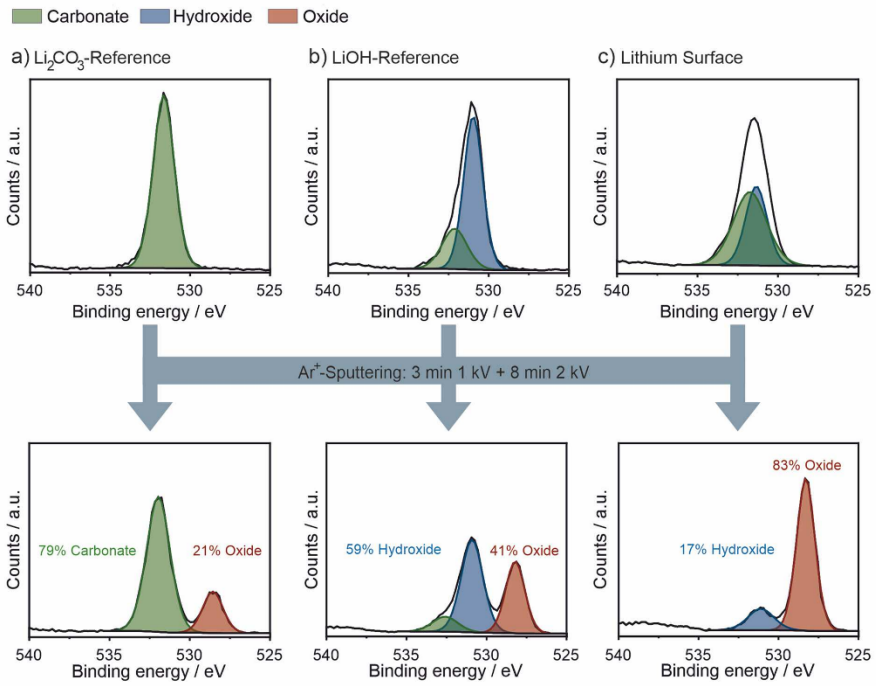

Figure S2: Comparison of the decomposition induced by argon sputtering (3 min at 1 kV and 8 min at 2 kV) for a) a Li_2CO_3-reference, b) a LiOH-reference and c) a lithium surface. The oxide fraction on the lithium sample after sputtering cannot be explained only by the degree of decomposition which was observed on the reference samples. The given numbers are atom fractions of the examined lithium compounds.

S4: Characterization of reference samples with ToF-SIMS

To identify secondary ions that are specific for the different lithium compounds, the reference samples LiOH, Li_2O_2, Li_2CO_3, Li_2O and LiH were investigated with ToF-SIMS, similarly as reported for other lithium containing samples.[7] In a first step, depth profiles of pressed pellets were analyzed to distinguish between signals originating from contaminations and from the reference compound. Signals with rising or constant intensity in the depth profile were regarded as potentially specific; signals with decreasing intensity were defined as contaminants. Depth profiles for characterization of the reference samples were performed on pressed pellets in spectrometry mode. Bi^+ primary ions (25 kV, 1.2 pA, 100x100 µm²) and Ar_{1500}^+ sputter ions (10 kV, 10 nA, 300x300 µm²) were used. For charge compensation a flood gun with an energy of 21 eV and a current of 10 µA was used. Between two sputter frames, analysis was done after 2 s of waiting time, in random raster mode, measuring 2 frames with 128x128 pixels and 1 shot/pixel. In a second step, ToF-SIMS spectra of the sputter-cleaned samples were measured with a defined ion dose density. The potentially specific signals, which showed highest intensity in comparison to all other investigated compounds, were defined as specific for the

corresponding lithium compound. Spectra of the reference samples were measured after sputter cleaning with Ar_{1500}^+ using a dose density of $4 \cdot 10^{15}$ ions/cm^2. For each sample, 12 areas of 100x100 µm^2 were measured with a primary ion dose of 10^{12} ions/cm^2. To compare the secondary ion signal intensities of different compounds, the average intensity of all areas from one compound was taken. As error, the standard deviation was calculated. The procedure is shown for the secondary ion Li_2H^- as a specific signal for LiH in Figure S3. The specific signals, which were used for the interpretation of the depth profiles, are summarized in Table S1. They were chosen because they do not overlap with other peaks. Other related secondary ions which showed similar profiles and were used as group of specific signals are also given. It is important to note that signals, which are discussed as specific for one compound, may also be quite intense for another one. Consequently, the intensity of the signal can be high even though the corresponding compound is only present in minor amounts.

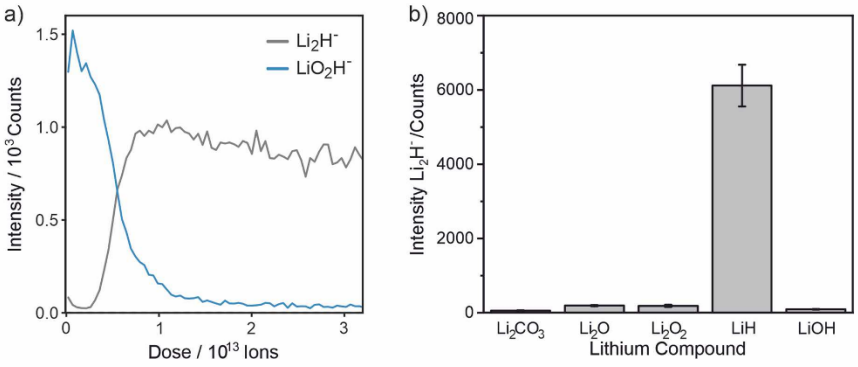

Figure S3. Example for the classification of a specific secondary ion for a lithium compound: a) Depth profile of the LiH pellet. The signal intensity of LiO_2H^- dropped, while the intensity of Li_2H^- increased with sputtering. Therefore, Li_2H^- was identified as a potentially specific secondary ion for LiH, whereas LiO_2H^- was regarded as originating from a surface contamination of the sample. b) Comparison of the signal intensity of Li_2H^- for all spectra measured on sputter-cleaned pellets of the reference compounds with the same ion does density: The intensity is highest for the LiH sample. Consequently, the Li_2H^- signal was classified as specific for LiH.

Table S1. Representative specific secondary ions which were used for the interpretation of the ToF-SIMS depth profiles and other specific signals with similar profiles.

Compound	**Specific signal(s) negative polarity**	**Related signal(s)**	**Specific signal(s) positive polarity**	**Related signal(s)**
Hydrocarbons	C_2H^-	CH_2^-, CH^-,$C_2H_3^-$, CH_3^-, C_3H^-, $C_3H_2^-$	$C_3H_3^+$	CH^+, CH_2^+, CH_3^+, $C_2H_3^+$
Carbonate	CO_3^-	$LiCO_3^-$		
Hydroxide	OH^- and LiO_2H^-	HO_2^-, $LiO_2H_2^-$	Li_2OH^+ and $LiOH^+$	$LiOH_2^+$
Oxide	O^- and LiO^-	LiO_2^-	Li_2O^+	LiO^+
Hydride	LiH_2^-	$^6LiH^-$, LiH^-, Li_2H^-	Li_2H^+	$^6LiLiH^+$

S5: ToF-SIMS depth profiling

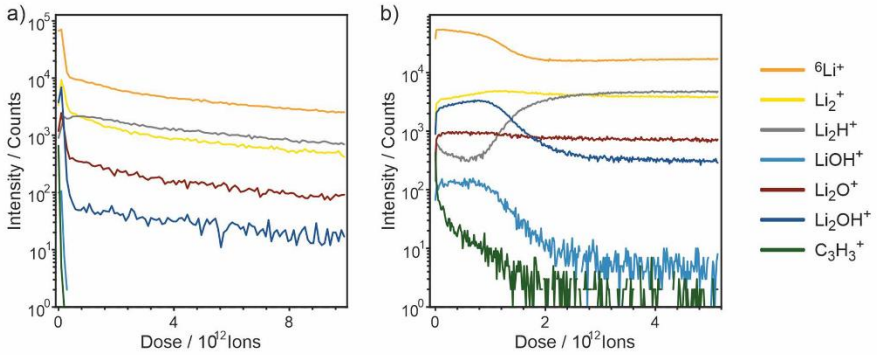

Figure S4. ToF-SIMS depth profiles of lithium foil 1 as-received measured in (spectrometry) positive ion mode. The unspecific secondary ions $^6Li^+$ and Li_2^+ are shown to visualize that all signal intensities drop for higher sputter dose.

Other elements than Li, C, O and H, which could be identified in the negative mode ToF-SIMS spectra of lithium foils, are P, F, S, Cl, Br and N. In the positive ion mode Mg, K, Si, Na, Ca and Fe were identified as additional trace elements.

S6: Determination of sputter rates with ToF-SIMS

In order to access sputter rates of lithium and lithium compounds, sputter craters were prepared with defined sputter doses. Sputter rates and yields were calculated from the sputter time and current that were necessary to prepare the craters. The depth of the sputter craters ranged from 5 to 15 µm. 3 to 5 craters were prepared on as received lithium foil for each sputter species, namely for Cs^+ (2 keV – 190 nA), Ar^+ (1 keV – 210 nA), Ar_{750}^+ (10 keV – 9 nA), and Ar_{1500}^+ (10 keV – 10 nA). The rates for sputtering lithium compounds were determined with Ar_{1500}^+ (10 keV – 10 nA) by preparing 2 craters on pressed pellets. The crater size was 300x300 µm^2 in all cases. The depth of the craters was measured with a profilometer (Alpha-Step IQ Surface Profiler, KLA Tencor) under argon atmosphere. The obtained sputter rates and yields for the different sputter species are given in Figure S5. In literature some estimates for the sputter rates of lithium and its compounds are given[8–10], but no experimental values for lithium foils and different sputter species are reported.

For bigger argon cluster ions (Ar_{1500}^+, 10 kV, 10 nA, 300x300 µm^2) a sputter rate of about 0.15 nm/s was obtained for lithium foils, when using 100 s sputter steps. The rate was also determined for 2 s sputter steps (0.17 nm/s). Considering the error range, the sputter rates for sputter steps between 2 and 100 s can be regarded as approximately constant. For continuous sputtering a significantly higher value of 0.33 nm/s was determined, showing that the estimation cannot be applied for very long sputter steps. The given values are averages over the passivation layer and the bulk of the lithium foils. As the thickness of the passivation layer was at least two orders of magnitude smaller than the crater depth, the given sputter rates represent approximate values for the bulk lithium. The sputter rates for lithium compounds were determined for pressed pellets of the materials (Figure S5b). For Li_2CO_3 and Li_2O the sputter rate with Ar_{1500}^+ (10 kV, 10 nA, 300x300 µm^2) was about 0.25 nm/s. For LiOH a value of about 1.20 nm/s was determined. As the XPS results showed that these three compounds are the main components of the lithium foil passivation layer, an intermediate rate of 0.5 nm/s was used to estimate the thickness of the passivation layer. It is important to note that varying rates within the passivation

layer were neglected. Also, sputter rates depend on many factors, such as crystallographic orientation.[8] Consequently, the given value remains an estimate, especially as the determined thicknesses on the lithium samples are close to the depth resolution limit of the GCIB. The actual value for the sputter rate and thickness of the passivation layer could be accessed by applying AFM in combination with SIMS depth profiling. Alternatively, synchrotron-XPS measurements with varying high photon energies may be used to access detailed information about the passivation layer structure and thickness.

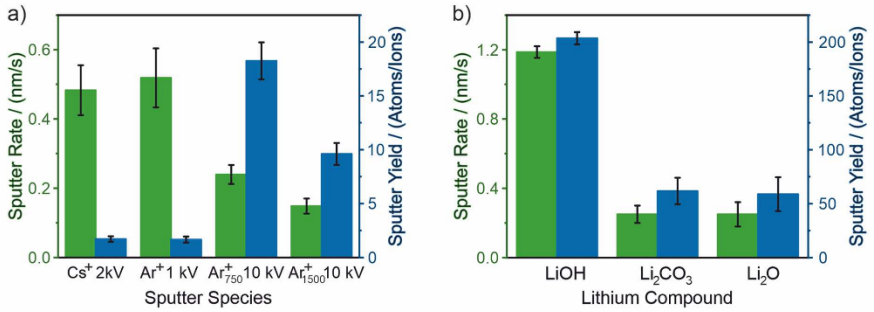

Figure S5. Sputter rates and yields for a) lithium foils with different sputter species and for b) lithium compounds with Ar_{1500}^+, 10 keV. All shown values were determined in 100 s sputter steps.

S7: ToF-SIMS imaging

While the lateral resolution is better in imaging mode, mass resolution and count rates are worse than in spectrometry mode. Consequently, it is necessary to invest longer measurement time, and signal interpretation becomes more complex. In general, mass spectra obtained in the imaging mode need to be compared with mass spectra taken in spectrometry mode and only *m/z*-regions without overlapping peaks can be used. Alternatively, single-pixel normalization of multiple *m/z*-regions, which include peaks giving the same information but overlap with other peaks, can be applied.[11]

In Figure S6 high resolution images from depth profiles of the lithium foils are shown. In most regions the passivation film was layered as described in most XPS-based literature.[12] On the very surface, a homogeneous coverage with hydrocarbon species that were quickly removed by sputtering, was detected. Below, hydroxide and oxide signals, also indicating homogeneous distribution, were more prominent. The hydroxide signal intensity decreased after a lower sputter dose than the oxide signal intensity. Beside the regions, which were homogeneously covered with the layered passivation, organic and inorganic contaminations were detected. As already found in the spectrometry mode, chemical information about the samples was easier to access in negative ion mode. For example, hydroxide contaminations were hard to visualize in the positive ion mode.

Contaminations on lithium foils are also reported in literature. For instance, Harry *et al.* used synchrotron hard X-ray micro tomography to study battery failure caused by dendrite growth and found crystalline impurities in the lithium anode that lead the nucleation of dendritic structures.[13] Similarly, Maslyn *et al.* reported, based on X-ray tomography analyses, the presence of impurity particles with diameters between 2 and 30 µm in commercial lithium metal foils.[14] With ToF-SIMS depth profiles in imaging mode, the contaminations can be visualized and chemically characterized, what allowed Meyerson et al. to identify inhomogeneously distributed organic material on a lithium anode as dominating factor for dendrite nucleation.[15]

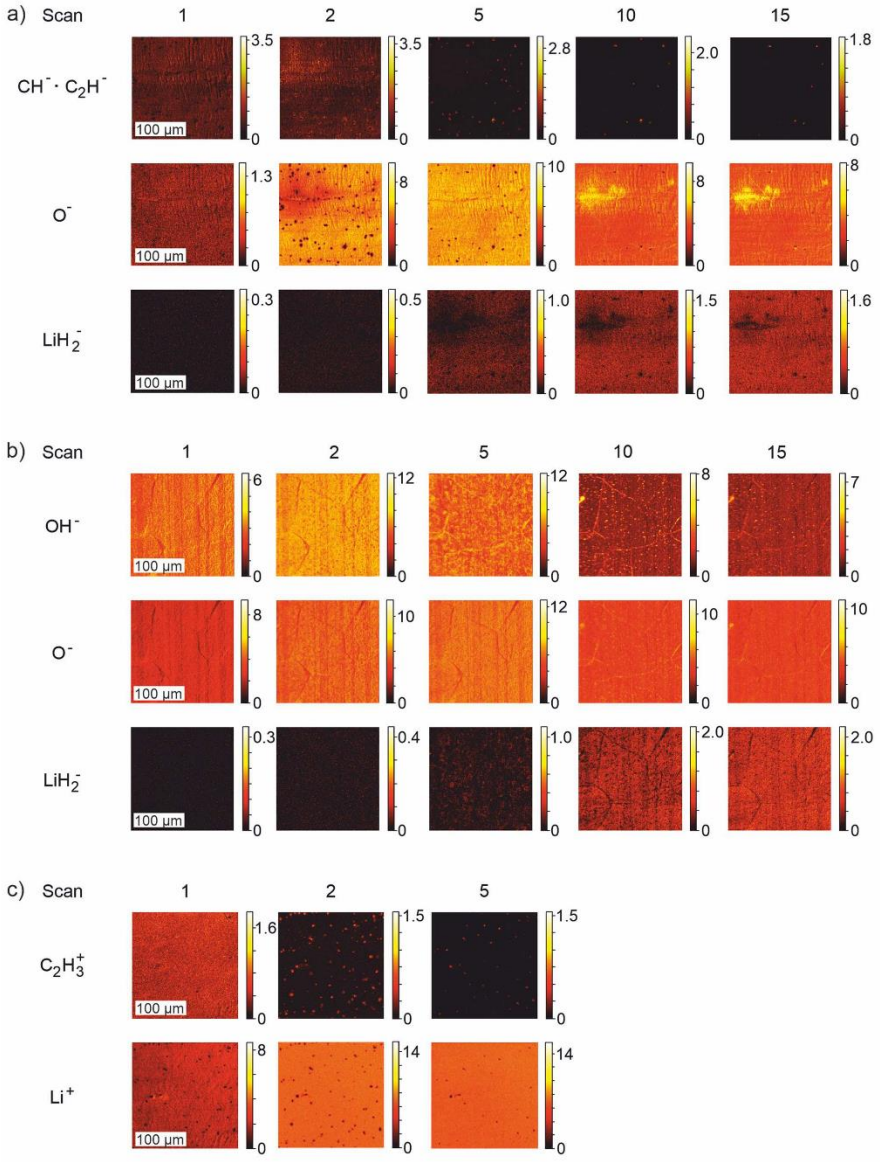

Figure S6. Single scan ToF-SIMS images of the depth profiles in imaging positive and negative ion mode. The evolution of organic contamination is shown in a) negative and c) positive ion mode. A region with hydroxide contamination is presented only in b) negative ion mode, as the information cannot be accessed properly in positive ion mode. Scan 1 shows the surface of the lithium foil before sputtering.

S8: Variation in ToF-SIMS depth profiles

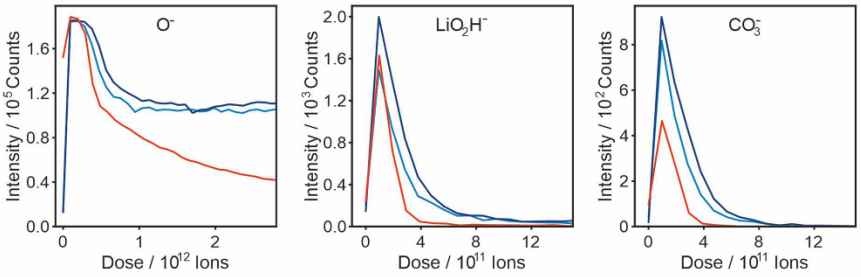

Figure S7. Homogeneity of the ToF-SIMS depth profiles measured for lithium foil 2. Two different measurements of lithium foil 2 are shown in blue. The one presented in dark blue is a representative measurement, the one in light blue an example for the possible spread of the results. For comparison, a representative measurement for lithium foil 1 is shown in red. The spread for the thinner passivated foil is not significant.

S9: EDX analysis of lithium samples with thicker passivation layers

For an electron acceleration voltage of 1 kV, the average generation depth of Li K_α emission in lithium is 47 nm, which is an order of magnitude more than the thickness of the upper surface passivation layer. Using an even lower beam energy is not resonable as the count rates become very low, and a minimum energy is needed for excitation. Consequently, the information that is accessible by EDX analysis comes mainly from deeper regions of the lithium foils than the upper passivation layer probed by XPS and ToF-SIMS. This offers the chance to get additional information on the samples and to probe thicker passivation layers, that require very long sputter time. For EDX no sputtering is necessary to probe deeper regions of the sample (static depth profile). Therefore, deeper regions are analysed in their pristine state and no unwanted reactions with the chamber atmosphere disturb the analysis like in the case of XPS after sputtering. However, it is important to note that the typical SEM chambers operate under HV conditions. Consequently, the risk of surface contamination is even higher than during XPS or SIMS analyses (UHV conditions). Furthermore, the lack of sputtering is also a drawback, since many factors influenence the analysis result at once. For example, the lateral spread of the X-ray generation also changes with the beam energy, material out of different depths is probed and all factors vary for the different elements due to their distribution and characteristic X-ray energy. Also, the sensitivity and the quantification error for lithium are unknown for the used software so far. Probably the error is quite high, as there is an intense background in the corresponding low-energy region. Defined model systems and careful data evaluation are needed to extract useful information. To show that differenes between lithium samples can be investigated with EDX, a stored lithium foil 1 is compared to an as received lithium foil 2. The results are shown in Figure S8. For every beam energy, we determined a higher lithium fraction and a lower oxygen fraction for the as received foil than for the stored one. As error the standard deviation of three measurements is given. Please note that small changes of few at% occur between successive measurements at the same spot, what is attributed to damage induced by the electron beam. We took this into account by using a new spot for each measurement and by starting the measurement immediately after reaching the spot to make the damage comparable for different samples.

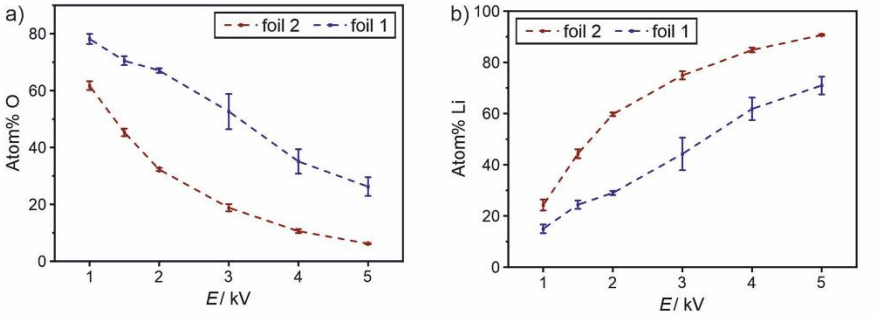

Figure S8. a) O and b) Li atomic fractions as a function of the electron beam energy determined from EDX analyses for an as received lithium foil 2 in comparison to a stored lithium foil 1.

S10: Lithium plating through ToF-SIMS measurements

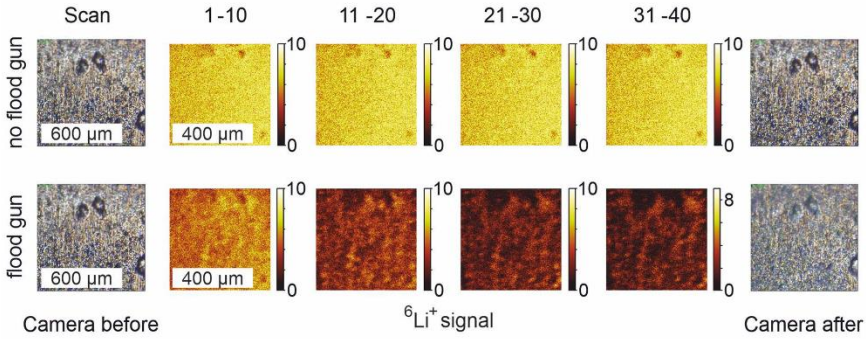

Figure S9. Lithium plating on a grounded lithium foil through electron beam exposure: comparison between spectrometry mode surface scans without (upper row) and with (bottom row) electron beam exposure using the flood gun. While the surface did not change without electron beam exposure, lithium was plated on the surface with the electron flood gun. The lithium was inhomogeneously distributed which explains the dark color of the plated lithium in the XPS camera images. Interestingly, all secondary ion intensities, such as the shown $^6Li^+$ signal intensity, decreased through the lithium plating. Only some very weak signals of trace metals, like Ni and Cu, increased. The observation indicates that the ionization probability of all lithium related secondary ions is lower for metal than for lithium compounds. Consequently, there are no specific secondary ions for lithium metal.

S11: Lithium plating through EDX measurements

EDX is used in literature to characterize for example reactions of lithium samples.[16,17] Typical EDX detectors cannot detect Li K_α emission because of its low energy. Improved EDX detectors without a vacuum window can detect elemental lithium in high concentration, as in lithium metal.[18] Lithium ions have no 2s electrons, therefore no X-ray emission takes place and lithium ions cannot be detected. As for XPS and ToF-SIMS analyses, the sample preparation can influence the results quite strongly. In Figure S10 the effect of electron neutralization on a stored lithium foil 1 prepared in electrical contact (grounded) or isolated (floating) is shown. A higher lithium metal fraction and a lower oxygen fraction

were determined for the contacted sample, what indicates that the sample changed due to lithium plating. The changes observed through this effect varied for the different samples. For example, no significant changes were observed for as received lithium foils. For the EDX measurements electron beam impact is unavoidable since the SEM electron beam causes the X-ray emission. Consequently, measuring isolated samples is the only valid option. It is important to note that isolated preparation leads to charging, especially at higher acceleration voltages.

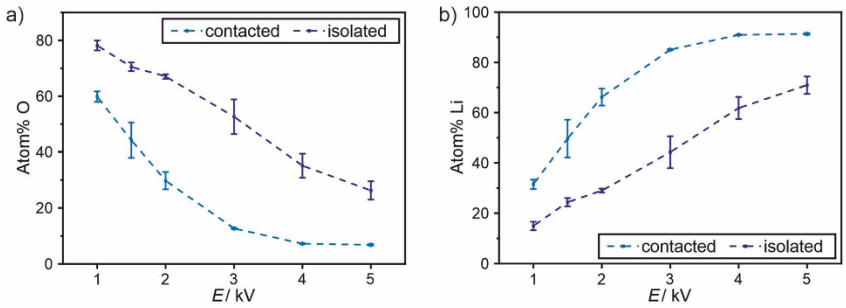

Figure S10. a) O and b) Li atomic fractions as a function of the electron acceleration voltage determined from EDX analyses for a stored lithium foil 1 prepared in electrical contact with the sample holder (grounded, light blue) or isolated from the holder (isolated, dark blue).

References

(1) Wood, K. N.; Teeter, G. XPS on Li-Battery-Related Compounds: Analysis of Inorganic SEI Phases and a Methodology for Charge Correction. *ACS Appl. Energy Mater.* **2018**, *1* (9), 4493–4504. DOI: 10.1021/acsaem.8b00406.

(2) Dedryvère, R.; Laruelle, S.; Grugeon, S.; Poizot, P.; Gonbeau, D.; Tarascon, J.-M. Contribution of X-ray Photoelectron Spectroscopy to the Study of the Electrochemical Reactivity of CoO toward Lithium. *Chemistry of Materials* **2004**, *16* (6), 1056–1061. DOI: 10.1021/cm0311269.

(3) Edström, K.; Herstedt, M.; Abraham, D. P. A new look at the solid electrolyte interphase on graphite anodes in Li-ion batteries. *Journal of Power Sources* **2006**, *153* (2), 380–384. DOI: 10.1016/j.jpowsour.2005.05.062.

(4) Schmitz, R.; Müller, R.; Krüger, S.; Schmitz, R. W.; Nowak, S.; Passerini, S.; Winter, M.; Schreiner, C. Investigation of lithium carbide contamination in battery grade lithium metal. *J. Power Sources* **2012**, *217*, 98–101. DOI: 10.1016/j.jpowsour.2012.05.038.

(5) Kanamura, K. X-Ray Photoelectron Spectroscopic Analysis and Scanning Electron Microscopic Observation of the Lithium Surface Immersed in Nonaqueous Solvents. *J. Electrochem. Soc.* **1994**, *141* (9), 2379. DOI: 10.1149/1.2055129.

(6) Ciosek Högström, K.; Malmgren, S.; Hahlin, M.; Gorgoi, M.; Nyholm, L.; Rensmo, H.; Edström, K. The Buried Carbon/Solid Electrolyte Interphase in Li-ion Batteries Studied by Hard X-ray Photoelectron Spectroscopy. *Electrochimica Acta* **2014**, *138*, 430–436. DOI: 10.1016/j.electacta.2014.06.129.

(7) Karen, A.; Ito, K.; Kubo, Y. TOF-SIMS analysis of lithium air battery discharge products utilizing gas cluster ion beam sputtering for surface stabilization. *Surf. Interface Anal.* **2014**, *46* (S1), 344–347. DOI: 10.1002/sia.5508.

(8) Bessette, S.; Paolella, A.; Kim, C.; Zhu, W.; Hovington, P.; Gauvin, R.; Zaghib, K. Nanoscale Lithium Quantification in LiXNiyCowMnZO2 as Cathode for Rechargeable Batteries. *Sci. Rep* **2018**, *8* (1), 17575. DOI: 10.1038/s41598-018-33608-3.

(9) Stark, J. K.; Ding, Y.; Kohl, P. A. Role of Dissolved Gas in Ionic Liquid Electrolytes for Secondary Lithium Metal Batteries. *J. Phys. Chem. C* **2013**, *117* (10), 4980–4985. DOI: 10.1021/jp4001303.

(10) Zu, C.; Dolocan, A.; Xiao, P.; Stauffer, S.; Henkelman, G.; Manthiram, A. Breaking Down the Crystallinity: The Path for Advanced Lithium Batteries. *Adv. Energy Mater.* **2016**, *6* (5), 1501933. DOI: 10.1002/aenm.201501933.

(11) Walther, F.; Koerver, R.; Fuchs, T.; Ohno, S.; Sann, J.; Rohnke, M.; Zeier, W. G.; Janek, J. Visualization of the Interfacial Decomposition of Composite Cathodes in Argyrodite-Based All-Solid-State Batteries Using Time-of-Flight Secondary-Ion Mass Spectrometry. *Chem. Mater.* **2019**, *31, 10*, 3745–3755. DOI: 10.1021/acs.chemmater.9b00770.

(12) Naudin, C.; Bruneel, J. L.; Chami, M.; Desbat, B.; Grondin, J.; Lassègues, J. C.; Servant, L. Characterization of the lithium surface by infrared and Raman spectroscopies. *J. Power Sources* **2003**, *124* (2), 518–525. DOI: 10.1016/S0378-7753(03)00798-5.

(13) Harry, K. J.; Hallinan, D. T.; Parkinson, D. Y.; MacDowell, A. A.; Balsara, N. P. Detection of subsurface structures underneath dendrites formed on cycled lithium metal electrodes. *Nat. Mater.* **2014**, *13* (1), 69. DOI: 10.1038/nmat3793.

(14) Maslyn, J. A.; Frenck, L.; Loo, W. S.; Parkinson, D. Y.; Balsara, N. P. Extended Cycling through Rigid Block Copolymer Electrolytes Enabled by Reducing Impurities in Lithium Metal Electrodes. *ACS Appl. Energy Mater.* **2019**, *2, 11*, 8197–8206. DOI: 10.1021/acsaem.9b01685.

(15) Meyerson, M. L.; Sheavly, J. K.; Dolocan, A.; Griffin, M. P.; Pandit, A. H.; Rodriguez, R.; Stephens, R. M.; Vanden Bout, D. A.; Heller, A.; Mullins, C. B. The effect of local lithium surface chemistry and topography on solid electrolyte interphase composition and dendrite nucleation. *J. Mater. Chem. A* **2019**, *7*, 513. DOI: 10.1039/C9TA03371H.

(16) Li, N.-W.; Yin, Y.-X.; Yang, C.-P.; Guo, Y.-G. An Artificial Solid Electrolyte Interphase Layer for Stable Lithium Metal Anodes. *Adv. Mater.* **2016**, *28* (9), 1853–1858. DOI: 10.1002/adma.201504526.

(17) Otero, M.; Lener, G.; Trincavelli, J.; Barraco, D.; Nazzarro, M. S.; Furlong, O.; Leiva, E. P. M. New kinetic insight into the spontaneous oxidation process of lithium in air by EPMA. *Appl. Surf. Sci.* **2016**, *383*, 64–70. DOI: 10.1016/j.apsusc.2016.04.060.

(18) Zachman, M.; Tu, Z.; Archer, L. A.; Kourkoutis, L. F. Nanoscale Elemental Mapping of Intact Solid-Liquid Interfaces and Reactive Materials in Energy Devices Enabled by Cryo-FIB/SEM. *ACS Energy Lett.* **2020**, *5, 4*, 1224–1232. DOI: 10.1021/acsenergylett.0c00202.

7.1.3 Publication 3

Supporting Information

Protective Coating for Lithium Metal Anode

Prepared by Plasma Polymerization

Yannik Moryson[a,b], Hannah Hartmann [a,b], Svenja-Katharina Otto [a],Xufei Fang[c], Marcus Rohnke [a,b] *, Jürgen Janek [a,b] *

[a] *Institute of Physical Chemistry, Justus Liebig University Giessen, Heinrich-Buff-Ring 17, D-35392 Giessen, Germany*

[b] *Center for Materials Research (ZfM), Justus Liebig University Giessen, Heinrich-Buff-Ring 16, D-35392 Giessen, Germany*

[c] *Department of Materials and Earth Sciences, Technical University of Darmstadt, Peter-Grünberg-Strasse 2, D-64287 Darmstadt, Germany*

Corresponding Authors:

* E-Mail: Juergen.Janek@phys.chemie.uni-giessen.de, Marcus.Rohnke@phys.chemie.uni-giessen.de,

S1 – Supporting Information 1:

In Supporting Information 1, a schematic sketch of the gas lines to the plasma reactor is shown. The reactor can be filled with Ar, N_2, $^{18}O_2$ and the polymer precursor gas or a mixture of them. The pressure and flow rate can be controlled via mass flow controllers (MFC1-3) in combination with the manometer. For operation, a LabView programm was created. Aditionally, a self-constructed transfer module (TM) was build, which can be seen in Figure S1 b). The transfer module can be filled with argon and closed with an hand valve to transport the lithium sample under air exclusion between the plasma chamber and a glovebox. Inside the TM is a *z*-axis manipulator which can be moved up and down fully motorised, see Figure S1 c) and d). This allows the respective sample to be placed in the TM and then retrieved again. In picture e) an argon-plasma with inserted TM and sample can be seen. The sketch in f) shows the resulting *E* and *B* fields due to the current flow through the copper coil around the plasma chamber glass tube.

S2

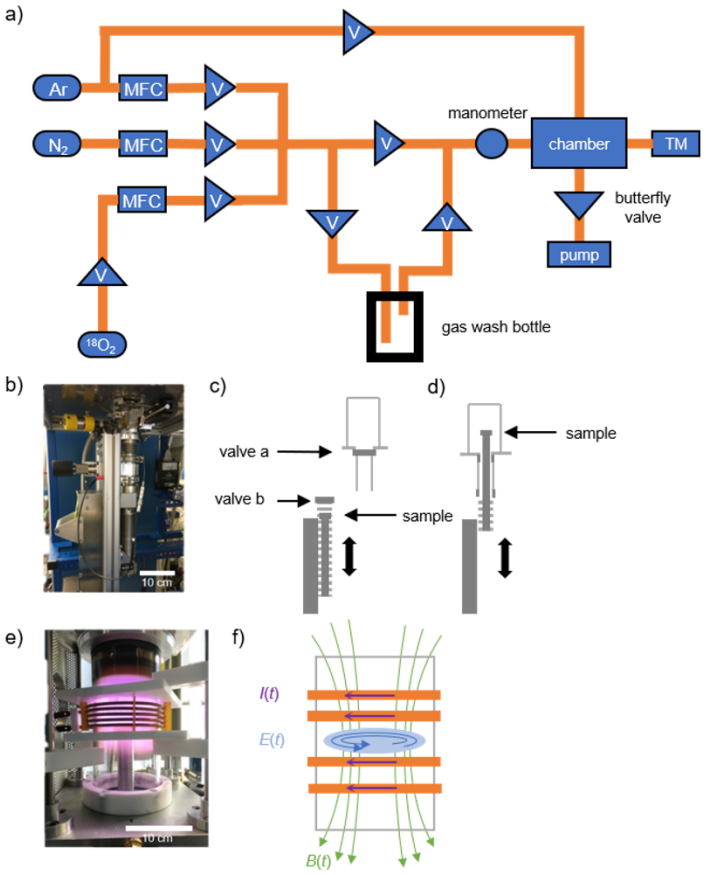

Figure S1: *a) Schematic sketch of the plasma chamber with the different valves and gas lines. b) Photo of the self-made transfer-module (TM). c) and d) Sketch of the TM with valve a to close the chamber and valve b to close the TM. The z-manipulator can be moved into the plasma chamber when both valves are open. e) Picture of an Ar-plasma with the TM driven in. f) Sketch of the emergence of the E and B fields due to the current in the copper coil around the plasma chambe*

S2 – Supporting Information 2:

In Supporting Information 2, the different sample attachments are depicted. The first approach to attach the lithium foil on the *z*-axis manipulator was using a metal frame or a ceramic, see a). After plasma treatment the lithium foil was tarnished, which results from formation of lithium metal on the surface (i.e. through the passivation layer) via lithium metal plating. The free electrons in the plasma can reach the surface and the native passivation layer on the foil acts as a solid electrolyte, evoking Li^+ ion diffusion towards the surface to create lithium metal. This process occurs due to the electrical grounding of the sample. Another possibility to attach the lithium foil is by tesa® or copper tape, see b). While tesa® tape can electrically isolate the sample, copper tape has electrical conductivity. The bigger problem for both tapes is the thermal degradation during plasma treatment and therefore contamination of the lithium foils. The best way to plasma-clean and deposit a polymer layer on top of lithium foils is to clamp them between two ceramics, which prevent lithium metal plating and degradation during the plasma treatment, see c). Still the ceramics has an influence on the plasma and the edges around the ceramic clips look a little different after plasma treatment than the middle part of the lithium foil.

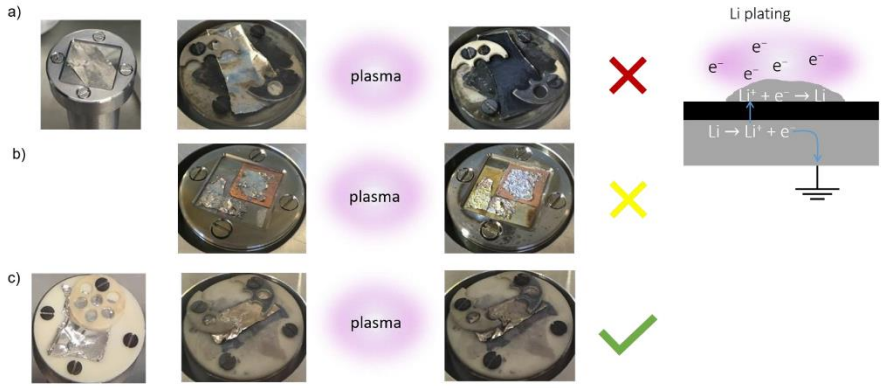

Figure S2: *a) Photographs of a lithium foil before and after argon plasma treatment with the metal frame affixing approach. Schematical sketch of the Li plating process during argon plasma treatment for grounded samples. b) Photographs of lithium foils before and after argon-plasma treatment attached with tesa and Cu-tape. c) Photos of lithium foils before and after argon plasma treatment clamped between ceramics.*

S3 – Supporting Information 3:

In Supporting Information 3, a SEM image of a cracked polymer layer after a deposition time of 15 min is shown. Due to the crack the layer thickness can be estimated to be about 2 µm.

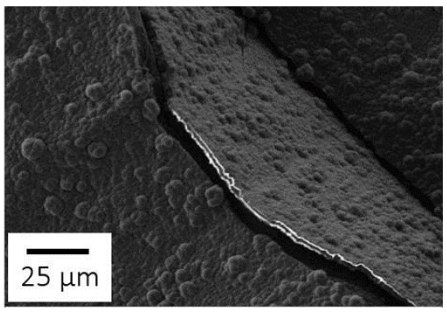

Figure S3: *SEM image of a cracked polymer layer after a deposition time of 15 minutes.*

S4 – Supporting Information 4:

ToF-SIMS surface spectra of lithium foils coated by plasma polymerization, compared with spectra of commercially available Parylene HT®. The following Figure S4 shows sections of the ToF-SIMS spectra of a representative plasma polymer sample and a Parylene HT® sample as a reference. The polymer fragments detected for Parylene HT®, which are formed when the polymer breaks between the C_6H_4- or CF_2-groups, were also detected for the layer formed in the plasma. This supports the hypothesis that the layers formed in the plasma are polymers similar to Parylene HT®. In Figure S5 the whole line spectra from $m/z = 1$ to $m/z = 480$ for both samples are shown. The line spectra for both samples look very similar over the whole mass range, which also indicates the formation of a Parylene HT® like polymer (identical mass spectrometric finger print). At $m/z = 34.968$ and $m/z = 336.39$ the Parylene HT® sample show significant higher intensities than the plasma polymer the signals can be attributed to Cl^- and $C_{24}H_{48}^-$, respectively, and are probably surface contaminations due to sample handling.

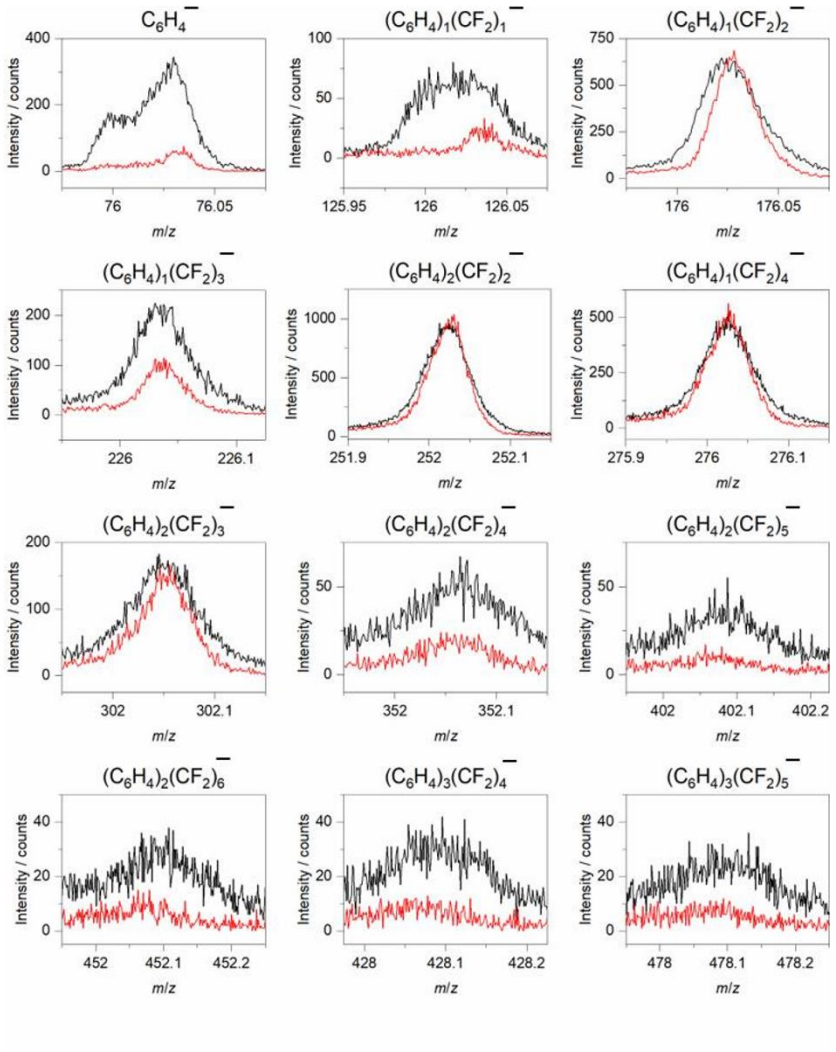

Figure S4: *Sections from ToF-SIMS surface spectra of Parylene HT® (red) and a layer formed by plasma polymerization (black). The fragments detected for the reference sample are also detected for the plasma coated sample.*

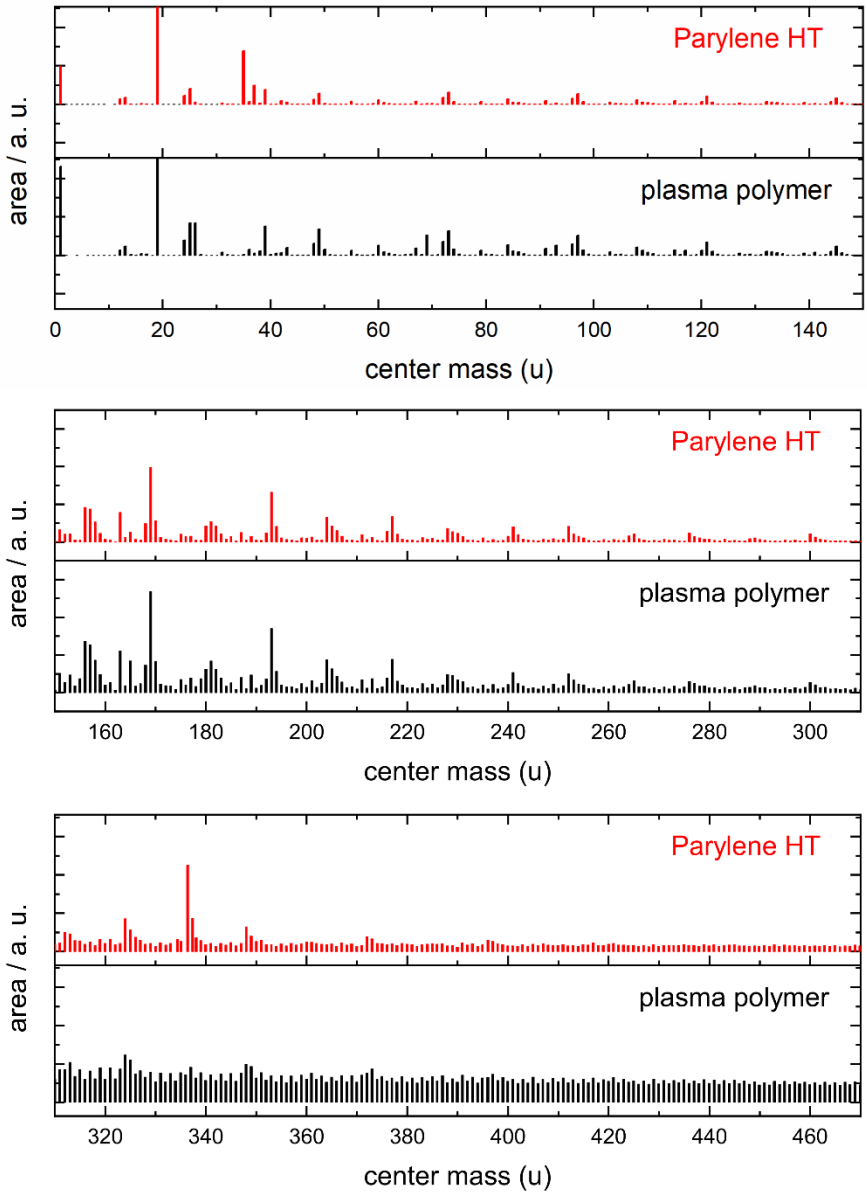

Figure S5: *ToF-SIMS line spectra of Parylene HT® (red) and a plasma polymer sample (black) for m/z = 1 to m/z = 480.*

S5 – Supporting Information 5:

In Figures S6-S9 the continuous stiffness measurements (CSM) of the Si-wafer, the commercial Parylene HT® and the plasma polymer on Si (5 min) and steel (60 s and 5 minutes) for the load, Young's modulus and hardness are shown. The measurements of the Si-wafer S6 show nearly no scattering (3 of 16 measurements were removed) and provide values of 170 GPa for Young's modulus and 12.5 GPa for the hardness, which fit well with literature[1–3]. This serves as a benchmark for the calibration of the nanoindentation system.

In Figure S7 the CSM measurements for commercial Parylene HT® are shown. The measurements exhibit a large scatter and also Young's modulus values are very high, particularly at larger displacements. The big scatter can be explained by the high surface roughness of the sample (R_a about 1 µm) and therefore substrate effects influence the measured values at higher depths.

The measurements of the plasma polymer in Figure S8 on Si and Figure S9 on steel show less scatter than the commercial sample. At larger displacements (>150 nm), however, the substrate starts to influence the modulus and hardness. To minimize the substrate influence due to the layer thickness (~ 1-2 µm), the values at a displacement of 150 nm were taken and plotted in the main text. This depth also corresponds to the rule of thumb for measuring "film-only" properties using nanoindentation, namely to limit the indentation depth to about 1/10 of the film thickness [4]

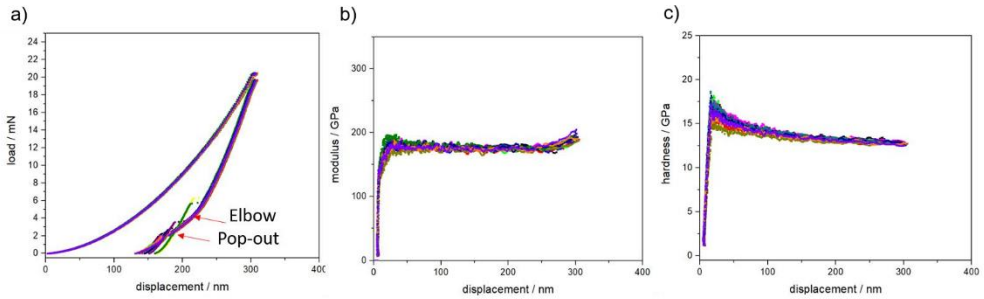

Figure S6: *CSM measurements of a Si-Wafer: a) load, b) Young's modulus, c) hardness. The differently colored curves represent different measurement spots on the sample.*

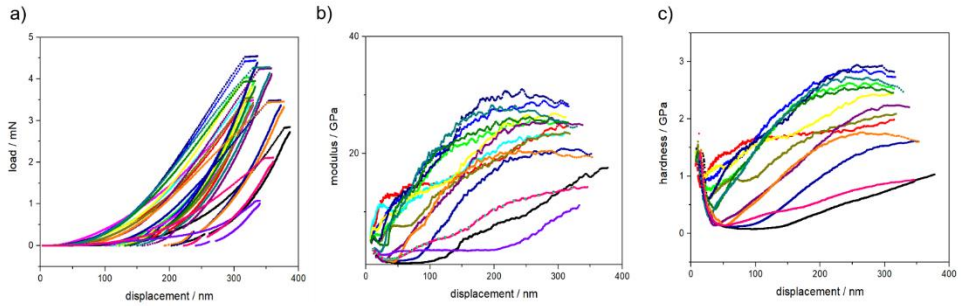

Figure S7: *CSM measurements of commercial Parylene HT®: a) load, b) Young's modulus and c) hardness. The differently colored curves represent different measurement spots on the sample.*

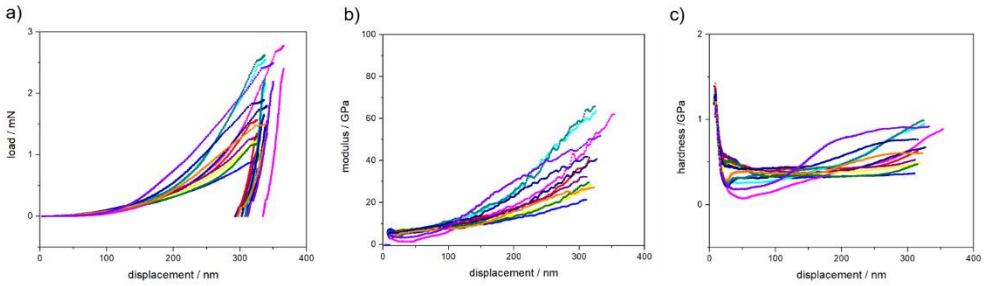

Figure S8: *CSM measurements of a Si-Wafer coated with the plasma polymer for 5 mins: a) load, b) Young's modulus, and c) hardness. The differently colored curves represent different measurement spots on the sample.*

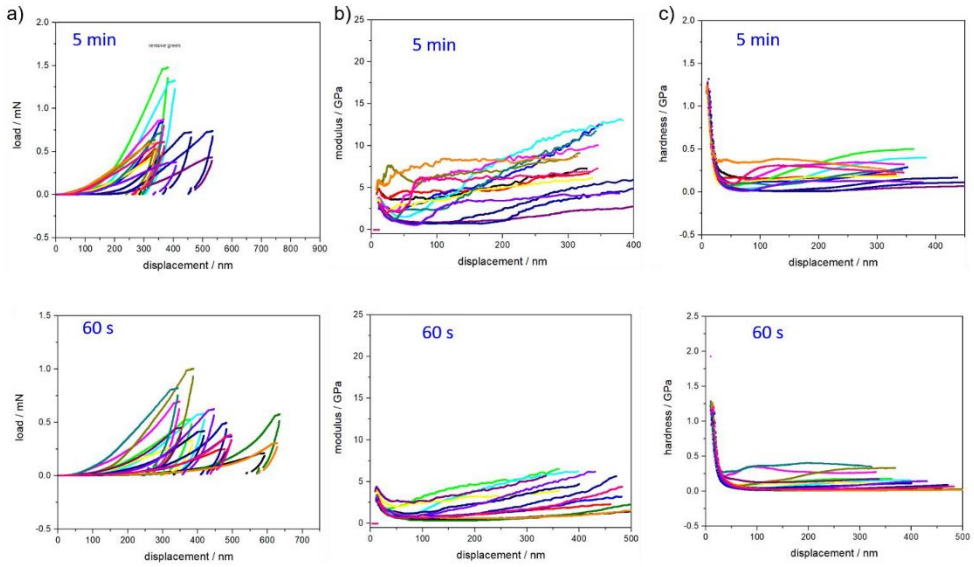

Figure S9: *CSM measurements of steel coated with the plasma polymer for 5 min (top) and 60 s (bottom): a) the load, b) Young's modulus and c) hardness. The differently colored curves represent different measurement spots on the sample.*

S6 – Supporting Information 6:

In Figure S6 a picture of an uncoated LMA (13mm diameter) a) wetted with 50 µL electrolyte directly after wetting and b) after 5 minutes is shown. In comparison to the plasma coated steel discs (see Figure 5 main manuscript) the wetting is worse, which leads to inhomogeneous SEI formation and current densities during cycling. Therefore, the plasma coating does improve the wetting behavior of the used electrolyte.

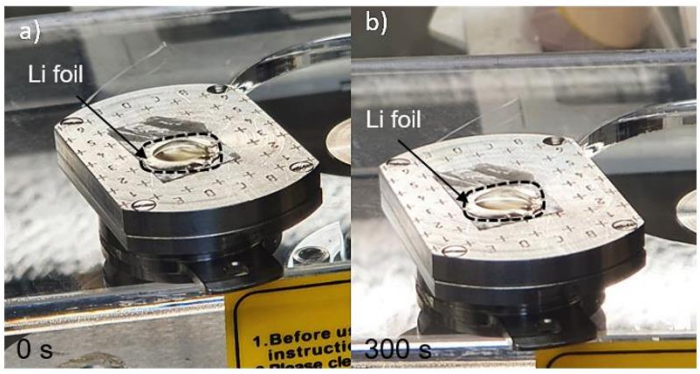

Figure S10: *Pictures of uncoated LMAs wetted with 50 µL electrolyte a) directly after wetting and b) after 5 minutes. It can be seen that the surface is not completely wetted with the liquid electrolyte.*

S7 – Supporting Information 7:

In Figure S11 the solution of Fick's second law for a source with constant surface concentration into semi-infinite space, see equation S1, was fitted to the ToF-SIMS data of the $^{18}O_2$ exposed lithium foil. Due to the large amount of excess oxygen and the slow diffusion, the surface concentration can be assumed to be constant. Oxygen exposures between 6 and 7 Langmuir (L) at 300 K are sufficient to form a Li_2O monolayer coverage on lithium[5] For this diffusion experiment the samples were exposed to 10 mbar $^{18}O_2$ for 30 minutes which is equivalent to roughly $1 \cdot 10^{10}$ L. For depth calibration a comparison measurement carried out with Cs^- sputtering (2 kV) and a sputter yield of 1.72 as determined by Otto et al.[6] was used. The depth was then adjusted to the measurement shown in Figure SI11 and fitted with equation 1. A stainless-steel sample coated with the polymer was sputtered to the interface (polymer/steel) and the crater depth was determined by alpha stepper measurements. A sputter yield of 3.30 with an estimated atomic density of $5 \cdot 10^{22}$ atoms/cm^3 was calculated and used for depth calibration of the lithium coated samples, since the same sputter settings were used. This sputter yield was used till a depth of 1181 nm and after that the sputter yield of lithium was used. The numeric value of 3.30 might be incorrect due to a wrong atomic density but should still provide the correct values for the depth, since the measurement settings were identical.

Due to a maximal diffusion time error of about 2 minutes (180 s), due to pumping of oxygen, transferring the sample into the glovebox and cooling down of the sample the diffusion coefficients were also determined for $t = 1920$ s, in addition to the original diffusion time of $t = 1800$ s, and the resulting values were considered in the stated errors for the diffusion coefficients.

$$c(x) = c_0 + (c_1 - c_0) \cdot \left[1 - \mathrm{erf}\left(\frac{x}{2\sqrt{Dt}}\right)\right] \qquad \text{(S1)}$$

with D = diffusion coefficient, c_0= the natural isotopic background concentration of ^{18}O in the bulk of the sample, c_1 = the ^{18}O concentration of the infinite source at the surface of the sample at x = 0, x = depth and t = diffusion time = 1800 s. The deviation between fit and data points in Figure S11 a) can be assigned to the high roughness of the polymer layer, an ion mixing effects during sputtering.

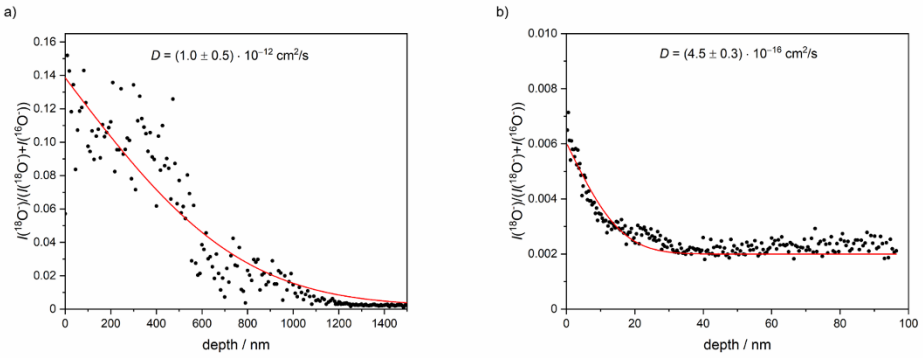

Figure S11: *Fit of equation S1 to the obtained I(^{18}O)/ (I(^{18}O) + I(^{16}O)) ratio from a ToF-SIMS depth profile of a) a coated lithium foil and b) untreated lithium foil. The fit can be realized due to the proportionality between species concentration and secondary ion intensity from ToF-SIMS measurements.*

References:

1. Domnich, V., Gogotsi, Y. & Dub, S. Effect of phase transformations on the shape of the unloading curve in the nanoindentation of silicon. *Appl. Phys. Lett.* **76**, 2214–2216 (2000).
2. Chang, L. & Zhang, L. Mechanical behaviour characterisation of silicon and effect of loading rate on pop-in: A nanoindentation study under ultra-low loads. *Mater. Sci. Eng. A* **506**, 125–129 (2009).
3. Jang, J., Lance, M. J., Wen, S., Tsui, T. Y. & Pharr, G. M. Indentation-induced phase transformations in silicon : influences of load , rate and indenter angle on the transformation behavior. **53**, 1759–1770 (2005).
4. Saha, R. & Nix, W. D. Effects of the substrate on the determination of thin film mechanical properties by nanoindentation. *Acta Mater.* **50**, 23–38 (2002).
5. Skinner, C. H., Sullenberger, R., Koel, B. E., Jaworski, M. A. & Kugel, H. W. Plasma facing surface composition during NSTX Li experiments. *J. Nucl. Mater.* **438**, S647–S650 (2013).
6. Otto, S.-K., Moryson, Y., Krauskopf, T., Peppler, K., Sann, J., Janek, J. & Henss, A. In-Depth Characterization of Lithium-Metal Surfaces with XPS and ToF-SIMS: Toward Better Understanding of the Passivation Layer. *Chem. Mater.* (2021) doi:10.1021/acs.chemmater.0c03518.

7.2 Scientific Contributions

7.2.1 List of Publications

2023

T. Lombardo, F. Walther, C. Kern, **Y. Moryson**, T. Weintraut, A. Henss, M. Rohnke (**2023**) *ToF-SIMS in battery research: Advantages, limitations, and best practices.* J. Vac. Sci. Technol. A 41, 053207 (2023)

H. Huo, M. Jiang, B. Mogwitz, J. Sann, Y. Yusim, T. Zuo, **Y. Moryson**, P. Minnmann, F. H. Richter, C. V. Singh, J. Janek (**2023**) *Interface Design Enabling Stable Polymer/Thiophosphate Electrolyte Separators for Dendrite-Free Lithium Metal Batteries.* Angew. Chem. Int. Ed*. 2023, e202218044*

B. Krauskopf, S.-K. Otto, **Y. Moryson**, F. Hoffmann, J. Sann, J. Janek (**2023**) *Thin and Homogenous Surface Functionalization of Lithium Metal Anodes by Defined Molecular Treatment.* J. Electrochem. Soc. 2023*, 170*

Y. Moryson, H. Hartmann, S-K. Otto, X. Fang, M. Rohnke, J. Janek (**2023**) *Protective Coating for the Lithium Metal Anode Prepared by Plasma Polymerization.* ACS Appl. Energy Mater*. 2023, 6,12,6656-6665*

2021

S.K. Otto, **Y. Moryson**, T. Krauskopf, K. Peppler, J. Sann, J. Janek, A. Henss (**2021**) *In-Depth Characterization of Lithium-Metal Surfaces with XPS and ToF-SIMS: Toward Better Understanding of the Passivation Layer.* Chem. Mater. 2021, 33

S.K. Otto, T. Fuchs, **Y. Moryson**, C. Lerch, B. Mogwitz, J. Sann, J. Janek, A. Henss **(2021***) Storage of Lithium Metal: The Role of the Native Passivation Layer for the Anode Interface Resistance in Solid State Batteries.* ACS Appl. Energy Mater. 2021, 4

Y. Moryson, F. Walther, J. Sann, B. Mogwitz, S. Ahmed, S. Burkhardt, L. Chen, P.J. Klar, K. Volz, S. Fearn, M. Rohnke, J. Janek (**2021**) *Analyzing Nanometer-Thin Cathode Particle Coatings for Lithium-Ion Batteries—The Example of TiO_2 on NCM622.* ACS Appl. Energy Mater. 2021, 4

2020

R. Pan, D. Rau, **Y. Moryson**, J. Sann, J. Janek (**2020**) *Reversible Capacity Loss of $LiCoO_2$ Thin Film Electrodes*. ACS Appl. Energy Mater. 2020, 3, 7.

P. Cop, E. Celik, K. Hess**, Y. Moryson**, P. Klement, M. T. Elm, B. M. Smarsly (**2020**) *Atomic Layer Deposition of Nanometer-Sized CeO_2 Layers in Ordered Mesoporous ZrO_2 Films and Their Impact on the Ionic/Electronic Conductivity.* ACS Apl. Nano Mater. 2020, 3, 11

2019 L. Ostheim, P.J. Klar, **Y. Moryson**, M. Rohnke, A. Beyer, M. Volk, M. Munde, W. Stolz, K. Volz (**2019**) *Effect of the interface morphology on the lateral electron transport in (001) GaP/Si heterostructure.* J. Appl. Phys. 126

2017 M. Göttlicher, M. Rohnke, **Y. Moryson**, J. Thomas, J. Sann, A. Lode, M. Schumacher, R. Schmidt, S. Pilz, A. Gebert, T. Gemming, J. Janek (**2017**) *Functionalization of Ti-40Nb implant material with strontium by reactive sputtering*. Biomaterials Research 21:18

7.2.2 List of Conference Contributions

2022 Oral Presentation: **AVS 68**, Pittsburgh, USA (11/2022): *Enhancing the performance in Li-ion batteries by plasma polymer coating of Li-metal anodes.*

Online Oral Presentation: **Online Symposium "Lithium Metal Anodes and their Application in Batteries**" (02/2022): *Enhancing the performance in Li-ion batteries by plasma polymer coating of Li-metal anodes.*

2021 Online Oral Presentation: **Rice University SIMS Workshop** (04/2022): *Detection of nanoscopic coatings on next generation battery materials by ToF-SIMS and related methods.*

2019 Poster Presentation: **XXII. International Conference on Secondary Ion Mass Spectrometry**, Kyoto, Japan (10/2019): *Challenges and Principles of 3D ToF-SIMS Imaging of Microparticles.*

2018 Poster Presentation: **SIMS Europe 2018**, Münster, Deutschland (09/2018): *Influence of the substrate temperature on the ionization probability.*

8. Acknowledgement

At first, I would like to thank my doctoral supervisor Prof. Dr. Jürgen Janek for giving me the opportunity to realize this doctoral thesis in his research group. Furthermore, I gratefully thank him for his support, his feedback and discussions during my time in his group.

I would like to express my very special thanks to PD Dr. Marcus Rohnke for supervising me since my Bachelor thesis and always supporting me with his knowledge on scientific and technical issues, as well as introducing me into operating the ToF-SIMS.

Special thanks also go to Dr. Anja Henß, for helping on issues with the ToF-SIMS, Dr. Joachim Sann for introducing me into operating the XPS and his advice concerning XPS data evaluation and to the precision mechanics workshop under the supervision of Harry Heidt, for the excellent work with the plasma chamber and transfer module.

Furthermore, I like to thank Prof. Dr. Michael Dürr for being the 2nd reviewer of this thesis.

I acknowledge the financial support of my work by the BMBF (Bundesministerium für Bildung und Forschung) within the MaLiBa (03XP0185D) project.

I would like to thank all project-, cooperation and research partners I had the pleasure to work with, for many fruitful discussions and good inputs. Particularly, I would like to thank all members of the BMBF project MaLiBa from JLU, IWS Dresden, SGS and hpulcas for the good work and atmosphere within the project and my current and former colleagues and friends in the Janek group, especially, Dr. Markus Göttlicher, Dr. Felix Walther, Dr. Svenja-Katharina Otto, Luise Riegger, Bastian Krauskopf, Hannah Hartmann, Mark-Melvin Pradja and Tobias Wagner.

Last but not least, I thank my family and friends, who supported me during my study and PhD time and my parents, which financially enabled me to study.